DESIGN, ANALYSIS AND SIMULATION OF HIGH SENSITIVITY, N-COUPLED OSCILLATOR, MICRO GYROSCOPE

by

Hoorad Pourzand

A thesis submitted to the faculty of
The University of Utah
in partial fulfillment of the requirements for the degree of

Master of Science

Department of Electrical and Computer Engineering

The University of Utah

May 2015

Copyright © Hoorad Pourzand 2015

All Rights Reserved

THE UNIVERSITY OF UTAH GRADUATE SCHOOL

STATEMENT OF THESIS APPROVAL

The thesis of **Hoorad Pourzand**

has been approved by the following supervisory committee members:

Massood Tabib-Azar, Chair **6/2/2014**
Date Approved

Rajesh Menon, Member **6/2/2014**
Date Approved

Bruce Gale, Member **6/2/2014**
Date Approved

and by **Gianlucca Lazzi**, Chair/Dean of

the Department/College/School of **Electrical and Computer Engineering**

and by David B. Kieda, Dean of The Graduate School.

ABSTRACT

Microelectromechanical gyroscopes are readily used in cars and cell phones. Tactical gyroscopes are available inexpensively and they offer 0.01 to 0.1 % scale factor inaccuracy. On the other hand, strategic gyroscopes with much better performance levels are 100,000 times more expensive. The main objective of this work is to explore the possibility of developing inexpensive strategic grade gyroscopes using microelectromechanical systems technology.

Most of the available gyroscopes are surface micromachined due to fabrication issues and misalignment problems involved in multistep fabrication processes necessary to use the bulk of the wafer as the proofmass in MEMS gyroscopes. It can be shown that the sensitivity of the gyroscope is inversely proportional to the natural frequency; so if bulk micromachining technique is used it is possible to decrease the natural frequency further than current limits of surface micromachining in order to increase sensitivity. This thesis is focused on proposing a way to use bulk of the silicon wafer in the gyroscope to decrease the natural frequency to very low levels, such as sub-KHz regime, that cannot be achieved by single mask surface micromachining processes. It then proposes a solution for solving the misalignment problems caused by using multiple fabrication steps and masks instead of using only one mask in surface micromachined gyroscopes.

In our design discrete proofmasses are linked together around a circle by compliant structures to ensure the highest effective mass and lowest effective spring

constant. By using a proposed double sided fabrication technology the effect of misalignments on frequency mismatch can be reduced. ANSYS software simulations show that 20 μm misalignment between the masks causes a frequency shift equal to 0.3% of the natural frequency that can be compensated using electrostatic frequency tuning. Acceleration parasitic effects can also be a major problem in a low natural frequency gyroscope. In our design a multiple sensing electrode configuration is used that cancels the acceleration effects completely. The sensitivity of the gyroscope with 3126 Hz natural frequency is simulated to be 574 $\frac{mV}{deg/sec}$, or about four times higher than 132 $\frac{mV}{deg/sec}$, which was used as a benchmark for a sensitive gyroscope.

Dedicated to my parents,

Tayyebeh Ghanbari

and Mahdi Pourzand

TABLE OF CONTENTS

ABSTRACT ... iii

LIST OF TABLES ... viii

LIST OF FIGURES ... ix

LIST OF SYMBOLS ... xiii

LIST OF ABBREVIATIONS ... xvi

ACKNOWLEDGMENTS ... xvii

CHAPTERS

1: INTRODUCTION ... 1

1.1: Surface Acoustic Wave (SAW) Gyroscopes ... 3
1.2: Levitated Rotating Ring Gyroscopes ... 5
1.3: Multi Axis Gyroscopes ... 6
1.4: Decoupling Gyroscopes ... 6
1.5: Tuning Fork Gyroscopes ... 8
1.6: Motivation hor N-Coupled Oscillator Gyroscopes ... 9

2: CONCEPTUAL DESIGN ... 14

2.1: Conceptual Design cnd Fabrication Method ... 14
2.2: Sensitivity Increase Concept ... 17
2.2: Quality Factor Enhancement Techniques ... 24
2.3: The Effect qf Using Multiple Resonators with Resonant Frequency Uhifts kn vhe Drive Mode ... 28
2.4: Optimum Number qf Resonators ... 29
2.5: The Effect qf Coupling ... 30

3: MODELING ... 32

3.1: Frequency qf c Single Oscillator Versus Cantilever Thickness ... 32
3.2: Frequency Analysis ... 33

3.3: Electro Mechanical Analysis 34
3.4: Pull-In Analytical Calculations 42
3.5: Pull-In COMSOL Simulation 44
3.6: Sense cnd Drive Frequency Versus Misalignment ....0................................ 45

4: DESIGN 52

4.1: Natural Frequency 52
4.2: Silicon Coupler - 5 µm Nickel Cantilever – Q = 200 55
4.3: Polymer Coupler - 1 µm Nickel Cantilever – Q = 200 66
4.4: Polymer Coupler - 1 µm Nickel Cantilever – Q = 20000 73
4.5: Polymer Coupler - 1 µm Nickel Cantilever – Q = 20000 y ith po Frequency Shift Between Sense cnd Drive....0.......... 77
4.6: Readout Circuit 79
4.7: Acceleration Canceling Technique 83
4.8: Stress Analysis 92

CONCLUSION 95

APPENDICES

A: MISALIGNMENT COMPENSATION TECHNIQUE 96

B: TRIMMER CAPACITOR DATASHEET 104

REFERENCES 106

LIST OF TABLES

3.1: Model dimensions…………………………………………………………..… 46

4.1: Simulation results for different rotation speeds for try number 1...................... 60

4.2: Simulation results for different rotation speeds for try number 2…………...... 71

4.3: Simulation results for different rotation speeds for try number 3…………...... 75

4.4: Simulation results for different rotation speeds for try number 4...................... 78

4.5: Final dimensions and characteristics of the device………………………….... 94

B.1: Trimmer capacitor TZY2Z010A001R00……………………………….…. 104

LIST OF FIGURES

1.1: Comparison of MEMS and optical gyroscopes………..…………………….……… 2

1.2: Sensitivity comparison of MEMS gyroscopes…………………....……………. 4

1.3: Double decoupling………………………………..……..…………………... 8

1.4: Ratio of natural frequency to the single cantilever natural frequency versus coupling ratio for five different mode shapes………………........……………..… 11

1.5: Coupled resonators subjected to a 10 μN pulse for 10 μs……………..…...…… 12

1.6: Transient response of the first four resonators with nickel cantilevers and SU8 polymer couplers……………………….……………………………………...…... 12

2.1: Different methods of coupling the resonators………………..……………..….. 14

2.2: Two mode shapes with 45 degrees difference in orientation………….…...….. 15

2.3: Velocity directions and shown with orange arrows and Coriolis force with yellow arrows around the ring gyroscope……………………….…........….. 15

2.4: Fabrication sequence of the device…………………..………...…...……….. 17

2.5: Connection of proofmasses to the couplers from the central points to decrease natural frequency and increase sensitivity of the device……….……………………………………………………..………....…. 18

2.6: Two mode shapes with 90 degrees difference in orientation……….……....… 21

2.7: Acoustic waves propagating away through the anchors of the resonator causing a leak of energy…………….………………………………..……..….. 26

2.8: Proposed bulk mass resonator with driving electrode bonded over a glass wafer with a trench…………... 28

3.1: Three-dimensional model of the actuator…………………..………....……….. 32

3.2: Modeling of the resonator with a rotational spring pendulum system……...... 33

3.3: Natural frequency of the bulk mass resonator using analytical formulation compared to ANSYS simulation………………………..……….. 34

3.4: Two-dimensional model of the actuator…….…………………………..……. 36

3.5: Two-dimensional equivalent model of the actuator by replacing the fixed electrode with a force and a negative spring constant linear spring or a moment and a negative spring constant rotational spring.…………….……… 36

3.6: Location of resultant force versus displacement of the electrode tip............... 39

3.7: Dimensionless moment versus dimensionless electrode tip displacement………………………………………...…………...……. 41

3.8: Zoomed view of dimensionless moment versus dimensionless electrode tip displacement ……………………………...…………..……… 41

3.9: Pull-in COMSOL simulation of the microactuator…………………...………. 44

3.10: Capacitance versus voltage difference……………………..………………… 45

3.11: Electrode tip displacement versus voltage difference……………….……….. 46

3.12: Overall structure……………………………………………...………......... 47

3.13: Overall structure from the top view…………………………..……………. 47

3.14: Nickel coupler and point contact………………………..…………………. 48

3.15: Nickel coupler and point contact from another view…………...…………….. 48

3.16: Drive frequency of 23459.6 Hz………...………………...………………... 49

3.17: Sense frequency of 23476.22 Hz….………………..……………………… 49

3.18: Drive frequency of 23345 Hz…………………...………………………......... 50

3.19: Sense frequency of 23434.6 Hz….……………………..………………….. 51

4.1: Initial meshed model used in our design process……..………...……………. 53

4.2: Zoomed view on the initial meshed model used in our design process……… 53

4.3: First parasitic mode shape, 11615.9 Hz……….………..…………………..... 55

4.4: Second parasitic mode shape, 11623.4 Hz ………………..……..……...... 56

4.5: Drive mode shape, 19600.6 Hz…………………………..…................... 56

4.6: Sense mode shape, 19701.1 Hz ………………...…………...……..……… 57

4.7: Fifth mode shape, 20374.6 Hz………..……………………….....……..…… 57

4.8: Sixth mode shape, 33281.6 Hz……………………………......……………. 58

4.9: Rotation harmonic response for 650 deg/sec …………………..………….. 59

4.10: No rotation harmonic response……...…………………………….………. 59

4.11: Radial sensing displacement and pattern rotation for up to 650 deg/sec external rotation……………...…………………………..…………... 60

4.12: First parasitic mode shape, 1439.72 Hz...……………………..……...……. 67

4.13: Second parasitic mode shape, 1441.09 Hz ……………..……….....…………. 67

4.14: Third parasitic mode shape, 2977.6 Hz ………………………...…………. 68

4.15: Drive mode shape, 3125.97 Hz…………………………………...………..…. 68

4.16: Sense mode shape, 3139.74 Hz………………………………..…...……… 69

4.17: Sixth mode shape, 6063.24 Hz..…………...…………………..………….... 69

4.18: External rotation harmonic response for 500 deg/sec ………..……….......... 70

4.19: No external rotation harmonic response..………………………...…...…… 70

4.20: New mesh pattern with mapped meshing almost everywhere except places the coupler is attached to the resonator……………………......……… 78

4.21: Capacitive readout circuit……………………........………………………. 80

4.22: Working frequency of 3126 Hz…………….………..………...……..….. 84

4.23: Z parasitic mode of 5641 Hz……….…………......……………....…….. 84

4.24: X parasitic mode of 1440 Hz………………..…......………..…...……..…. 85

4.25: Y parasitic mode of 1440 Hz…………..…………....……........................ 85

4.26: Multiple sensing electrodes…......………………………....…………...……. 88

4.27: Multiple sensing electrode Wheatstone bridge configuration…....……….. 89

4.28: Multiple sensing electrode Wheatstone bridge configuration with fixed voltage central hub……………………………......……………….. 90

A.1: Fabricated prototype of the structure using the conventional fabrication method…………………………………......…………………….. 97

A.2: Insensitivity of the dimensions of parallelogram to shifting of two facing edges…………………………………......….………...……….. 98

A.3: Uniformity and insensitivity of the dimensions of the column to misalignment of the top and bottom masks……......……………….……….... 99

A.4: Floating lines on the top and bottom masks and different features that are finally generated…………………………..…….....……….…………… 100

A.5: Two needed masks to fabricate eight resonators……………..…….....……. 101

A.6: The effect of misalignment of the bottom mask on the movement of proofmasses with respect to the initial positions………………...…...…….. 102

A.7: Trimmer capacitor TZY2Z010A001R00……………...…………………..…. 105

LIST OF SYMBOLS

Symbol	Description
T	Precession torque Temperature in Kelvin
I	Moment of inertia Moment of area
$\boldsymbol{\omega}$	Rotational speed of the rotor
$d\theta/dt$	Angular rate
U	Drive amplitude
Q	Quality factor
Q_d	Quality factor in drive direction
Q_s	Quality factor in sense direction
$Q_{surface}$	Quality factor by air dissipation
$Q_{support}$	Quality factor by support loss
Q_{TED}	Q by thermo elastic damping
F_d	Driving force
K_d	Spring constant in drive direction
K_s	Spring constant in sense direction
M_c	Resonator mass that moves in the sense direction
$\boldsymbol{\sigma}$	Brownian noise of Coriolis vibratory gyroscope
W_d	Drive frequency
F_c	Coriolis force
Ω_z	External rotation
K_B	Boltzmann constant
m_{eq}	Equivalent mass
M	Mass, moment
c_{eq}	Equivalent damping
f_0	Natural frequency
ζ	Total damping ratio
$\zeta_{support}$	Damping ratio for support loss
h	Cantilever thickness
l	Cantilever length, Proofmass height

K_θ Rotational retaining spring constant of the actuator

E Young modulus

C_x The capacitance of the actuator as a function of x

H Thickness of the proofmass

f Displacement of the electrode at distance y from the pivot point

G The distance of the resultant electrical force from the pivot point

$K_{\theta,elec}$ Negative rotational spring constant of the electrical force on pivot point

F_{top} Resultant electrical force after being moved to the top of the actuator

α Ratio of actuator tip displacement to the electrode gap

I_θ Mass moment of inertia around the pivot point

W Width of proofmass

x Displacement of the tip of the actuator

d Electrode gap

V Voltage difference between electrodes

$K_{rim,elec}$ Negative linear spring constant of the electrical force on tip of the actuator

F_{total} Resultant electrical force in its original place

df_y Infinitesimal electrical force on area w.dy with distance y from the pivot point

$\Delta C'$ Capacitance difference between two tuning capacitors of the Wheatstone bridge

Symbol	Description	Symbol	Description
ε	Permittivity	$\alpha_{pull\text{-}in}$	Pull-In displacement divided by electrode gap
$V_{pull\text{-}in}$	Pull-In voltage	ΔC	Capacitance change
$K_{eff,coupler}$	Effective spring constant of the coupler	$M_{eff,coupler}$	Effective mass of the coupler
$K_{\theta,\ bending}$	Bending rotational spring constant of the cantilever	$K_{\theta,\ tortion}$	Torsional rotational spring constant of the cantilever
$I_{\theta i}$, I_{θ}	Mass moment of inertia of each resonator	V_{ac}	AC component of driving voltage
V_{dc}	DC component of driving voltage	ΔC_1	Capacitance change of first sensing capacitor
ΔC_2	Capacitance change of second sensing capacitor	ΔC_3	Capacitance change of third sensing capacitor
ΔC_4	Capacitance change of forth sensing capacitor	C_0	Initial capacitance
$V_{ac\text{-}readout}$	Driving voltage of sensing circuit	V_{out}	The output signal of the sensing circuit
θ_{max}	Maximum rotation of the proofmass	M_{max}	Maximum moment in the cantilever
K_c	Coupling spring	A_p	Amplitude of vibration of resonator numbered by p
n	Mode shape number	p	Resonator number

LIST OF ABBREVIATIONS

MEMS	Micro electro mechanical systems
SAW	Surface acoustic waves
IDT	Inter digital transducer
VLSI	Very large scale integration
SOI	Silicon on insulator
DOF	Degree of freedom
MUMPS	Multi-user MEMS processes
DRIE	Deep reactive ion etching
TFG	Tuning fork gyroscope
DR	Decoupling ratio
SCS	Single crystal silicon
BAW	Bulk acoustic waves
HARPSS	High aspect ratio combined poly and single crystal silicon
CING	Cylindrical rate-integrating gyroscope
SOG	Silicon on glass
TED	Thermo elastic damping
FEM	Finite elements method
CVD	Chemical vapor deposition

ACKNOWLEDGMENTS

I sincerely appreciate the support of Professor Massood Tabib-Azar, specially during my first semester at the University of Utah, and for providing me the main idea of bulk mass resonators and his guidance throughout the project. I also want to thank Pradeep Pai and Brian Baker for their assistance in microfabrication of initial prototypes.

Special thanks go to my family members for their constant support and all those who helped me intentionally and unintentionally.

CHAPTER 1

INTRODUCTION

The basics of micro-electromechanical (MEMS) gyroscopes and their different types are covered thoroughly in [1], [2] and [3] and are not covered again here. After going through different designs of MEMS gyroscopes it can be seen that most of them are surface micromachined. The main reason is usually fabrication issues and also misalignment problems that are involved in multistep fabrication processes necessary to use the bulk of the wafer as the proofmass in the MEMS gyroscope. In later chapters it is shown that the sensitivity of the gyroscope is inversely proportional to the natural frequency; however, if surface micromachining technique is used it may not be able to decrease the natural frequency a lot. This thesis is focused on proposing a way to use bulk of the silicon wafer in the gyroscope to decrease the natural frequency to very low levels such as a sub-kilohertz regime that cannot be achieved by single mask surface micromachining processes. It then proposes a solution for solving the misalignment problem caused by using multiple fabrication steps and masks instead of using only one mask in surface micromachined gyroscopes. MEMS gyroscopes have much lower final cost compared to conventional optical gyroscopes. In Figure 1.1, the cost and performance of optical and MEMS gyroscopes are compared.

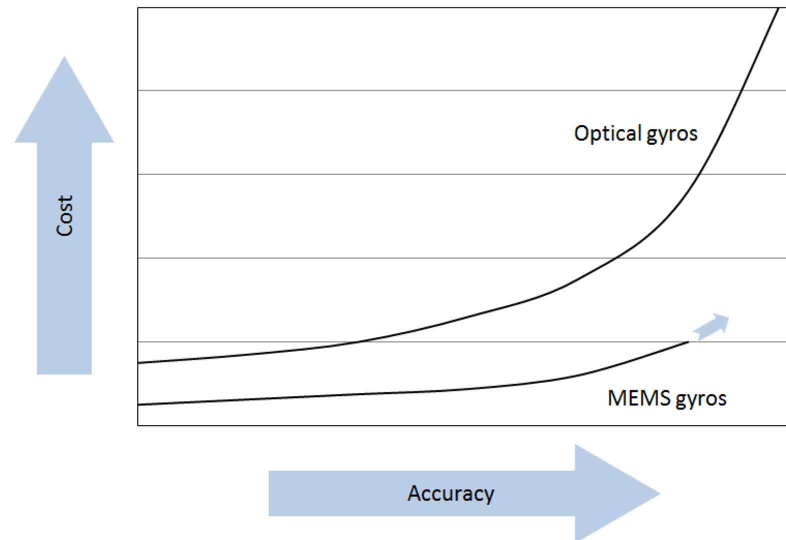

Fig 1.1: Comparison of MEMS and optical gyroscopes. Modified from [4].

It can be concluded from Figure 1.1 that if some solutions are proposed to push the sensitivity and other performance characteristics of MEMS gyroscopes beyond their current limits, there is a high chance to replace more expensive optical gyroscopes that have the same performance level with the newly designed MEMS gyroscopes because of lower cost and weight [4]. In this way the total cost of our designs can be reduced while keeping the same performance level, which guarantees a good market for the newly designed sensitive MEMS gyroscopes. There are also some new applications in space and aviation industry that require very small sizes, low weights or low costs that conventional gyroscopes cannot be used in. In these applications, MEMS gyroscopes have to be chosen although they may have worse characteristics. Considering these facts and applications all research projects on improving the performance characteristic of MEMS gyroscopes are highly justifiable and reasonable, including this work.

The next step is finding which type of MEMS gyroscopes are the best choice for performance improvement. It is well known that different types of MEMS gyroscopes have different typical performance characteristics. The concentration of this work is on sensitivity improvement, noise levels are not considered. From the review of reference paper [3], which was published in 2009, the highest sensitivities for different types of MEMS gyroscopes are selected and plotted in Figure 1.2. It can be seen that the highest sensitivity, which is 132 mV/º/sec, belongs to a ring type gyroscope fabricated in 2002 [5]. It should also be noted that the total sensitivity of the gyroscope depends on two things, the sensitivity of the readout circuit and the gyroscope type and dimensions. The difference in sensitivities between the ring type MEMS gyroscope and other types is so high that it cannot be only related to more sensitive circuit; so it can be concluded that MEMS ring type gyroscopes are the best type of gyroscope to focus on for improvements simply because they have the maximum sensitivity reported. The value of 132 mV/º/sec is also considered as the benchmark in this thesis for a sensitive gyroscope and the goal is designing a gyroscope with a better sensitivity. The gyroscopes shown in Figure 1.2 are discussed briefly below [3], except ring type gyroscopes which are explained in the next chapter.

Surface Acoustic Wave (SAW) Gyroscopes

In 1997, Kurosowa et al. proposed a completely novel design concept of an inter-digitated transducer (IDT) SAW gyroscope which includes IDTs, reflectors, and a metallic dot array within the cavity [6]. The IDTs and reflectors are fabricated through microfabrication techniques on the surface of a piezoelectric substrate, 128° YX $LiNbO_3$.

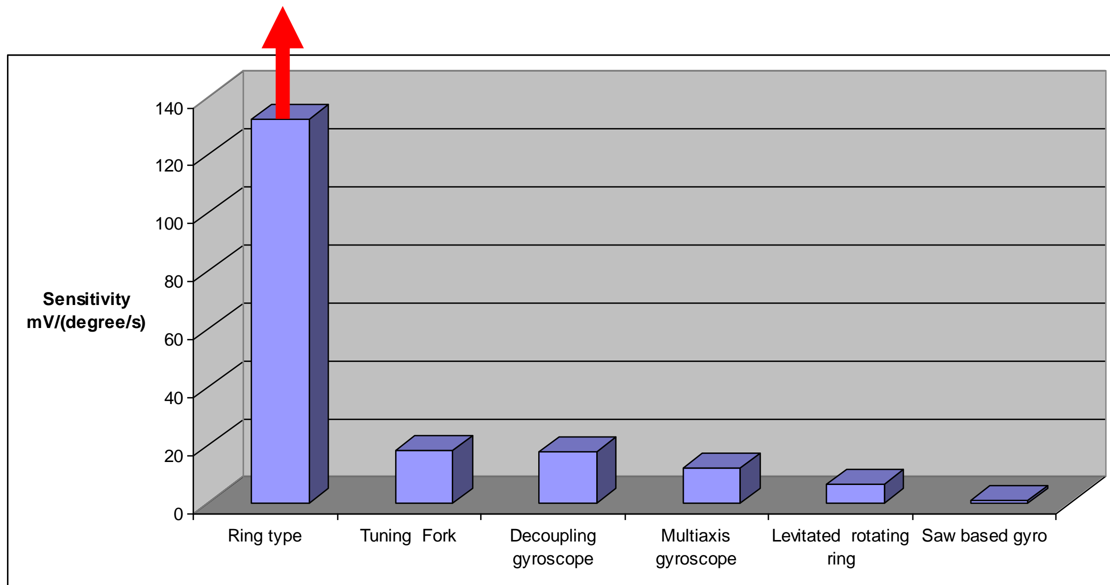

Fig 1.2: Sensitivity comparison of MEMS gyroscopes.

The transmitter IDT creates SAW that propagates back and forth between the reflectors and forms a standing wave inside the cavity due to the collective reflection from reflectors. SAW reflection from individual metal stripes adds in phase if the reflector periodicity is equal to half a wavelength. For the established standing wave, a substrate particle at the nodes of a standing wave has no amplitude of deformation in the z-direction; however, at or near the antinodes of the standing wave pattern, particles will experience larger amplitude of vibration in the z-direction, which serves as the reference vibrating motion for this gyroscope. In the presence of external rotation dot arrays over the antinodes will vibrate along the orthogonal direction to the standing wave because of the Coriolis force and will generate a secondary surface acoustic wave that can be sensed. Despite fabrication, the Kurosowa gyroscope did not obtain any output signal; the improvement was from Pennsylvania State University who fabricated the first 1 cm × 1 cm sample gyroscope which has a sensitivity of 705 µV/º/s [7].

Levitated Rotating Ring Gyroscopes

The levitated rotational-gyro/accelerometer consists of a spinning rotor and stators that maintain the rotor at its null position by applying levitation control. When an angular rate orthogonal to the spinning axis is applied, a precession torque applied by the levitation control returns the rotor to the null position. The formula below gives the magnitude of the precession torque, T, as a function of the moment of inertia, I, the rotational speed of the rotor ω, and the angular rate $\dot{\theta}$:

$$T = I\omega\dot{\theta} \tag{1.1}$$

An electrostatically suspended and sensed micromechanical rate gyroscope is comprised of a disk-shaped rotor with flange; the active conductive layer of which is composed of structural polysilicon and separated from the other conductive layers by an insulating silicon nitride layer and five sets of actuators, required by position control in both axial and radial directions. Three are for the upper and lower axial suspensions so that height and tilt relative to the substrate may be set, and two are for radial centering and driving. The motor drive electrodes transfer the sustaining torque for the spinning element and sensor electrodes are all placed below the rotor. In a word, the device consists of three types of electroquasistatic components: the motor drive, position sensors and the nonrotary actuators for rebalance and suspension. The spinning element of the gyroscope is a three-phase bipolar variable-capacitance synchronous motor and the gyroscope is a rebalanced gyroscope that has a control system designed to hold the gyroscope in a constant position while it is subject to external forces. As with suspended

macroscopic gyroscopes, the rotor is spun by a motor to produce angular momentum, suspended and controlled by force and torque actuators, and sensed by various position sensors. The structure is fabricated according to current very large scale integration (VLSI) micromachining methods. The rotor diameter is 4000 μm, which leads to a minimum detectable angular rate of 0.05 °/s and the total sensitivity of 6.5 mV/°/sec [8].

Multiaxis Gyroscopes

The vast majority of research has focused on single input axis rate gyroscopes. Dual and multi-input axes have the advantage of lowering cost and increasing efficiency. WACOH corporation is developing a new 5-axis motion sensor fabricated by SOI bulk micromachining. The whole package is made of glass, silicon on insulator (SOI) and glass from top to bottom and the chip size is minimized to $5.0 \times 5.0 \times 1.7$ mm^3. By using an electrostatic resonant drive at 3.42 KHz and nonresonant capacitive detection mode, the sensitivities of Ω_x and Ω_y are 6.61 mV/°/s and 12.1 mV/°/s, respectively. Cross-axis sensitivity is reported to be less than 5% and full scale nonlinearity is less than 3% [9].

Decoupling Gyroscopes

Quadrature signal and Coriolis offset are two important factors influencing performance of vibrating gyroscopes. In fact, ideal drive motion is never achieved and the drive displacement will have a vector component in the sense direction. Like the Coriolis motion, this displacement along the sense direction will be at drive frequency. Hence, this error signal will corrupt the desired Coriolis motion signal. This error is called quadrature signal since there is a 90° phase difference between quadrature and the desired Coriolis output. Coriolis offset is another error signal which appears at the output

at drive frequency. Coriolis offset arises when the drive force has a component along the sense direction. One of the methods to reduce the two errors mentioned above is through signal controlling. Another elegant solution to suppress the quadrature error in gyroscopes is through a clever design of mechanical suspension. Mechanical decoupling structure with different degree of freedoms (DOFs) can effectively lower the quadrature error and the Coriolis offset. The concept of quadrature error is explained really well in reference [1].

Middle East Technical University in Turkey reported a novel symmetric micromachined gyroscope design that provides enhanced decoupling of the drive and sense modes [10], and increased actuation and detection capacitances beyond the fabrication process limitations. The novel decoupling mechanism is based on providing 2DOF oscillation capability to the gyroscope proof mass, while the degrees of freedom of the actuation and detection electrodes are restricted to 1-DOF, as shown in Figure 1.3. The decoupling mechanism minimizes the effects of fabrication imperfections and the resulting anisoelasticities by utilizing independent folded flexures and constrained moving electrodes in the drive and sense modes. Bulk micromachined prototype gyroscopes have been fabricated and the experiment shows that over an order of magnitude of capacitance increase is achieved in the same footprint of the device, without additional fabrication steps. They fabricated gyroscopes using a standard three-layer polysilicon surface micromachining process, multi-user MEMS process (MUMPs) and a nickel electroforming process. The improved gyroscope in 2006 had a 18 µm thick nickel structural layer with 2.5 µm capacitive gaps, providing an aspect ratio above 7 a noise-equivalent rate of 0.095 $(°/s)/\sqrt{Hz}$ and short-term bias stability better than

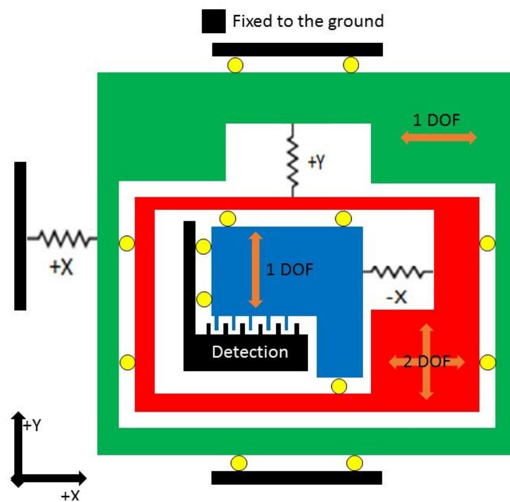

Fig 1.3: Double decoupling. Modified from [3].

0.1º/s. The nominal scale factor of the sensor is 17.7 mV/º/s in a measurement range of ±100 º/s, with a full-scale nonlinearity of only 0.12%.

Tuning Fork Gyroscopes

Bosch company reported a yaw rate silicon micromachining sensor in 1998 [11]. This device can achieve amplitudes as large as 50 μm using a permanent magnet mounted inside a metal package. It was fabricated through a combination of bulk and surface micromachining processes. It consists of two bulk-micromachined oscillating masses and two surface-micromachined accelerometers. The sensitivity can achieve 18 mV/º/s. The device resolution is 0.3 º/s at a 100 Hz bandwidth because of the large amplitude. The large amplitude can increase output signal and power consumption. It also can cause fatigue problems over long-term operation. The mechanical suppression of the mechanical crosstalk between the oscillator and the Coriolis sensing accelerometer was

more than 8000. The temperature drift of the offset of the yaw rate sensor is less than 0.5 °/s without any temperature compensation.

Motivation for N-coupled Oscillator Gyroscopes

For the classic N-coupled resonators, equations of motion can be written as:

$$m\ddot{y}_n = -k_c(y_n - y_{n-1}) + k_c(y_{n+1} - y_n) - ky_n \tag{1.2}$$

where k_c is the coupling spring between the resonators, k is the spring constant of each resonator, $w_0 = \sqrt{\frac{k}{m}}$ and $w_c = \sqrt{\frac{k_c}{m}}$.

$$m\ddot{y}_n + (k + 2k_c)\, y_n - k_c y_{n-1} - k_c y_{n+1} = 0 \tag{1.3}$$

$$\ddot{y}_n + (w_0{}^2 + 2w_c{}^2)\, y_n - w_c{}^2 y_{n-1} - w_c{}^2 y_{n+1} = 0 \tag{1.4}$$

$$y = A_p \mathrm{Cos}(wt) \tag{1.5}$$

After plugging equation 1.5 into 1.4:

$$\frac{A_{p-1} + A_{p+1}}{A_p} = \frac{w_0{}^2 + w_c{}^2 - w^2}{w_c{}^2} \tag{1.6}$$

To solve equation 1.6, it should be assumed that:

$$A_p = C\sin(p\theta) \tag{1.7}$$

After replacing 1.7 into 1.6 it will be concluded that the mode shapes should be of the form of equation 1.8 for 32 coupled resonators:

$$A_p = C.\sin\left(\frac{pn\pi}{16}\right) \ \& \ C.\mathrm{Cos}\left(\frac{pn\pi}{16}\right) \tag{1.8}$$

where p is the resonator number and n is the mode shape number. The first mode shape is uniform motions of all the resonators together, which happens for n=0. After using equation 1.8 in 1.6 it can be concluded that the modal frequency of the system can finally be written in the form of:

$$w = \sqrt{w_0{}^2 + 4w_c{}^2 \ \sin^2\frac{n\pi}{32}} = w_0\sqrt{1 + 4\frac{k_c}{k} \ \sin^2\frac{n\pi}{32}} \tag{1.9}$$

This formula also works for n=0 where all the resonators move together. Figure 1.4 shows a plot of the natural frequency versus coupling ratio for different mode shapes. For n=16 adjacent resonators move in opposite directions.

There are two different methods to design a gyroscope with coupled oscillators. The first method is using the fact that wave propagation speed changes around a circular coupler in the presence of an external rotation. Figure 1.5 shows 32 resonators around a circle that are attached to the substrate from the cantilever. If the system is subjected to a

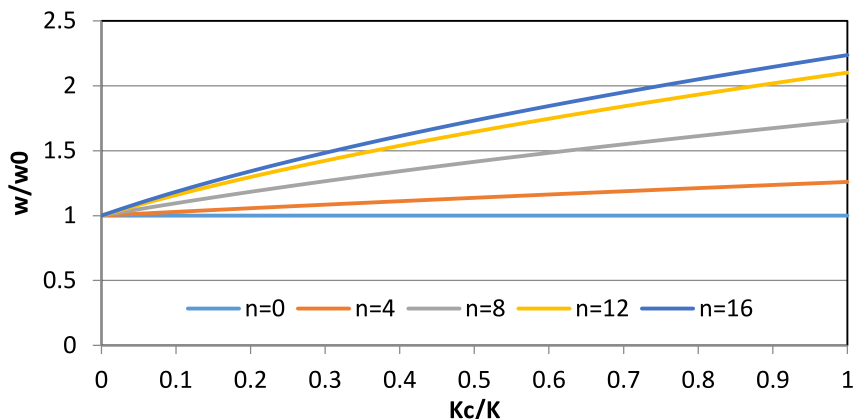

Fig 1.4: Ratio of natural frequency to the single cantilever natural frequency versus coupling ratio for five different mode shapes.

pulse from the top electrode, the first peak of vibration will travel gradually around the circle and the group velocity can be calculated. Figure 1.6 shows the transient response of the first four oscillators after applying a 1 µN force to the top resonator for 10µs.

The group velocity can be calculated from Figure 1.6 to be 12 m/s and it takes about 355 µs for the peak of vibration to reach the two sensors from both directions. At first, all the vibrational energy will be concentrated in the top resonator where the force is applied and gradually the vibrational energy will transfer to other resonators. As a wave until, all resonators will vibrate according a combination of excited mode shapes and then the vibration will be gradually damped by an energy loss mechanism until the system reaches an almost fixed position. Then another pulse will be applied and this happens repeatedly. If the gyroscope is rotated in this process, the peak of vibration reaches the two sensors at different times and by measuring the time lag, the external rotation can be cause a time lag and at the end of this time period the average external rotation can be

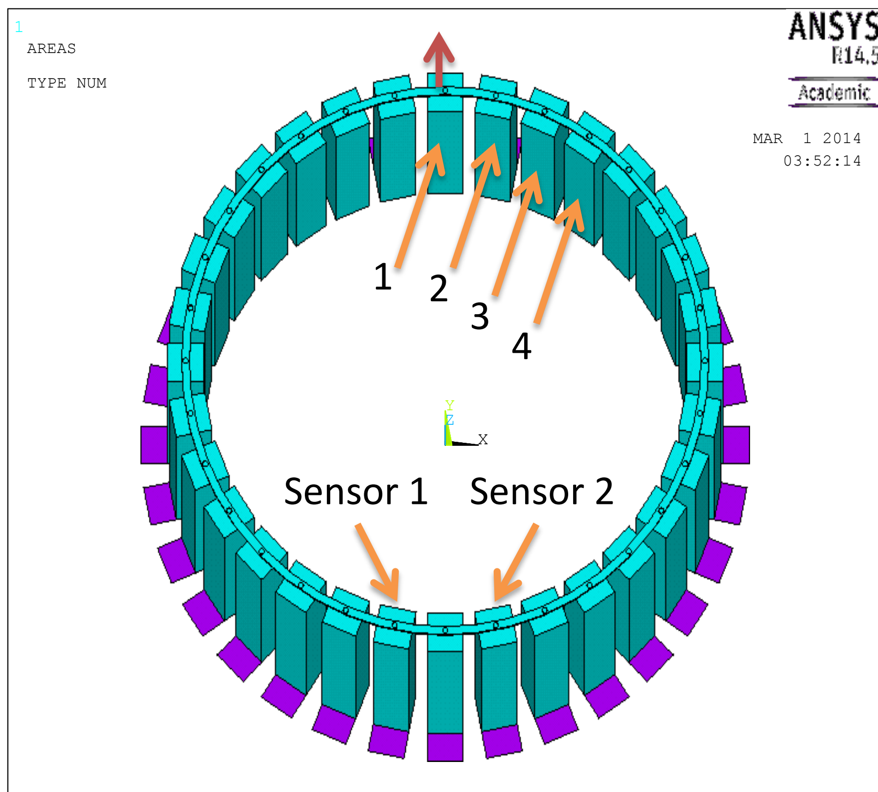

Fig 1.5: Coupled resonators subjected to a 10 μN pulse for 10 μs.

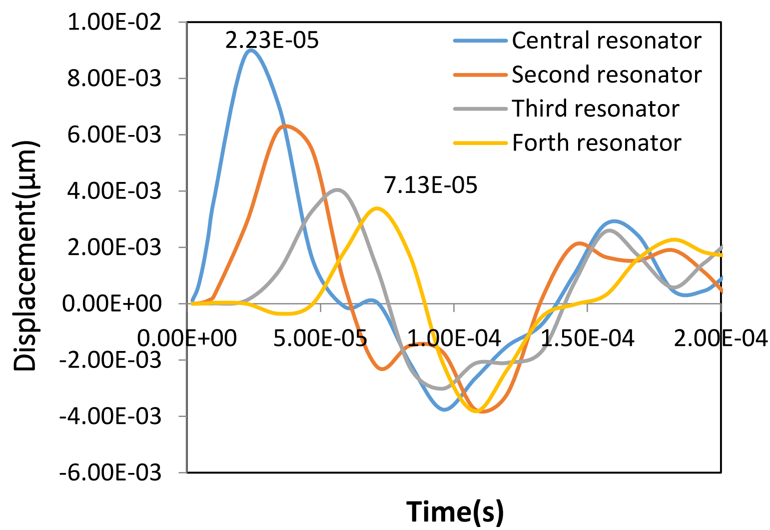

Fig 1.6: Transient response of the first four resonators with nickel cantilevers and SU8 polymer couplers.

calculated. Following this calculation period there is a damping down period which may be up to a few seconds. Increasing the effective damping of the system can reduce this damping down interval but it will not be eliminated completely.

Another way to use coupled resonators as a gyroscope is using them in combination of a ring type gyroscope. The discrete proof masses of the coupled oscillators increase the effective mass of the system while the effective spring constant is kept at low levels, which leads to lower natural frequencies and higher sensitivities. This method is explained further in the next chapter.

CHAPTER 2

CONCEPTUAL DESIGN

Conceptual Design cnd Fabrication Method

The gyroscope is comprised of a series of bulk mass oscillators connected together with a ring coupler. The resonators can be coupled from the top or from the base, see Figure 2.1. The simulations show the device will have higher sensitivity if the resonators are coupled together from the end in which they are not attached to the substrate. The principle of working of this gyroscope revolves around having two mode shapes with almost the same natural frequency that have 45 degrees difference in

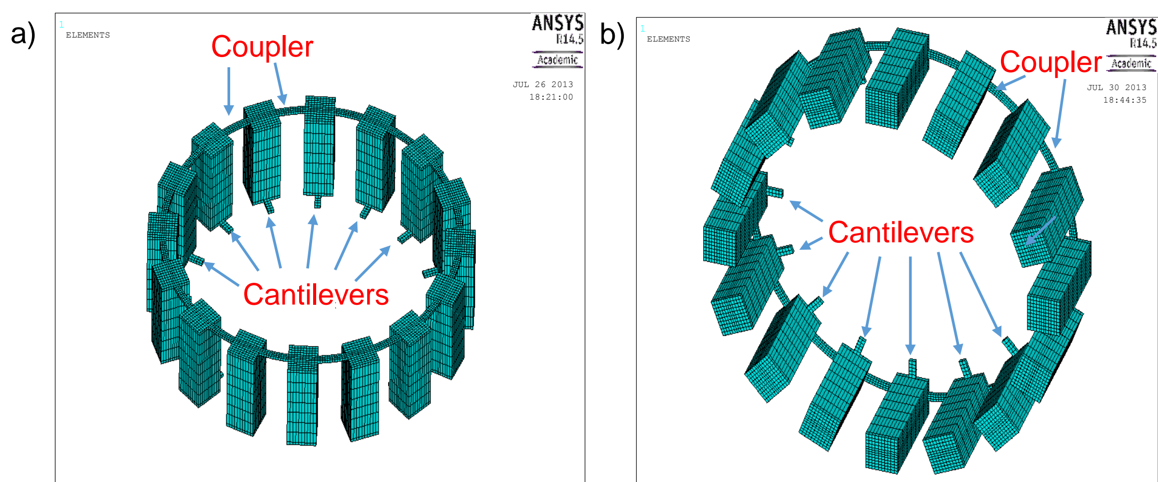

Fig 2.1: Different methods of coupling the resonators. (a) From the top end, (b) from the bottom end.

direction, see Figure 2.2. When a rotation around the axis of the gyroscope happens, all of the resonators contribute to starting a secondary vibration along the other direction which is 45 degrees tilted from the excitation direction (Figure 2.3). All the proofmasses cooperate in giving rise to secondary vibrational motion either directly, or by squeezing the ring coupler, or a combination of these two actions. The difference of this gyroscope with other hemispherical gyroscopes is that the cantilevers can be accessed and can be

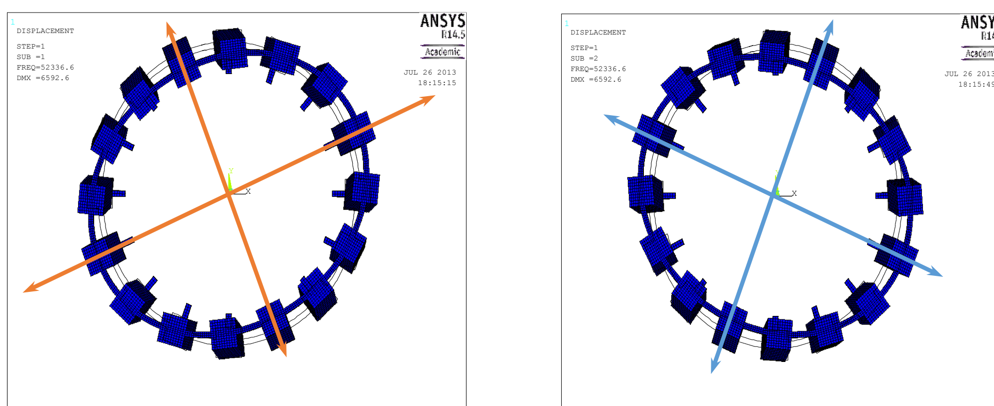

Fig 2.2: Two mode shapes with 45 degrees difference in orientation. Natural frequency is 52336 Hz for this model's dimensions.

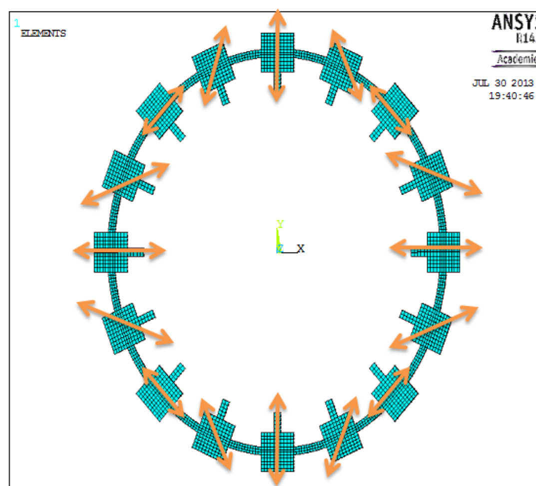

Fig 2.3: Velocity directions are shown with orange arrows and Coriolis force with yellow arrows around the ring gyroscope.

improved to increase the quality factor. The mass of the structure can also be increased without changing the spring constant to increase the sensitivity of the gyro. This gives the designer open hands to design different gyroscopes for different applications. In order to microfabricate this complicated structure from silicon, deep reactive ion etching (DRIE) method should be used from both sides of the wafer. The coupler and cantilevers can be made out of single crystal silicon, silicon nitride, silicon oxide, nickel and other metals or polymers and the rest of the structure is made out of silicon. At first the coupler is deposited and patterned (Figure 2.4.a). Then a Cr layer is deposited on the bottom side and patterned by lithography to be used as a mask to etch silicon (Figure 2.4.b). Then the chip is flipped and a Ni layer is deposited on the top surface and patterned to form a circular opening on it. This is used as a mask to do DRIE from the top side till an opening is seen on the other side, while anchor cantilevers are still untouched (Figure 2.4.c). Then Ni mask is removed and from the bottom side the first DRIE etch is continued till the coupler is reached (Fig 2.4.d). At the end the bottom Cr mask is removed by etchant. In this way only one side of the proof mass is formed from the top side and the three other sides will be formed from the bottom side. If there is a misalignment of the top and bottom mask, the mass of proof masses may change slightly but a fabrication sequence can be used in which two opposite sides of the proof mass are fabricated from the top and the other two from the bottom. This minimizes the misalignment effect on the final size of proof mass. This method is explained later in Appendix A. The bonding to glass step and fixed electrode formation are not shown in this fabrication sequence. To increase the sensitivity it is better to increase the size of proof masses and make them as close to each other as possible. Because of the small gaps between large proofmasses the size of

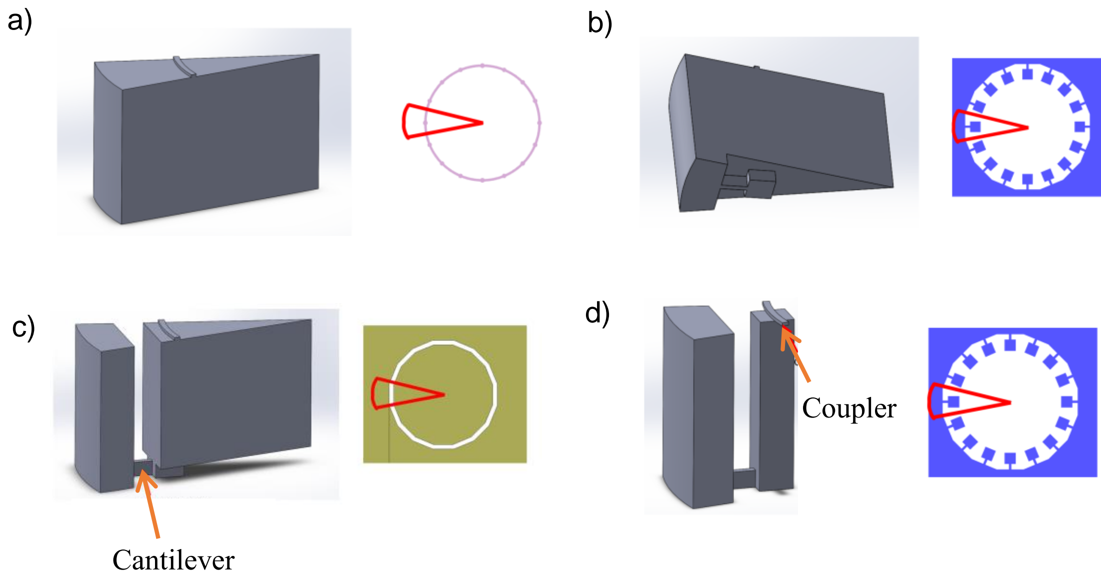

Fig 2.4: Fabrication sequence of the device. Only one sector of the device is shown so that it is easier to visualize the fabrication steps. Next to each step the mask that is used in that step is shown, with the location of sector region highlighted.

the couplers connecting the proofmasses together will decrease substantially, leading to high coupling stiffness which is not desirable. To overcome this issue, sacrificial layers can be used so that the couplers connect the center point of the proofmasses only and do not touch other parts of the system, Figure 2.5. In this way, the length of the couplers will be independent of the proofmass size.

Sensitivity Increase Concept

The device that is going to be designed, analyzed and simulated in this work is a N-Coupled oscillator gyroscope, which has both characteristics of coupled oscillators and ring-type micro gyroscopes. There is not a similar device to what is going to be designed, so in order to compare it with previous works it can only be compared

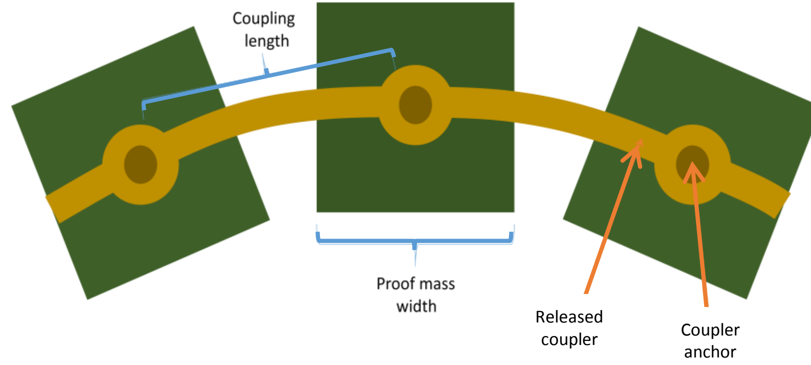

Fig 2.5: Connection of proofmasses to the couplers from the central points to decrease natural frequency and increase sensitivity of the device.

separately to coupled oscillators, ring type, disk type and cylindrical gyroscopes.

The first paper that is compared to our design is article [12]. This paper investigates the main source of acceleration sensitivity of tuning fork gyroscopes. The frequency response of in-plane coupled resonators is used for investigating the acceleration sensitivity of a MEMS tuning fork gyroscope (TFG) and a new method of suppressing the acceleration output is presented. The unbalancing of two sense resonators in the TFG caused by fabrication errors converted an external vibration into antiphase mode excitation. To reduce the acceleration output, decoupling between in-phase and antiphase modal frequencies is crucial and is done by increasing the decoupling ratio (DR), since coupled resonators may cause large antiphase vibrations from the acceleration.

$$DR = \frac{f_{anti} - f_{in}}{f_{anti}} \tag{2.1}$$

The main goal of article [12] is canceling the acceleration sensitivity of tuning fork gyroscopes. TFG has two drive masses vibrating in opposite directions which results in Coriolis motions to also be in opposite directions. If a differential amplifier is used to measure the final output of the sensors and two resonators are identical, an external vibration in the direction of sensing motions will move the sensing elements equally. This will be eliminated in the differential amplifier. However, if fabrication imperfections are introduced, small output is added to the Coriolis signal. This is due to the fact that vibrational output of the system is the weighted sum of different mode shapes and since the stiffness in the two resonators are not the same in practice, the force needed to oscillate the system with the same amplitude in the same direction in a way that the differential amplifier does not sense it, is not equal. So if an equal force because of external acceleration is applied to both of the resonators, the out-of-phase mode shape will also be excited. The amplitude of this unwanted motion is related to the decoupling ratio and how close the frequency of the acceleration is to antiphase frequency. In case of an external impulse in the sense direction, two sense masses will oscillate with slightly different periods and amplitudes which gradually give rise to out-of-phase motion until it is damped out.

The acceleration output model was verified using two coupled resonators with 1 and 5% stiffness unbalance. Finite elements method simulation results show a 25% reduction in the antiphase vibration by increasing the decoupling ratio from 0.09 to 0.29, irrespective of the coupled resonators designs. Quantitative analysis of a TFG based on coupled resonators with 1% stiffness unbalance shows the acceleration output decreasing from 5.65 to 1.43 °/s/g. The first two mode shapes of a ring gyroscope have 45 degree

difference in orientation. In Figure 2.6, mode shapes number three and four are shown, which have 90 degree difference in orientation. In our design, mode shape 1 and 2 are considered the out-of-phase motion and mode shapes 3 and 4 the in-phase motion. Natural frequencies are 52336 Hz for mode shapes 1 and 2 and 53843 Hz for mode shapes 3 and 4. It can be seen, there is a 1.5 KHz difference between natural frequencies. The frequency difference and also the decoupling ratio can be increased by reducing the thickness of anchor cantilevers, because in this way the stiffness ratio between the cantilevers and the couplers will decrease.

The sensitivity in a single mass MEMS gyroscope with perpendicular drive and sense directions is derived here. For the ring-type gyroscope the same equations are expected with a different coefficient. The vibration amplitude in the drive direction can be written as:

$$U = Q_d \frac{F_d}{K_d} \tag{2.2}$$

In order to increase the drive amplitude, the spring constant should be decreased as much as possible and the driving force should be increased. To increase the driving force the gap can be decreased or the area can be increased. Increasing area is a better choice since by decreasing the gap a limit will be set on the vibration amplitude and the fabrication process also gets harder. The Coriolis force that drives the sense direction motion is:

$$F_c = -2m_c \Omega_z U w_d \tag{2.3}$$

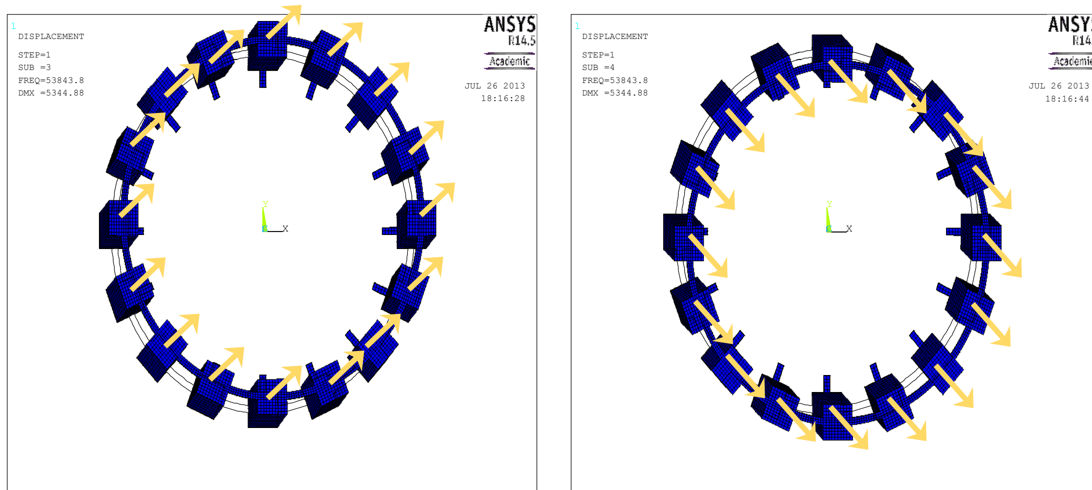

Fig 2.6: Two mode shapes with 90 degrees difference in orientation. Natural frequency is 53843 Hz for the model dimensions.

where m_c is the resonator mass that moves in the sense direction, Ω_z is the input rotation and w_d is the drive frequency. The sense vibration amplitude in the mode-matched condition would also be:

$$O = Q_s \frac{F_c}{K_s} = 2m_c\Omega_z w_d \frac{Q_s Q_d}{K_s K_d} F_d \tag{2.4}$$

From formula 2.4, it can be clearly seen that for achieving higher sensitivities the spring constant of the system should be decreased and the mass and electrode area should be increased, which is the main approach of this work. In the following pages this work is compared with three other designs and it is explained how it can be superior to them.

The first design is a simple ring micro gyroscope [5]. The system is comprised of a silicon ring and radial springs that connect the structure to the central hub. In this paper, a single crystal silicon (SCS) vibrating ring gyroscope with high aspect ratio, silicon on

glass structure was designed, fabricated and tested. The ring is 2.7mm in diameter and 150μm thick. The gyro has the following measured performance: high Q (12000), good nonlinearity (0.02%), large sensitivity (132 mV/°/sec), low output noise (10.4°/hr/$\sqrt{Hz}$) and high resolution (7.2°/h). The maximum bias shift is less than ± 1°/sec over 10 hours without thermal control. This is a very high performance design, but the driving amplitude is 0.123 μm and can be increased. The sense gap is 8 μm, which is good enough. The spring constant can be increased further and the mass of the system can be increased substantially in order to reach lower frequencies and higher sensitivities. To decrease the spring constant, a low thickness ring can be used on top of our structure and the thickness of the base anchor cantilevers can be decreased.

One way to increase the mass is using bulk acoustic wave (BAW) sensors. The second design is a BAW gyroscope sensor [13]. In this paper, a 800µm diameter center-supported single crystal silicon disk gyroscopes operating in high order elliptical bulk acoustic modes at 5.9MHz is presented. The BAW gyroscope was fabricated on 50µm thick SOI using the high aspect ratio combined poly and single crystal silicon (HARPSS) process to obtain 250 nm capacitive gaps. It exhibited ultrahigh Q in excess of 200,000. The Brownian noise of Coriolis vibratory gyroscope is:

$$\sigma = \frac{1}{U}\sqrt{\frac{4K_BT}{f_0MQ}} \tag{2.5}$$

where K_B is Boltzmann constant, T is temperature in kelvin and U is drive amplitude. So

by using a bulk acoustic wave sensor, M, Q and f_0 can be increased. This leads to lower noise levels, but there are two draw backs here. Although mass is increased in this design, spring constant is also increased substantially so according to equations 2.2 and 2.4, U and sensitivity are decreased although bias instability is decreased. Sensitivity of this device is reported to be 0.19 mV/°/sec and bias instability is 0.175 °/Sec. Compared to the previous ring-type gyro, it can be seen that sensitivity is 700 times lower but bias instability is 6 times better. The main reason for this huge decrease in sensitivity is the high spring constant of the structure. In this thesis the spring constant is decreased substantially while large proofmasses are still being used, because they are not coupled together anymore and the dimensions of each of them can be changed separately.

The last and the third design that will be discussed is similar to disk resonator plus several round trenches in the structure by which designers tried to decrease the spring constant of the system while having a large mass [14]. This paper reports the architecture and operation of a single-crystal cylindrical rate-integrating gyroscope (CING). The attractive features of the CING include mode stability due to the separation of the wineglass modes from the in-phase-parasitic modes, self-alignment of sensor components and fabrication. The CING is built using a silicon on glass (SOG) process using a (111) Si wafer. It operates at 17.9 KHz and has an average Q of 21,800. It is reported that the bias stability is 0.16 °/sec, which is slightly better than the previous two designs, but sensitivity of the gyro is not reported. The proofmass is separated in the radial direction, but in this thesis it is separated tangentially; thus, it is expected to be more compliant with a better sensitivity.

Quality Factor Enhancement Techniques

In a one degree of freedom mass-spring-dashpot system the differential equation that governs the motion is [15]:

$$\ddot{x} + 2\zeta\omega_n\dot{x} + \omega_n{}^2 x = \frac{F(t)}{m_{eq}} \tag{2.6}$$

and one can write the quality factor to be:

$$Q = \frac{1}{2\zeta} = \frac{m_{eq}\omega_n}{C_{eq}} = \frac{\sqrt{km_{eq}}}{C_{eq}} \tag{2.7}$$

Based on this formula it might be assumed that it is necessary to increase both the mass and the spring constant to increase the quality factor. However, what actually happens is more complicated than that because the denominator also will increase when the mass and spring constant are increased. When mass is increased, usually the surface area and air damping are also increased; and when spring constant is increased, a term named anchor loss is also increased considerably which will increase C_{eq}. The quality factor can be written as [16]:

$$\frac{1}{Q} = \frac{1}{Q_{TED^1}} + \frac{1}{Q_{support}} + \frac{1}{Q_{surface}} \tag{2.8}$$

---

[1] Thermo elastic damping

The support loss damping ratio can also be written as [17]:

$$\zeta_{support} = 0.23\,\frac{h^3}{l^3} \tag{2.9}$$

So it can be concluded:

$$Q_{Support} = \frac{1}{2\zeta_{support}} = 2.174\,(\frac{l}{h})^3 \propto \frac{1}{K} \tag{2.10}$$

There is another formula which shows the same proportionalities with a slight change in the coefficient [16]:

$$Q_{Support} = \left[\frac{0.24(1-\nu)}{(1+\nu)\psi}\right]\frac{1}{(\beta_n\chi_n)^2}\left[\frac{L}{b}\right]^3 \propto \frac{1}{K} \tag{2.11}$$

Our goal is to decrease the spring constant of the system to reduce the support loss. Air damping can also be eliminated by reducing the working pressure of the resonators. It should be noted that equations 2.10 and 2.11 are for a beam that does not have a proofmass at its end. If we increase the mass of the system the natural frequency goes down, which leads to higher sensitivity, but the support loss will increase causing a reduction in the quality factor of the system. To solve this problem, different techniques can be used on the side to reduce the anchor loss. One of them is using Mesa isolations [18], which are basically a trench around the anchor area that reflects back the acoustic waves into the system. A trench can be fabricated around our anchor cantilevers to

increase the Q. Depending on the distance of the trench from the cantilever base, reflecting waves can have a constructive or destructive effect which increase or decrease the Q, respectively. Optimum distance should be found experimentally. A 400% increase in Q has been shown using this method.

Another method for reducing the support loss is using material mismatch [19]. In this method to increase the Q the resonator is made from one material and another material is used for the support or the anchor (Figure 2.7). The different acoustic velocities of these dissimilar materials create an impedance mismatch at the resonator-support interface that attenuates energy transfer from the vibrating resonator to the

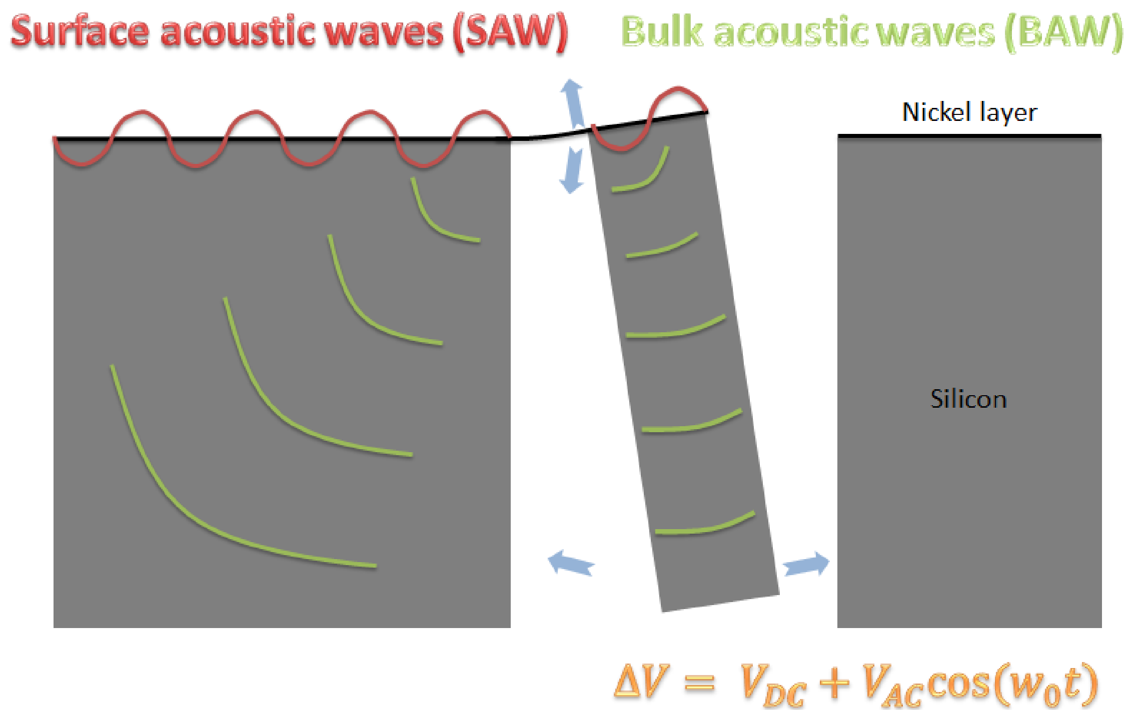

Fig 2.7: Acoustic waves propagating away through the anchors of the resonator causing a leak of energy.

support, thus, allowing the resonator to retain its vibrational energy and exhibit high Qs. In contrast, resonators that use identical materials for support and resonator will have a perfect impedance match between the two. This allows maximum power transfer from the resonator to the support, thereby allowing significant loss from the resonator, through the support, to the substrate, resulting in substantially lower Q values. Using SOI wafers is a good example of this method.

Phononic crystal strips can also be incorporated in designing our anchors to suppress wave propagation to the support [20]. Some of the pass bands may exist as the so-called deaf bands in which certain types of incident waves can be nearly totally reflected by the phononic crystal. In other words, these structures can be used as lossless anchors if they are used in the right working frequency and place. A series of etch holes will also show the same blocking effect for acoustic waves in certain frequency bands. This method is more suitable for high frequency applications in GHz, so probably this method will not be used in our design.

Figure 2.8 shows a bulk mass resonator that has a series of etched holes near the anchor to block the propagation of acoustic waves that transfer out the vibrational energy from the resonator. There is also a mesa isolation which is the step around the etched hole area that reflects back some part of the acoustic waves to the resonator. The dimensions of the mesa isolation should be changed experimentally to find out at what distance the quality factor is higher. SOI wafer can be used to increase the quality factor further, but it will complicate the electrical connection to the resonator [21, 22]. The structure is comprised of two rigid fixed blocks and one middle oscillator block that is connected to one of the blocks by a cantilever beam. Since the DRIE method is used from both sides of

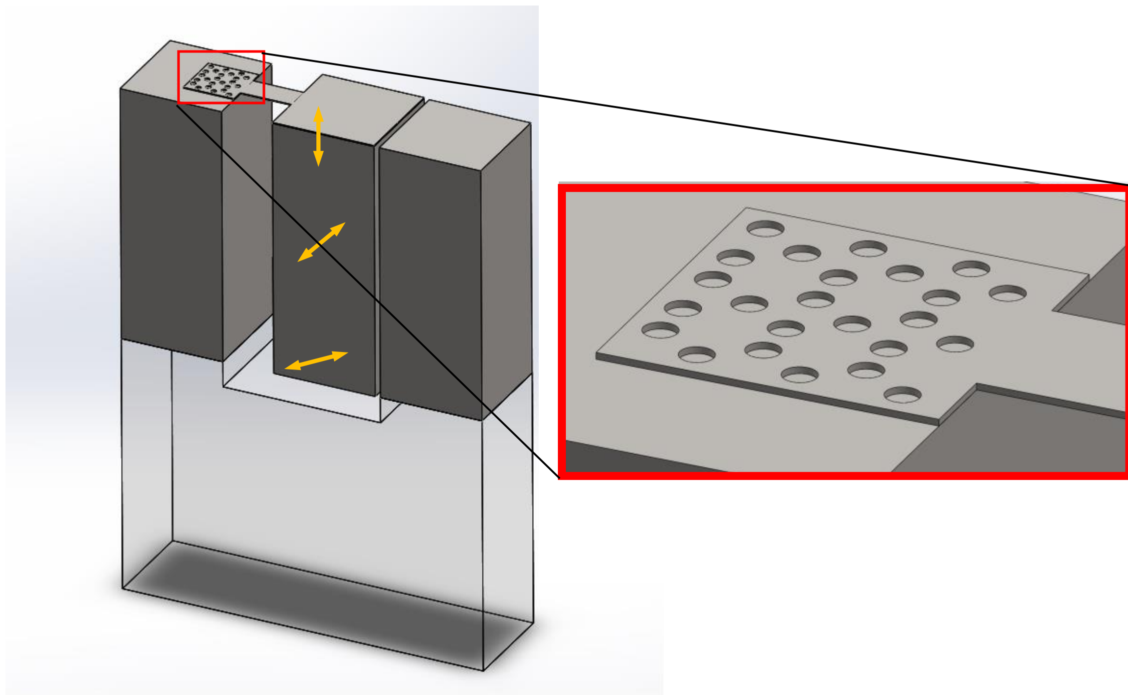

Fig 2.8: Proposed bulk mass resonator with driving electrode bonded over a glass wafer with a trench.

the wafer, the anchor area can be accessed for some changes to reduce the energy leakage. The gap distance is 10 µm and the AC voltage is applied between the two fixed blocks through the electrical pads. The glass wafer is bonded to a silicon wafer which is highly doped. The yellow arrows show the oscillation direction of different parts of the resonator.

The Effect qf Using Multiple Resonators y ith Resonant Frequency Shifts kn vhe Drive Mode

If in the coupled resonators a slight frequency shift is introduced in each device, the system response curve will have wider peak in resonance. A very good example is

reference [23]. Since the Coriolis force, and the sense-mode response is directly proportional to the drive-mode oscillation amplitude, it is desired to enhance the drive-mode amplitude by increasing the Q factor with vacuum packaging and operating at the peak of the drive-mode resonance curve. However, large drive-mode amplitude and bandwidth cannot be achieved with a 1-DOF drive system at the same time. The proposed approach explores the possibility of increasing the drive-mode response bandwidth of micromachined gyroscopes, by utilizing multiple resonators with incrementally spaced resonant frequencies in the drive mode.

Optimum Number qf Resonators

In different systems different approaches should be taken to figure out the optimum number of resonators. For example, in this thesis design, if a few coupled resonators are used then each proofmass will have larger dimensions and if lots of coupled resonators are used, they cannot have big sizes anymore. In a ring gyroscope, at least eight resonators should be used to balance the system, because separate resonators are needed in front of the sense and drive electrodes and if the system is rotated 45 degrees a similar structure should be reached to minimize frequency mismatch between sense and drive. If it is necessary to use more resonators, a multiple of eight resonators should be used to make sure appropriate driving and sensing resonators are in place. As a more general rule, if a 4 node mode shape is used for driving and sensing, then a multiple of eight resonators should be used [5] and if a 6 node mode shape is used, then a multiple of 12 resonators should be used [13], and so on. Our goal is achieving minimum natural frequency to gain higher sensitivities. If it is assumed the coupler dimensions, cantilever

thickness and length are fixed, the width of cantilever and proof mass are equal and the minimum gap between the corners of adjacent resonators is kept to be a constant value, e.g., 50 µm, as the number of resonators increase by eight increments, from 8 to 64, it can be expected that the effective mass and effective spring constant of the system, both decrease. However, it is not evident how the natural frequency will behave. It is a good practice to use finite element methods (FEM) simulation softwares to find out what the optimum number of resonators will be. As the number of resonators around the circle increase the capacitor area will decrease, so multiple resonators may be needed for driving or frequency tuning. If a lower number of resonators is used because of wider cantilevers, the sensitivity of the system to the same amount of misalignment between the masks will reduce. By using larger capacitors, fewer resonators will be needed for driving and frequency tuning purposes. In this thesis the number of resonators is not optimized because the frequency of the system can always be reduced by using thinner cantilevers and couplers, or increasing the diameter of the coupler. Sixteen resonators were used for initial simulations; then, to find the final dimensions and characteristics, 32 resonators were used.

The Effect qf Coupling

When zero coupling is used the resonators will work separately with respect to each other and when the coupling is increased very much, a continuous cylindrical structure will be reached. Between these two extreme cases, where there are discrete resonators coupled weakly together with a ring coupler from the top end, is our working point. In this thesis silicon, nickel and SU8 couplers with different dimensions are used in

simulations. If the stiffness of the coupler is changed, the ratio of frequency of parasitic mode shapes to the drive and sense frequency will also change, which affects noise level directly.

CHAPTER 3

MODELING

Frequency of a Single Oscillator Versus Cantilever Thickness

The capacitive actuator that is going to be modeled is shown in Figure 3.1. These actuators can be used to design low frequency gyroscopes with very high sensitivity. One single oscillator can be modeled with a spring mass system by assuming the cantilever is rigid and connected to a rotational spring, as shown in Figure 3.2. The pivot point would be between 1/2 and 2/3 of the length of the cantilever depending on the loading conditions from pure moment to pure transverse load.

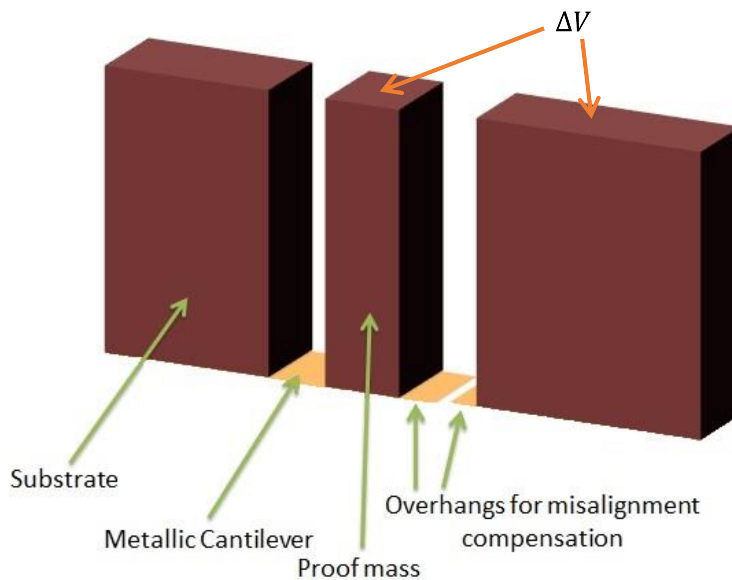

Fig 3.1: Three-dimensional model of the actuator.

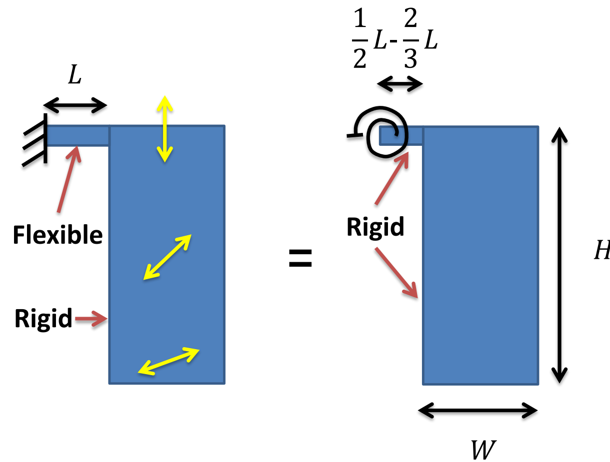

Fig 3.2: Modeling of the resonator with a rotational spring pendulum system.

Frequency Analysis

The natural frequency of the system would be:

$$f_0 = \frac{1}{2\pi}\sqrt{\frac{K_\theta}{I_\theta}} \tag{3.1}$$

where K_θ and I_θ are derived in equations 3.2 and 3.3.

$$K_\theta = \frac{EI}{L} = \frac{EWh^3}{12L} \tag{3.2}$$

$$I_\theta = \frac{1}{12}M(W^2 + H^2) + M\left((\frac{W}{2} + \frac{1}{2}L)^2 + \frac{H^2}{4}\right) \tag{3.3}$$

The reason half the length of the cantilever is used for the pivot point in equation

3.3, is that the loading condition on the cantilevers is a combination of axial force and a moment without any transverse loading. If the frequency versus cantilever thickness using equation 3.1 to 3.3 is plotted and then compared to the ANSYS simulation, for a square proof mass with a width of 140 μm, height of 530 μm and a cantilever with the width and length of 50 μm, Figure 3.3 will be reached.

In Figure 3.3, it can be seen that there is a close agreement between the calculated natural frequency of the resonator and ANSYS simulation which shows that our analytical model is suitable for predicting the resonator behavior. The difference is about 20%, which is typical in finite elements method simulations.

Electromechanical Analysis

In order to model the system shown in Figure 3.1, the cantilever is replaced with a rotational spring like Figure 3.2. Then, only one side of the bulk resonator which is in front of the fixed electrode is considered to reach a two-dimensional model, like Figure

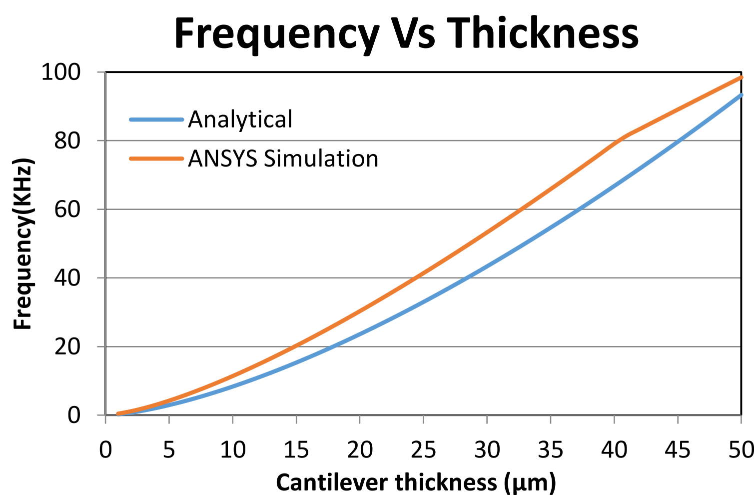

Fig 3.3: Natural frequency of the bulk mass resonator using analytical formulation compared to ANSYS simulation.

3.4. The in-plane width of the capacitor, which is not shown, is considered as w. As you can see in Figure 3.4, in this two-dimensional model the position of the pivot point is shifted from Figure 3.2 to the right corner. In small displacements, especially if the height of the resonator is much bigger than its width, the vertical motion effect in the capacitance change is negligible so it can be neglected and the rotational spring can be moved to the right corner. This assumption is only valid when electrical forces or moments are being calculated and should not be used for calculating the frequency of the system since the rotational moment of inertia will change in this way. When a voltage difference of V is applied between the two electrodes, the moving electrode will start rotating until it reaches the equilibrium state where the tip of the moving electrode is moved the distance x. The capacitance of the resonator as a function of x can be computed as follows:

$$C_x = \int dC = \int_0^l \frac{\varepsilon w}{d-f} dy = \int_0^l \frac{\varepsilon w}{d - \frac{xy}{l}} dy$$

$$= -\frac{\varepsilon w l}{x} \ln\left(d - \frac{xy}{l}\right)\Big|_0^l = -\frac{\varepsilon w l}{x}[\ln(d-x) - \ln d]$$

$$= \frac{\varepsilon w l}{x} \ln\left(\frac{d}{d-x}\right) \tag{3.4}$$

Now the force and moment in Figure 3.5 can be computed:

$$\frac{\partial C_x}{\partial x} = -\frac{\varepsilon w l}{x^2} \ln\left(\frac{d}{d-x}\right) + \frac{\varepsilon w l(d-x)}{d.x} \frac{d}{(d-x)^2} = \frac{\varepsilon w l}{x^2} \ln\left(1 - \frac{x}{d}\right) + \frac{\varepsilon w l}{x(d-x)} \tag{3.5}$$

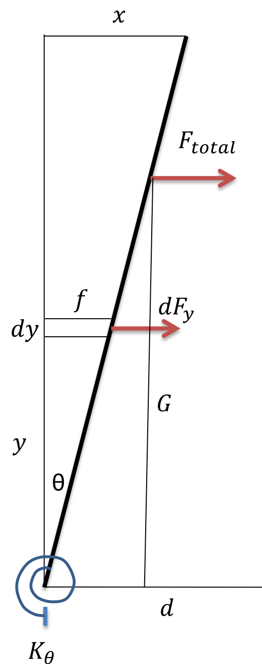

Fig 3.4: Two-dimensional model of the actuator.

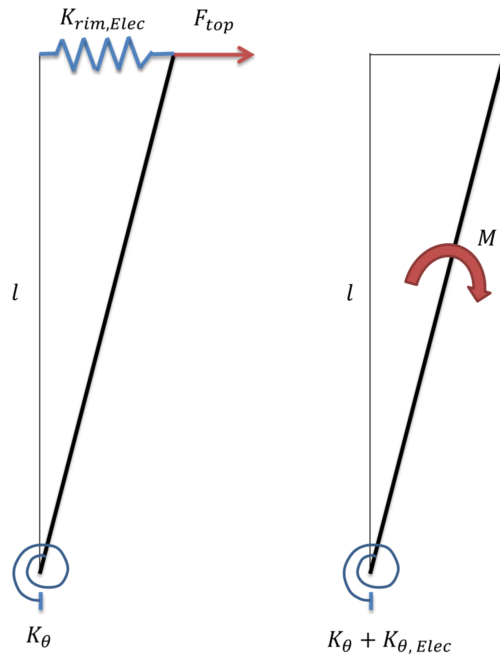

Fig 3.5: Two-dimensional equivalent model of the actuator by replacing the fixed electrode with a force and a negative spring constant linear spring, or a moment and a negative spring constant rotational spring.

$$F_{Top} = \frac{1}{2}\left(\frac{\partial C_x}{\partial x}\right)V^2 = \frac{1}{2}\left(\frac{\varepsilon wl}{x^2}\ln\left(1-\frac{x}{d}\right)+\frac{\varepsilon wl}{x(d-x)}\right)V^2 \quad (3.6)$$

$$M = F_{Top}.l = \frac{l}{2}\left(\frac{\partial C_x}{\partial x}\right)V^2 = \frac{1}{2}\left(\frac{\varepsilon wl^2}{x^2}\ln\left(1-\frac{x}{d}\right)+\frac{\varepsilon wl^2}{x(d-x)}\right)V^2 \quad (3.7)$$

F_{total} can be calculated as:

$$dF_y = \frac{V^2}{2}.\frac{\partial(dC)}{\partial f} = \frac{V^2}{2}.\frac{\partial(dC)}{\partial x}.\frac{\partial x}{\partial f} = \frac{V^2}{2}.\frac{\partial}{\partial x}\left(\frac{\varepsilon w.dy}{d-\frac{xy}{l}}\right).\frac{l}{y} = \frac{\varepsilon wV^2}{2\left(d-\frac{x}{l}y\right)^2}.dy \quad (3.8)$$

$$F_{total} = \int dF_y$$

$$= \frac{\varepsilon wV^2}{2}\int_0^l \frac{dy}{(d-\frac{x}{l}y)^2}$$

$$= \frac{\varepsilon wV^2}{2}\left(\frac{l}{x}\right)\frac{1}{\left(d-\frac{x}{l}y\right)}\Bigg|_0^l = \frac{\varepsilon wlV^2}{2x}\left[\frac{1}{d-x}-\frac{1}{d}\right] = \frac{\varepsilon wlV^2}{2d(d-x)} \quad (3.9)$$

The moment can be also calculated by integrating the $dF_y.y$ over the length of the moving electrode.

As can be noted, formula 3.10 is identical to formula 3.7. To find G it is only needed to divide moment by total force as shown in formula 3.11.

The ratio $\frac{x}{d}$ can be named as the unit less parameter α ($0 < \alpha < 1$) and equation 3.11 can be written as equation 3.12.

Figure 3.6 shows that when the electrode is not moved yet the resultant force is in

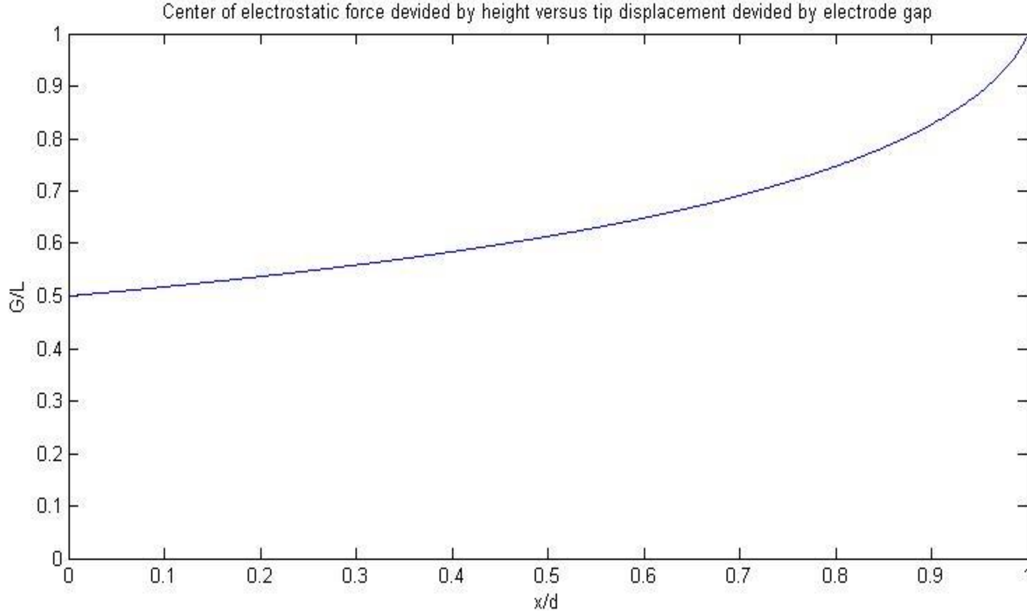

Fig 3.6: Location of resultant force versus displacement of the electrode tip.

$$M = \int_0^l \frac{\varepsilon w V^2}{2} . \frac{y}{\left(d - \frac{x}{l} y\right)^2} dy = \int_0^l \frac{\varepsilon w V^2}{2} . \left(-\frac{l}{x}\right) . \frac{-\frac{x}{l} y + d - d}{\left(d - \frac{x}{l} y\right)^2} dy$$

$$= \frac{\varepsilon w V^2}{2} . \left(-\frac{l}{x}\right) . \left[\int_0^l \frac{1}{\left(d - \frac{x}{l} y\right)} dy + \int_0^l \frac{-d}{\left(d - \frac{x}{l} y\right)^2} dy \right]$$

$$= \frac{\varepsilon w V^2}{2} . \left(-\frac{l}{x}\right) . \left[\left(-\frac{l}{x}\right) \ln\left(d - \frac{x}{l} y\right) \Big|_0^l + \left(-\frac{ld}{x}\right) \frac{1}{(d - \frac{x}{l} y)} \Big|_0^l \right]$$

$$= \frac{\varepsilon w V^2 l}{2x} . \left[\left(\frac{l}{x}\right) \ln\left(\frac{d - x}{d}\right) + \left(\frac{l}{d - x}\right) \right] \tag{3.10}$$

$$G = \frac{M}{F_{total}} = \frac{ld(d - x)}{x^2} \ln \frac{d - x}{d} + \frac{ld}{x} \tag{3.11}$$

$$\frac{G}{l} = \frac{1 - \alpha}{\alpha^2} \ln(1 - \alpha) + \frac{1}{\alpha} \tag{3.12}$$

the center of the electrode because of uniform electrical load profile. As the electrode tip approaches the other electrode the position of resultant force gradually moves from the center to the top. This makes sense because as the gap closes the top part will be attracted to the other electrode with higher forces but dF_y on the lower parts does not change as much. In a similar fashion to G, M and F_{Top} can also be written in terms of the dimensionless parameter α:

$$F_{Top} = \frac{1}{2}\left(\frac{\varepsilon wl}{x^2}\ln\left(1-\frac{x}{d}\right)+\frac{\varepsilon wl}{x(d-x)}\right)V^2 = \frac{\varepsilon wlV^2}{2d^2}\left[\frac{1}{\alpha^2}\ln(1-\alpha)+\frac{1}{\alpha(1-\alpha)}\right] \quad (3.13)$$

$$M = F_{Top}.l = \frac{\varepsilon wl^2V^2}{2d^2}\left[\frac{1}{\alpha^2}\ln(1-\alpha)+\frac{1}{\alpha(1-\alpha)}\right] \quad (3.14)$$

Formulas 3.13 and 3.14 are both nonlinear and are not suitable for linear vibrational analysis of the resonator. The two following Taylor series can be used to simplify these formulas for small displacements.

$$\ln(1-\alpha) = -\sum_{n=1}^{\infty}\frac{\alpha^n}{n} = -\left(\alpha+\frac{\alpha^2}{2}+\frac{\alpha^3}{3}+\frac{\alpha^4}{4}+\cdots\right) \quad (3.15)$$

$$\frac{1}{1-\alpha} = \sum_{n=0}^{\infty}\alpha^n = 1+\alpha+\alpha^2+\cdots \quad (3.16)$$

Using equations 3.15 and 3.16 the first-order and second-order approximation for

moment and force around the equilibrium point can be found.

Figures 3.7 and 3.8 show the actual electrostatic force on the actuator versus displacement. From Figures 3.7 and 3.8, it can be concluded that the behavior of the system can be approximated by a linear negative spring very well as long as $\alpha < 0.1$; however, for $\alpha > 0.5$, the linear approximation is much different to the actual behavior of the system.

$$F_{Top} = \frac{\varepsilon w l V^2}{2d^2}\left[\frac{1}{\alpha^2}\ln(1-\alpha) + \frac{1}{\alpha(1-\alpha)}\right]$$

$$= \frac{\varepsilon w l V^2}{2d^2}\left[\frac{1}{\alpha^2}\left(-\alpha - \frac{\alpha^2}{2} - \frac{\alpha^3}{3} - \frac{\alpha^4}{4}\right) + \frac{1}{\alpha} + \frac{1}{1-\alpha}\right]$$

$$= \frac{\varepsilon w l V^2}{2d^2}\left[\left(-\frac{1}{\alpha} - \frac{1}{2} - \frac{\alpha}{3} - \frac{\alpha^2}{4}\right) + \frac{1}{\alpha} + 1 + \alpha + \alpha^2\right]$$

$$= \frac{\varepsilon w l V^2}{2d^2}\left[\frac{1}{2} + \frac{2\alpha}{3} + \frac{3\alpha^2}{4}\right] \quad (3.17)$$

$$M = F_{Top}.\,l = \frac{\varepsilon w l^2 V^2}{2d^2}\left[\frac{1}{2} + \frac{2\alpha}{3} + \frac{3\alpha^2}{4}\right] \quad (3.18)$$

From equations 3.17 and 3.18 the negative linear and rotational spring constants in Figure 3.5 can be derived:

`

$$K_{rim,Elec} = -\frac{\varepsilon w l V^2}{3d^3} \quad (3.19)$$

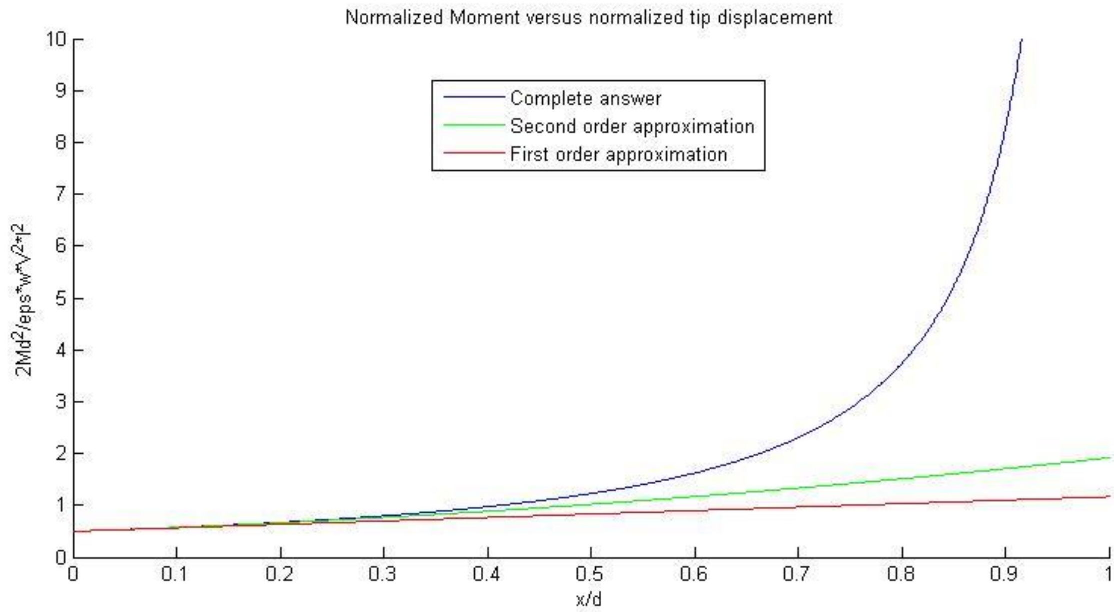

Fig 3.7: Dimensionless moment versus dimensionless electrode tip displacement.

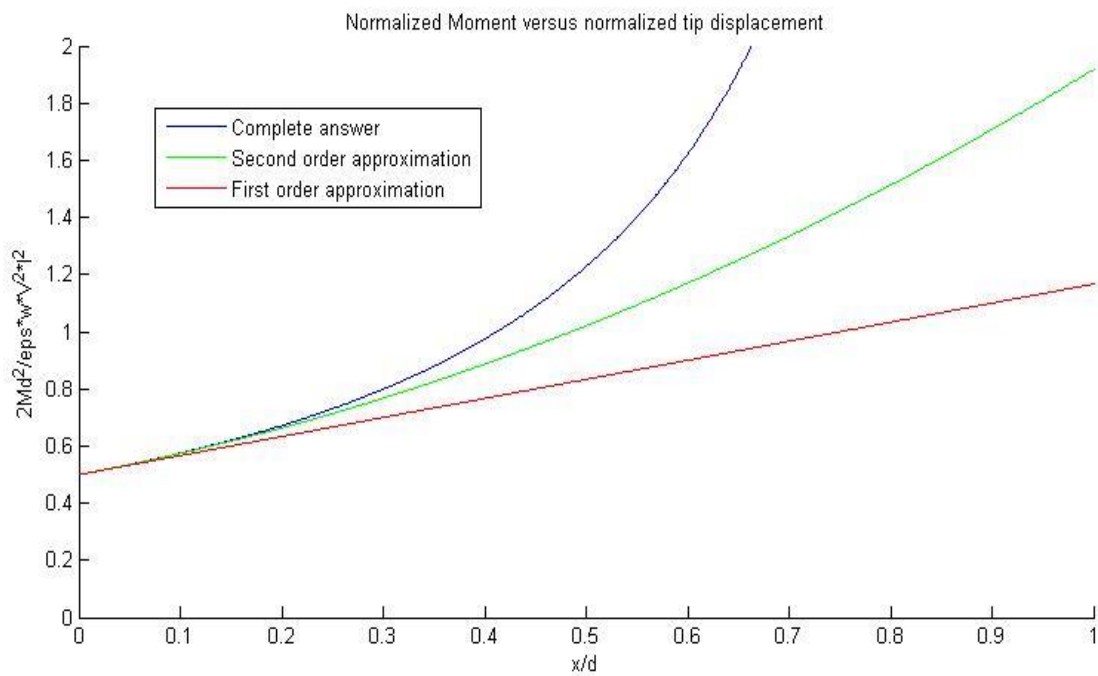

Fig 3.8: Zoomed view of dimensionless moment versus dimensionless electrode tip displacement.

$$K_{\theta,Elec} = K_{rim,Elec} \times l^2 = -\frac{\varepsilon w l^3 V^2}{3d^3} \tag{3.20}$$

Pull-In Analytical Calculations

In order to find out how much the tip of the actuator will displace when a voltage difference is applied, the nonlinear curve of Figure 3.7 should be intersected with the linear restraining moment curve of the cantilever that passes through the origin. In low voltages there are two intersection points. The left one is the stable equilibrium point and the right one would be unstable. If the voltage is increased the nonlinear moment curve of the capacitor moves up while the linear restraining moment curve is fixed. In this way, the two equilibrium points will converge until the voltage reaches the pull-in voltage, in which the nonlinear curve will touch the linear restraining moment curve at only one point. At this condition, both stable and nonstable equilibrium points will be coincident. If the voltage is increased higher than the pull-in voltage the two curves will not have any intersections and there would be no equilibrium points. In order to calculate the pull-in voltage, the fact that at this point the value and the derivative value of the two curves are equal can be used, which is shown in equations 3.21 and 3.22, respectively. If these two equations are solved simultaneously the tip displacement at pull-in voltage can be found and then one of the equations, 3.21 or 3.22, can be used to find the pull-in voltage.

$$\frac{\varepsilon w l^2 V^2}{2d^2}\left[\frac{1}{\alpha^2}\ln(1-\alpha) + \frac{1}{\alpha(1-\alpha)}\right] = k_\theta \theta = k_\theta \frac{x}{l} = k_\theta \frac{d}{l}\alpha \tag{3.21}$$

$$\frac{\varepsilon w l^2 V^2}{2d^2}\left[\frac{-2}{\alpha^3}\ln(1-\alpha) - \frac{1}{\alpha^2(1-\alpha)} - \frac{1}{\alpha^2} + \frac{1}{(1-\alpha)^2}\right] = k_\theta \frac{d}{l} \tag{3.22}$$

To solve these two equations simultaneously, the lower equation can be multiplied by α and then the left parts can be equated to reach:

$$\frac{1}{\alpha^2}\ln(1-\alpha)+\frac{1}{\alpha(1-\alpha)}=\frac{-2}{\alpha^2}\ln(1-\alpha)-\frac{1}{\alpha(1-\alpha)}-\frac{1}{\alpha}+\frac{\alpha}{(1-\alpha)^2} \tag{3.23}$$

$$\frac{3}{\alpha^2}\ln(1-\alpha)+\frac{2}{\alpha(1-\alpha)}+\frac{1}{\alpha}=\frac{\alpha}{(1-\alpha)^2} \tag{3.24}$$

If equation 3.24 is solved numerically the pull-in displacement would be:

$$\alpha_{pull-in}=0.4404 \tag{3.25}$$

Now, if this number is plugged into equation 3.21 or 3.22 the $V_{pull-in}$ would be:

$$V_{pull-in}=\sqrt{\frac{(0.82745)K_\theta d^3}{\varepsilon w l^3}} \tag{3.26}$$

Equation 3.26 can be used to calculate the pull-in voltage for a square cross section resonator with 530 μm height, 140 μm width, which is connected to the substrate by a cantilever with the length of 100 μm and thickness of 1 μm. The electrode gap is assumed to be 10 μm and the cantilever is made out of nickel. Using equation 3.2, K_θ would be:

$$K_\theta = \frac{EI}{L} = \frac{Ebh^3}{12L} = \frac{(219 \times 10^9) \times 140 \times 10^{-18}}{12 \times 100} = 2.555 \times 10^{-8} \quad N.m \qquad (3.27)$$

Now the pull-in voltage can be calculated using equation 3.26 to be:

$$V_{pull-in} = \sqrt{\frac{(0.82745)(2.555 \times 10^{-8}) \times 10^3}{(8.85 \times 10^{-12})(140 \times 10^{-6})(530)^3}} = 10.71\ V \qquad (3.28)$$

Pull-In COMSOL Simulation

For the same resonator described in the last section a COMSOL simulation is done. The pull-in voltage was about 11 volts and the electrode tip displacement at pull-in is about 4.9 μm, which is about half the electrode gap as shown in Figure 3.9. The calculated pull-in voltage and displacement in the last section are 10.71 V and 4.4 μm,

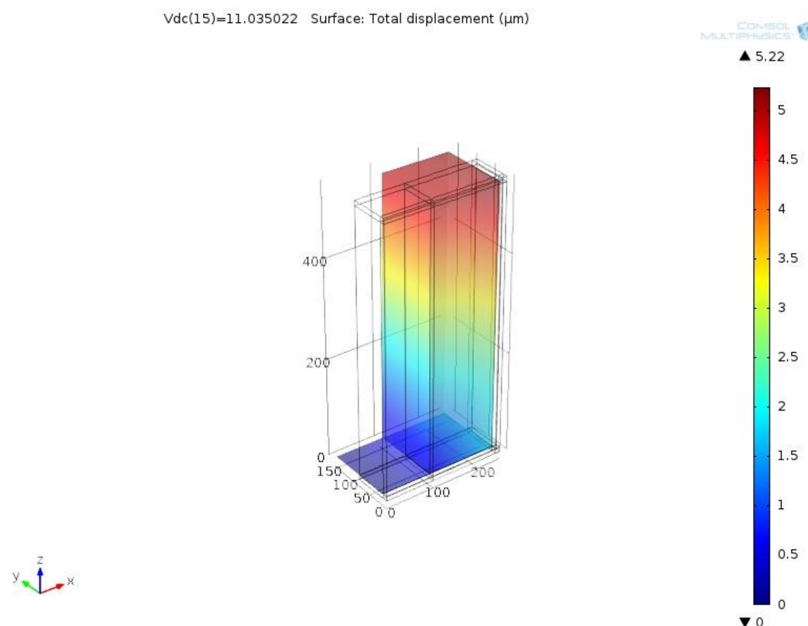

Fig 3.9: Pull-in COMSOL simulation of the microactuator.

that matches the simulation very well. In Figures 3.10 and 3.11, the capacitance change and tip displacement versus voltage plots are shown.

Sense and Drive Frequency Versus Misalignment

In this part the effect of misalignment on the sense and drive frequency mismatch is modeled. Appendix A should be studied at first, to see how the proposed fabrication technique can reduce the effect of misalignments. The general dimensions of the model that is used are shown in Table 3.1. Figures 3.12 through 3.15 show the meshed pattern used in this simulation. After modal analysis two distinct mode shapes for the sense and drive motions are shown, in Figures 3.16 and 3.17. The drive and sense frequencies are calculated to be 23460 Hz and 23476 Hz, respectively, which yields 16 Hz frequency mismatch due to unsymmetrical free meshing of the system. Now, if 20 μm misalignment is introduced between the top and bottom mask some of the resonators move slightly and

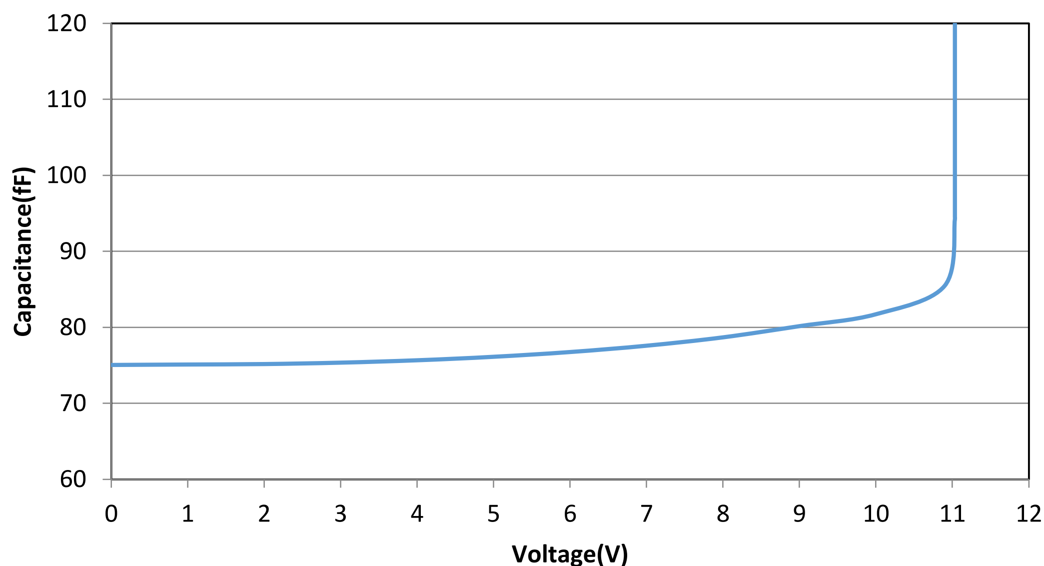

Fig 3.10: Capacitance versus voltage difference.

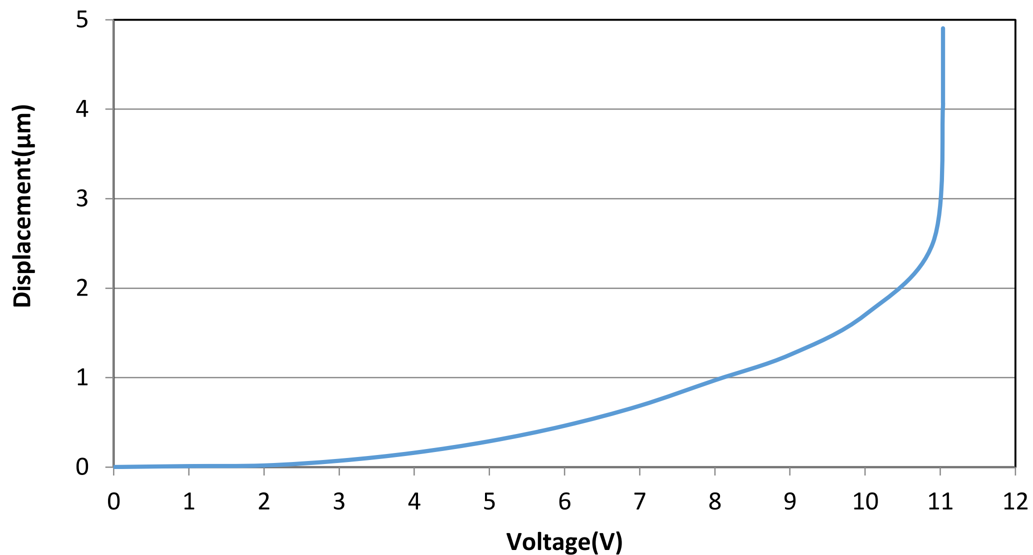

Fig 3.11: Electrode tip displacement versus voltage difference.

Table 3.1: Model dimensions.

Number of resonators	32
Nickel cantilever thickness	5 µm
Nickel cantilever width	140 µm
Nickel cantilever length	100 µm
Square silicon proofmass width	140 µm
Silicon proofmass height	530 µm
Nickel coupler gap	5 µm
Coupler round connector diameter	20 µm
Nickel coupler diameter	2 mm
Nickel coupler width	30 µm
Nickel coupler thickness	5 µm

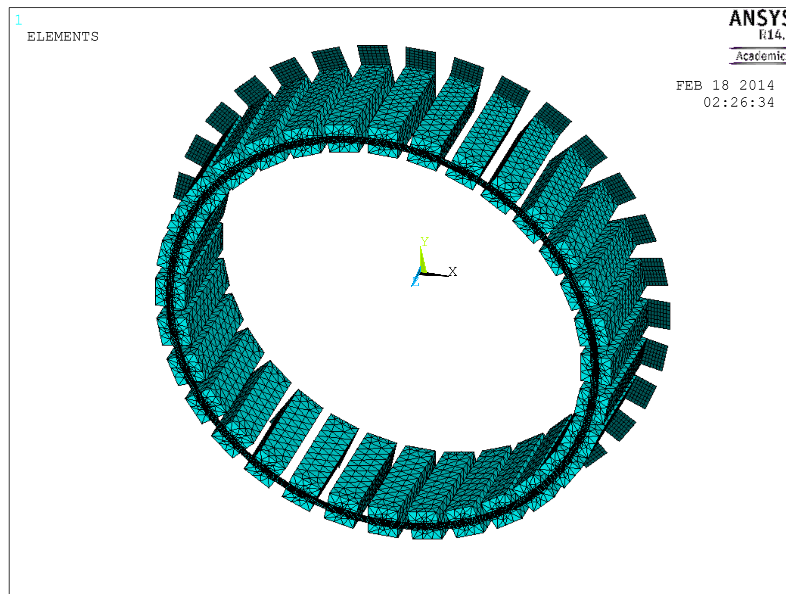

Fig 3.12: Overall structure.

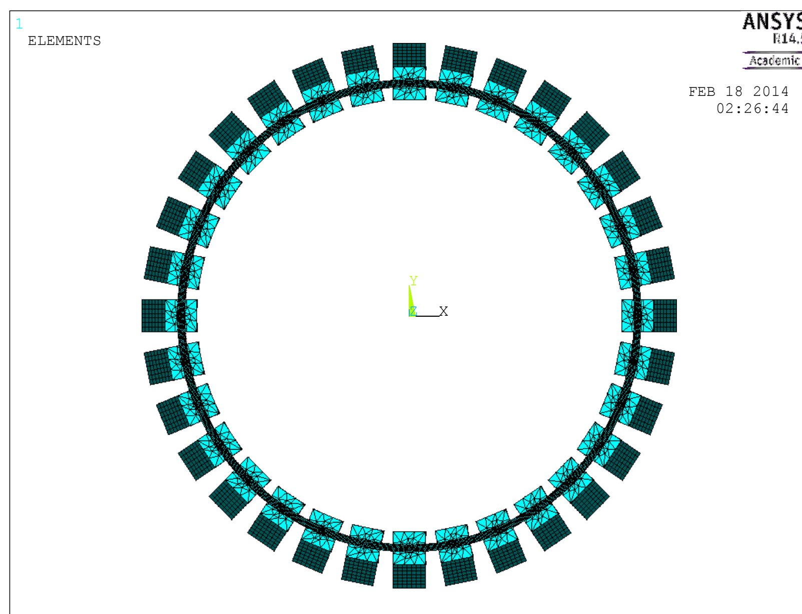

Fig 3.13: Overall structure from the top view.

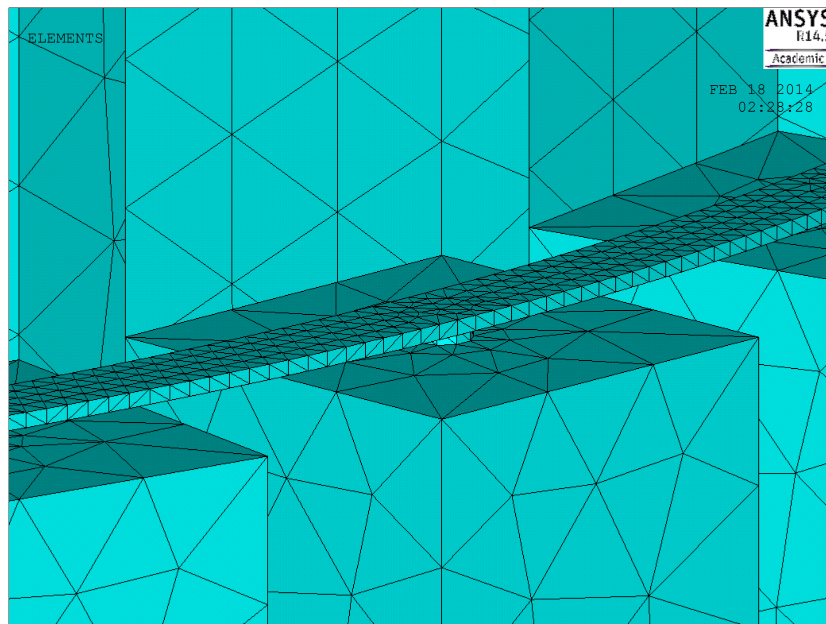

Fig 3.14: Nickel coupler and point contact.

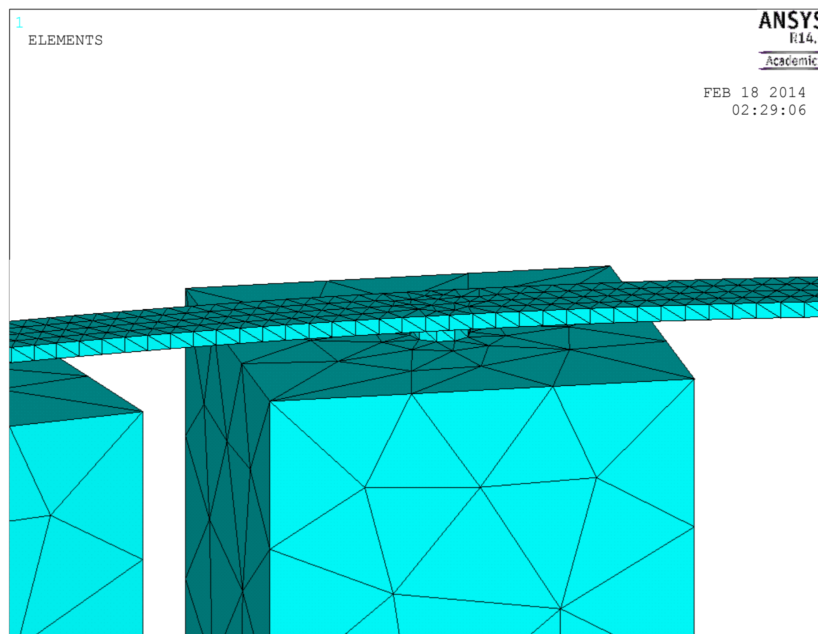

Fig 3.15: Nickel coupler and point contact from another view.

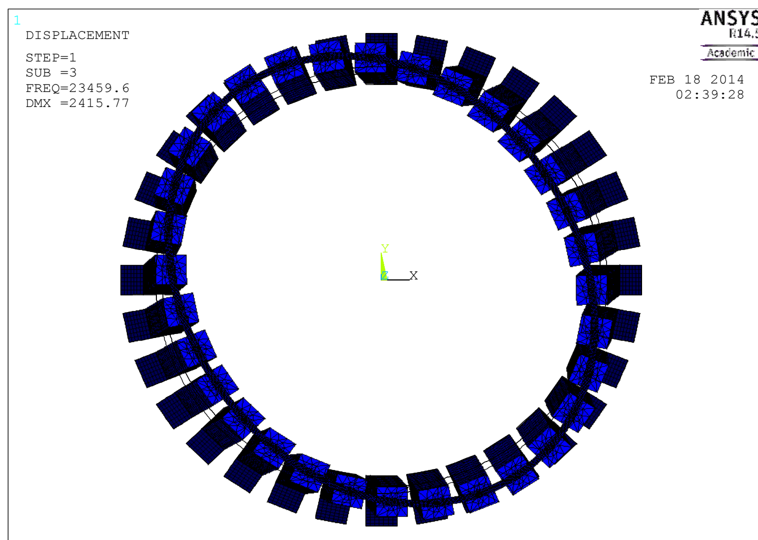

Fig 3.16: Drive frequency of 23459.6 Hz.

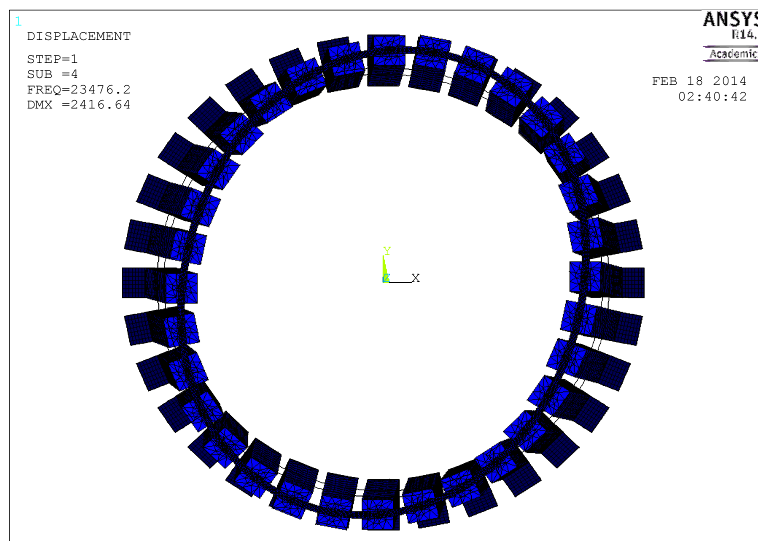

Fig 3.17: Sense frequency of 23476.22 Hz.

the two resulted mode shapes are shown in Figures 3.18 and 3.19. The new drive and sense frequencies are calculated to be 23345 Hz and 23435 Hz, respectively, which yields 90 Hz frequency mismatch due to unsymmetrical free meshing of the system and the misalignment. The misalignment effect would be less than 90 Hz, maybe about 70 Hz. This is about 0.3% of the natural frequency for 20 µm misalignment, which shows the system is almost insensitive to small misalignments. Control methods like using frequency tuning electrodes can be used to match the sense and drive exactly after fabrication. Frequency tuning is explained further in the acceleration canceling technique section of Chapter 4.

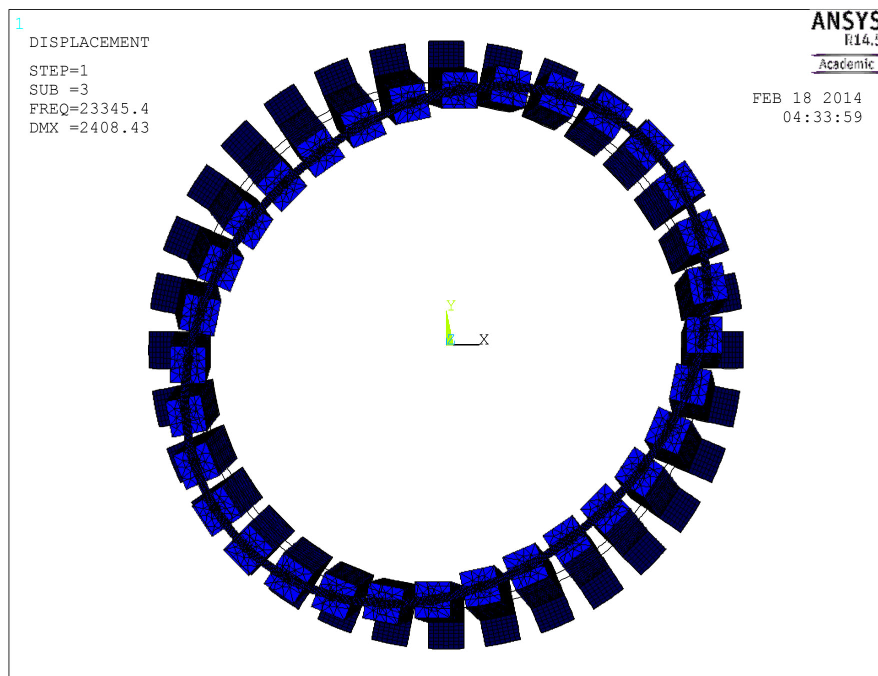

Fig 3.18: Drive frequency of 23345.4 Hz.

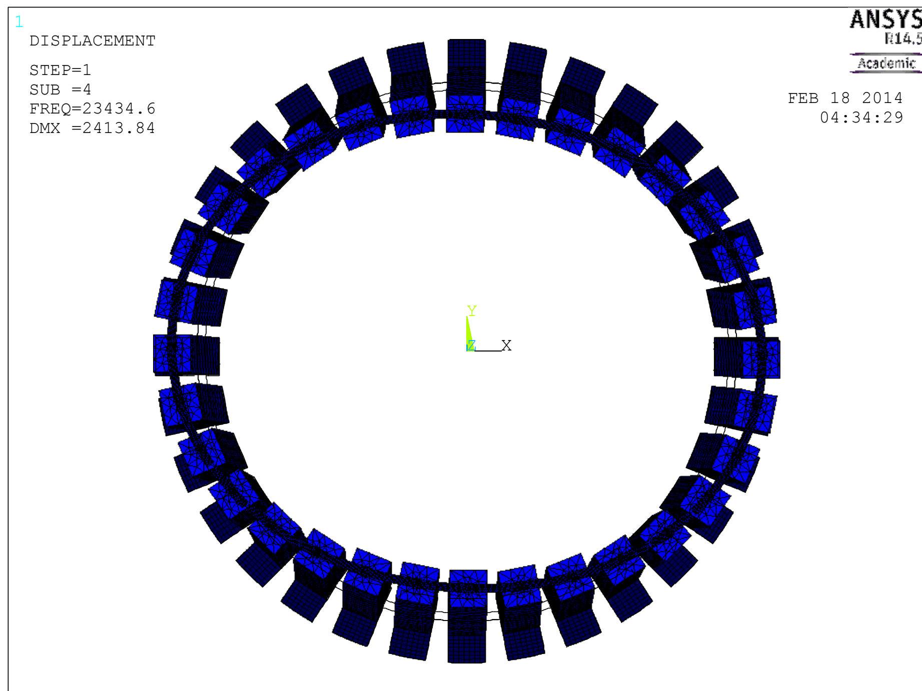

Fig 3.19: Sense frequency of 23434.6 Hz.

CHAPTER 4

DESIGN

In this section, a series of steps for finding the final dimensions of the device are discussed and a finite element simulation tool (ANSYS) is used to compute the sensitivity of the gyroscope, in each step. A combination of analytical formulas and FEM simulations are used to change the dimensions of the device to reach the maximum sensitivity possible. At last, a brief discussion about the readout circuit will be presented in order to cancel parasitic acceleration modes.

Natural Frequency

In order to have a better frequency mode matching of sense and drive motions, the model is remeshed in a more patterned way. Figures 4.1 and 4.2 show this new mesh pattern. The frequency mismatch between the sense and drive mode is not exactly zero because of the asymmetry of the freely meshed parts but it works fine to take our initial steps. The natural frequency of the system for each mode shape can be calculated from this formula derived from energy formulation in vibrational analysis:

$$f_0 = \frac{1}{2\pi}\sqrt{\frac{K_\theta + Cl^2\, K_{eff,coupler}}{I_\theta + El^2\, M_{eff,coupler}}} \tag{4.1}$$

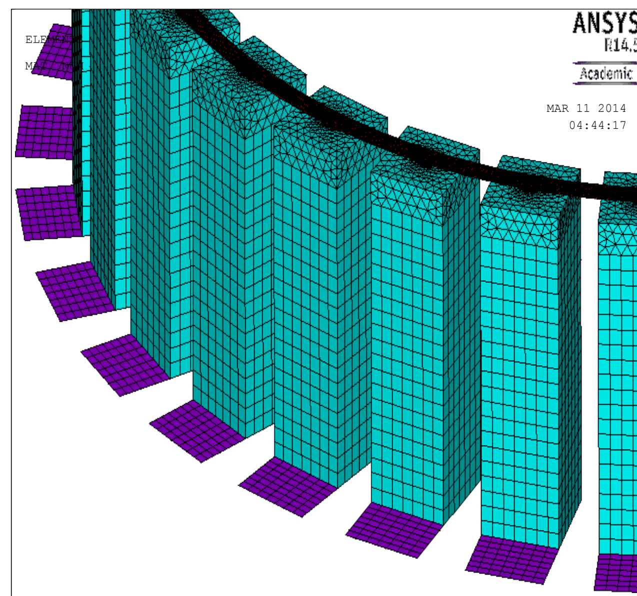

Fig 4.1: Initial meshed model used in our design process. There are some parts with patterned meshing and some parts with free meshing.

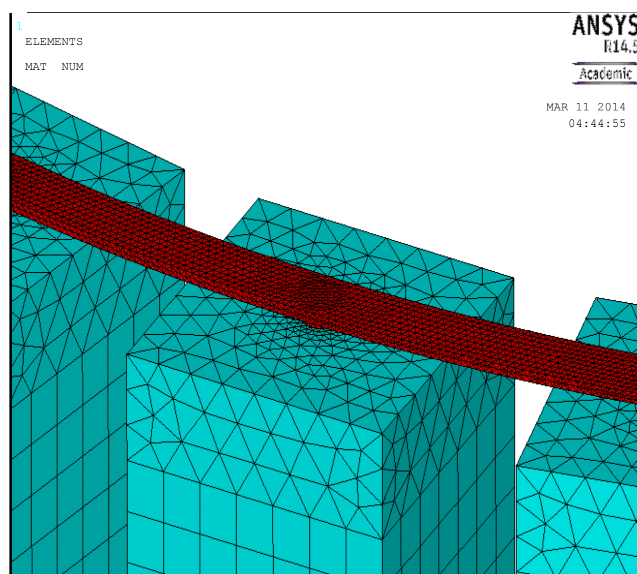

Fig 4.2: Zoomed view on the initial meshed model used in our design process.

where the effective rotational spring constant and mass inertia can be derived from formulas 4.2 and 4.3.

$$K_\theta = \sum_{i=1}^{32} A_i K_{\theta,bending} + B_i K_{\theta,torsion} \quad (4.2)$$

$$I_\theta = \sum_{i=1}^{32} D_i I_{\theta i} \quad (4.3)$$

where $I_{\theta i}$ is the mass moment of inertia of each resonator around the rotation axis, which may not be along the tangential and radial direction according to the mode shape because the tip of each resonator may have both radial and tangential velocity components. $K_{\theta,bending}$ and $K_{\theta,torsion}$ are the rotational spring constants in the bending and torsional movement of the cantilevers. A_i, B_i, C, D_i, E, $K_{eff,coupler}$, $M_{eff,coupler}$ and $I_{\theta i}$ are constants that vary for each mode shape and can be computed from relative maximum rotations and displacements in different parts of the system and l is the height of the resonators.

If only a ring resonator is analyzed, then a 4 node mode will have the lowest frequency, but if a very weak coupler system is used in this gyroscope, the constants mentioned above would be in such a way that the natural frequency of the four node mode comes after 6 node modes and 8 node modes.

Silicon Coupler - 5 µm Nickel Cantilever - Q = 200

For the first model the dimensions listed in Table 3.1 are used. The coupler is made out of silicon <111> with elastic modulus of 168.9 GPa [24] with 5 µm thickness, 30 µm width and 2mm diameter. Cantilevers are made out of nickel (205GPa) with 5 µm thickness, 100 µm length and 140 µm width. The quality factor is considered to be 200 for the first try in this model. If a 20 µm thick coupler is used, the sense and drive mode shapes will have the lowest frequencies among other mode shapes; however, if the coupler thickness is reduced to 5 µm the sense and drive mode shapes will not be the first mode shapes anymore and they will come after some parasitic mode shapes. The first six mode shapes are shown in Figures 4.3 to 4.8.

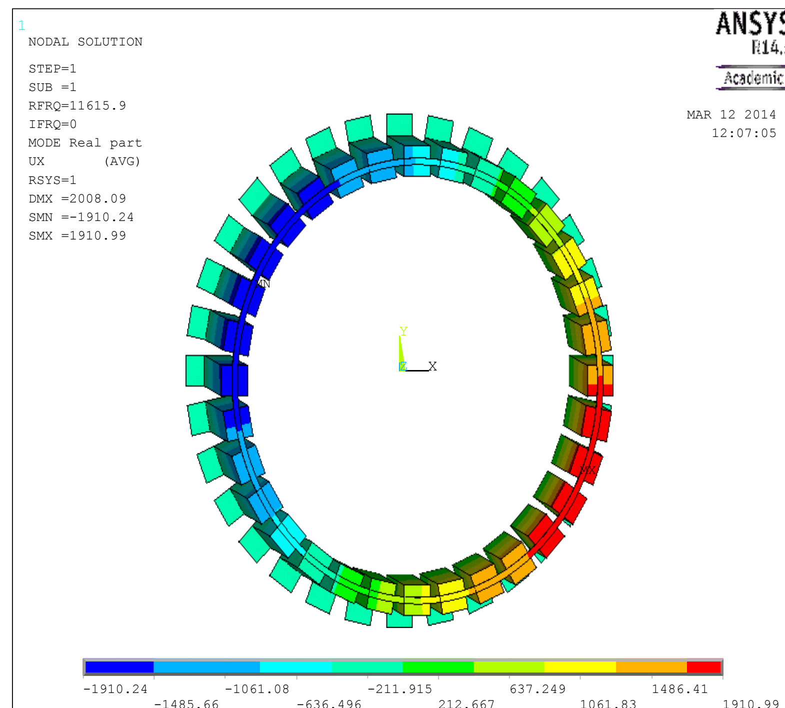

Fig 4.3: First parasitic mode shape, 11615.9 Hz.

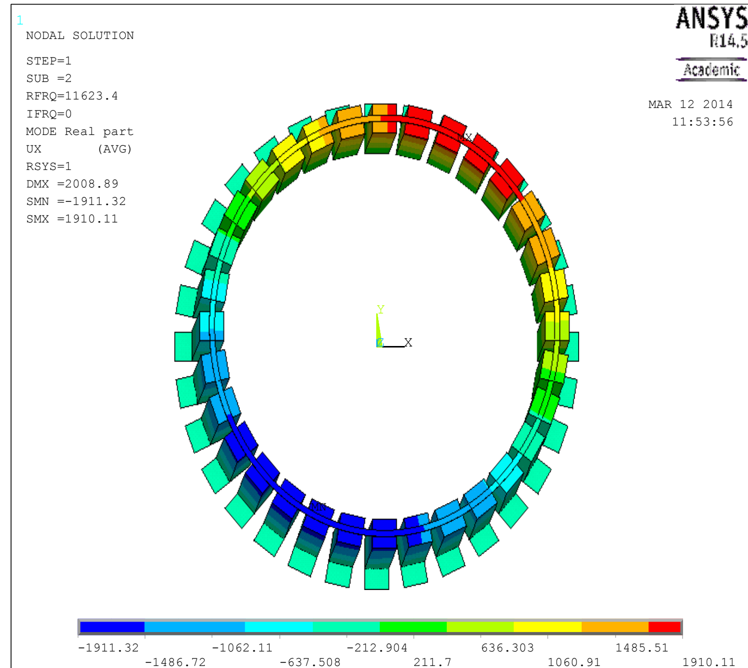

Fig 4.4: Second parasitic mode shape, 11623.4 Hz.

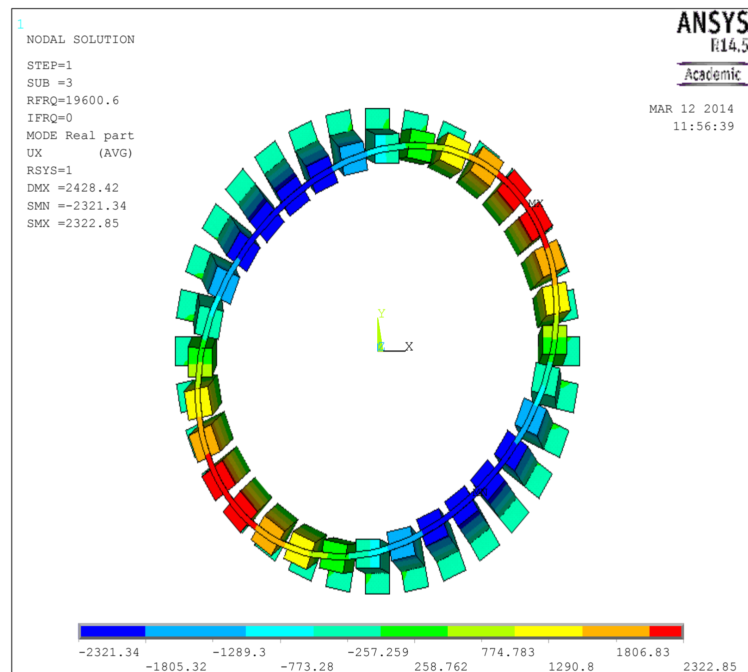

Fig 4.5: Drive mode shape, 19600.6 Hz.

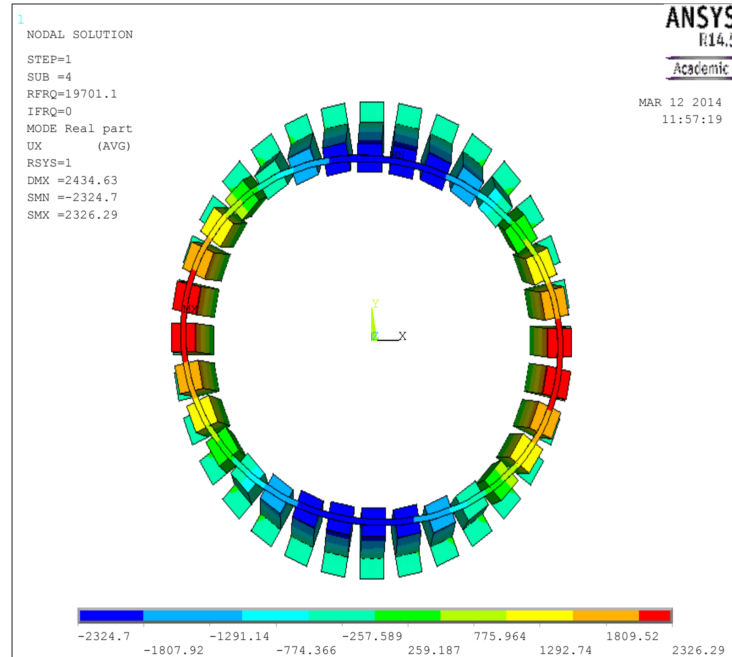

Fig 4.6: Sense mode shape, 19701.1 Hz.

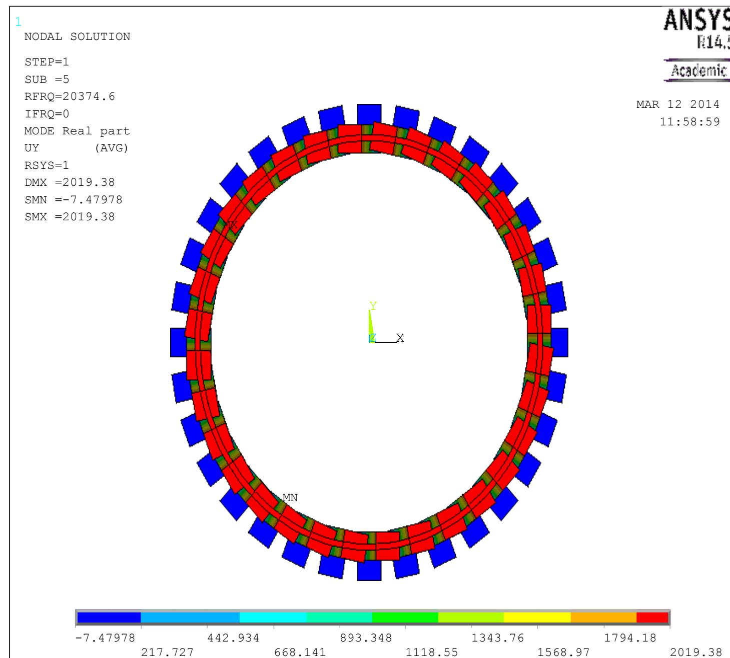

Fig 4.7: Fifth mode shape, 20374.6 Hz.

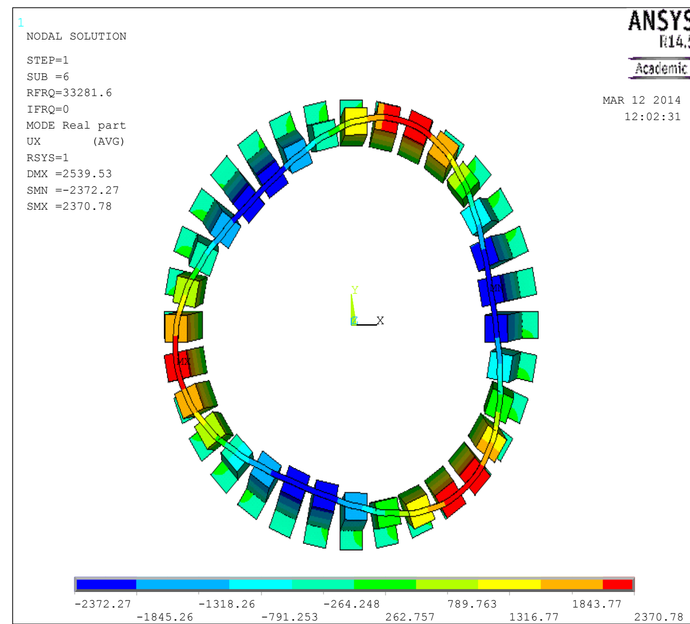

Fig 4.8: Sixth mode shape, 33281.6 Hz.

Excitation is done with two opposite 1 μN forces on the upper and lower resonators with assumed quality factor of 200 and excitation frequency of 19700 Hz. In Figures 4.9 and 4.10, it can be seen that the vibration pattern will rotate slightly in the presence of external rotation. The simulation results for the first try are shown in Table 4.1. Displacement in the sensing direction and pattern rotation versus external rotation is shown in Figure 4.11.

Formula 3.17 is restated here for better referencing:

$$F_{Top} = \frac{\varepsilon w l V^2}{2d^2}\left[\frac{1}{2} + \frac{2\alpha}{3} + \frac{3\alpha^2}{4}\right] \tag{4.4}$$

From formula 4.4 the equivalent electrostatic force on top of the microactuator can be calculated. In practice a constant voltage is not applied to the electrode and the

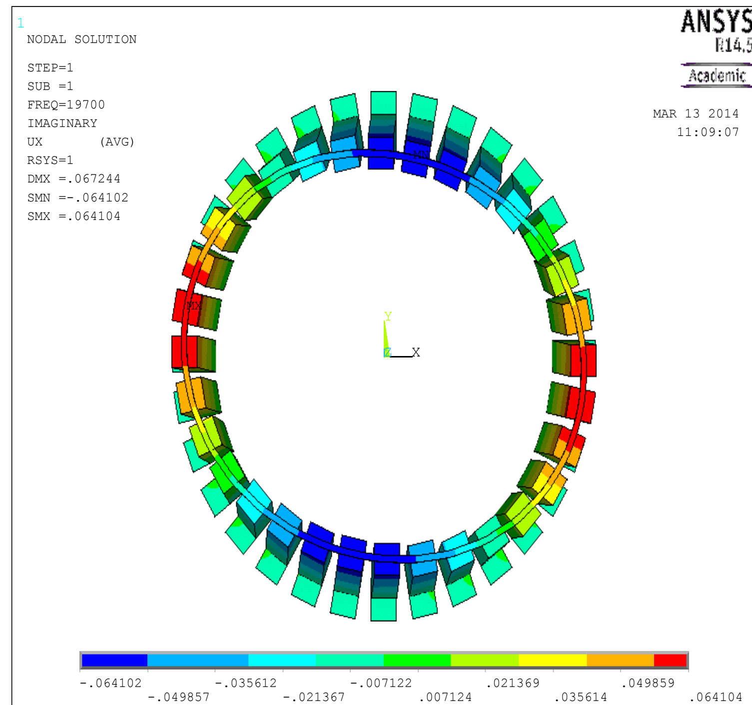

Fig 4.9: Rotation harmonic response for 650 deg/sec.

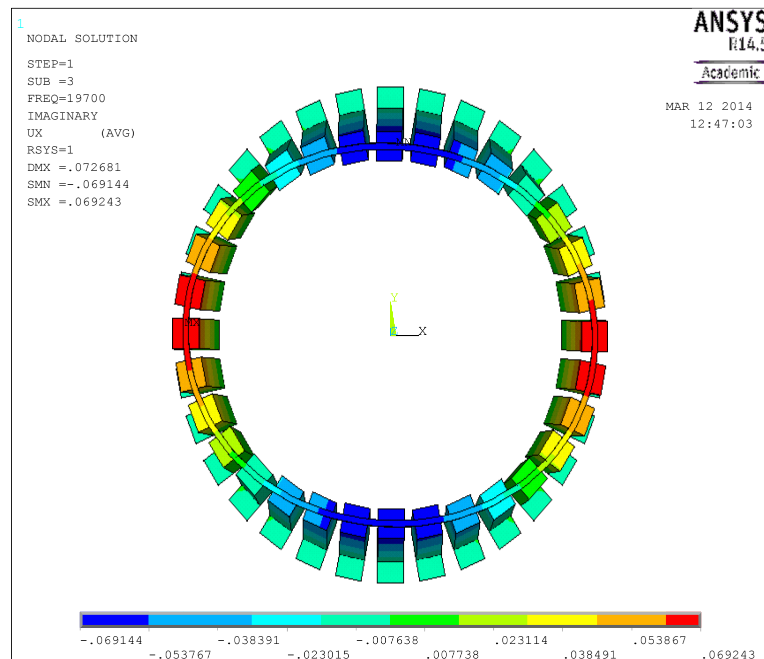

Fig 4.10: No rotation harmonic response.

Table 4.1: Simulation results for different rotation speeds for try number 1.

Rotational velocity (deg/s)	Pattern rotation (deg)	45 degree node radial displacement (nm)	45 degree node tangential displacement (nm)	Maximum displacement (nm)
0	0	7.52	35.18	72.7
50	0.68	8.57	34.33	71
150	2.07	10.98	34.15	71
250	3.89	13.32	33.79	70
350	5.60	15.57	32.26	70
450	6.99	17.73	32.57	69
550	8.05	19.79	31.70	68
650	8.82	21.72	30.69	67

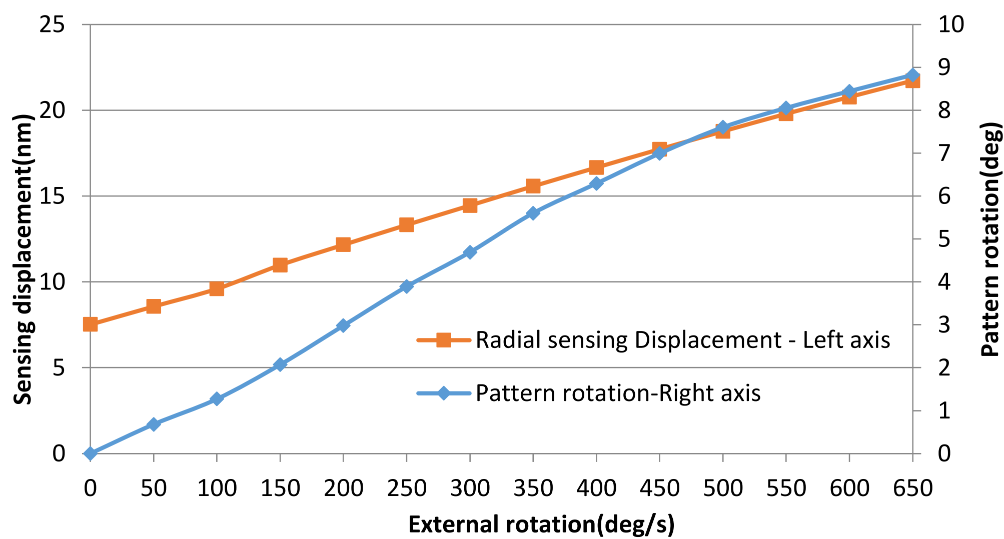

Fig 4.11: Radial sensing displacement and pattern rotation for up to 650 deg/s external rotation.

voltage difference would be of the following form:

$$V = V_{ac}Cos(wt) + V_{dc} \tag{4.5}$$

If equation 4.5 is substituted into equation 4.4, after expansion lots of different terms will be generated. If V_{dc} is assumed to be about ten times bigger than V_{ac}, the prominent parts of the force for small amplitude vibrations would be:

$$F_{Top} = \frac{\varepsilon wl{V_{dc}}^2}{4d^2} + \frac{\varepsilon wlV_{ac}V_{dc}}{2d^2}Cos(wt) \tag{4.6}$$

The first term will cause a static deformation while the second term is the resonating force which causes the actual vibration amplitude which is used later to calculate the driving force. The negative spring constant on top of the actuator will be:

$$K_{rim,Elec} = -\frac{\varepsilon wl{V_{dc}}^2}{3d^3} \tag{4.7}$$

From equations 3.4 and 3.15, the capacitance C_x can be written in terms of unitless displacement α:

$$C_x = -\frac{\varepsilon wl}{d}\frac{\ln(1-\alpha)}{\alpha} = \frac{\varepsilon wl}{d}\left(1 + \frac{\alpha}{2} + \frac{\alpha^2}{3} + \frac{\alpha^3}{4} + \frac{\alpha^4}{5} + \cdots\right) \tag{4.8}$$

So, ΔC as a function of tip displacement would be:

(4.9)

$$\Delta C = C_x - C_0 = \frac{\varepsilon w l}{d^2}\left[\frac{x}{2} + \frac{x^2}{3d} + \frac{x^3}{4d^2} + \frac{x^4}{5d^3} + \cdots\right]$$

In small amplitude vibrations only the first term can be used. In the previous simulation 1 μN force was assumed. If $V_{dc} = 100\ V$ and $V_{ac} = 5\ V$, the needed gap for the capacitor to generate that much force will be:

$$F = \frac{\epsilon w l V_{DC} V_{AC}}{2d^2} = \frac{8.85 \times 10^{-12} \times 140 \times 530 \times 100 \times 5}{2 \times d^2} = 10^{-6}\ N \Rightarrow$$
$$d = 12.81\ \mu m \qquad (4.10)$$

So, if the gap is 128.1 μm instead of 12.81 μm, the force would be 100 times less than 1μN. The quality factor is considered to be 200 in the simulation, so with 128.1 μm gap the quality factor of 2000 is needed so that the displacement values match the simulation results, because output displacements are proportional to Q^2, according to equation 2.4. This is true, if the vibration amplitude does not go too high and the voltages are considered to be fixed.

$$\text{Pattern rotation sensitivity} = \frac{8.82\ deg}{650\ deg/s} = 1.357 \times 10^{-2}\ \frac{deg}{deg/s} \qquad (4.11)$$

So, 100 deg/s will cause 1.357 degrees pattern rotation.

$$\text{Radial displacement sensitivity} = \frac{(21.7-7.52)\ nm}{650\ deg/s} = 2.182 \times 10^{-2}\ \frac{nm}{deg/s} \qquad (4.12)$$

So, 100 deg/s will cause 2.182 nm change in amplitude for a vibration with 7.52 nm initial amplitude without any rotation in the sensing electrode. The zero rate output will be:

$$\text{Zero rate output: } \frac{7.52\ nm}{2.182\times10^{-2}\frac{nm}{deg/s}} = 344.64\ \ deg/s \tag{4.13}$$

This means even in the stationary position the sensor will read almost one rotation per second for the sensor. Zero rate output, which is sometimes called quadrature error, is considered one of the most common weak points of MEMS gyroscopes. In simulations this is caused because of meshing asymmetries and in real gyroscopes it is caused by fabrication imperfections and anisoelasticities.

From [25], it is known that less than aF capacitance changes can be detected using delta sigma method. If it is assumed that 1 aF capacitance change corresponds to 1 mV of output signal, then sensitivities of higher than 1 $\frac{mV}{aF}$ can be achieved.

$$\Delta c = \frac{\varepsilon A}{2d^2}.Sensing\ resonator\ radial\ displacement =$$

$$= \frac{8.85\times10^{-12}\times530\times140\times(21.72-7.52)\times10^{-9}}{2\times10^{2}}$$

$$= 46.62\ aF \tag{4.14}$$

$$\frac{\Delta c}{w} = \frac{46.62\ af}{650\ deg/s} = 0.0717\frac{af}{deg/s} \tag{4.15}$$

$$\text{The minimum detectable signal} = \frac{1}{0.0717} = 13.94 \text{ deg/s} \tag{4.16}$$

$$\text{Total sensitivity} = 0.0717 \frac{mV}{deg/s} \tag{4.17}$$

It can be seen that there is a large difference between the sensitivity of this design and previously designed gyroscopes with sensitivity of 132 $\frac{\text{mV}}{\text{deg/s}}$ [5]. For a simple proofmass gyro with driving direction along the x axis and sensing direction along the y axis, it can be written that:

$$Sense\ amplitude = Q_s \frac{F_c}{K_s} = 2m\Omega_z w_d \frac{Q_s Q_d}{K_s K_d} F_d \Rightarrow \frac{Sense\ amplitude}{\Omega_z}$$

$$= 2\sqrt{m} \frac{Q_s Q_d}{K_s \sqrt{K_d}} F_d \tag{4.18}$$

The equation above is exact and is in the form of equality relation. For hemispherical gyroscopes a similar relation holds, but a coefficient should be added to the formula that should be calculated by simulations or more sophisticated analytical approaches. For simplicity a proportionality relation is used here instead of equality.

$$\frac{Sense\ amplitude}{\Omega_z} \propto \sqrt{m_{eff}} \frac{Q^2}{{K_{eff}}^{1.5}} F_d \propto \sqrt{m_{eff}} \frac{Q^2}{{K_{eff}}^{1.5}} \frac{\epsilon w l V_{AC} V_{DC}}{2d^2} \tag{4.19}$$

m_{eff} and K_{eff} can be calculated as follows:

$$\mathrm{m_{eff}} = \mathrm{m_{eff,coupler}} + \sum_{i=1}^{32} \mathrm{A_i} \frac{\mathrm{I_i}}{\mathrm{l}^2} \tag{4.20}$$

$$\mathrm{K_{eff}} = \mathrm{K_{eff,coupler}} + \sum_{i=1}^{32} \mathrm{B_i} \frac{\mathrm{K_{\theta,bending}}}{\mathrm{l}^2} + \sum_{i=1}^{32} \mathrm{C_i} \frac{\mathrm{K_{\theta,tortion}}}{\mathrm{l}^2} \tag{4.21}$$

Unknown coefficients can be derived from relative maximum displacements and rotations for each mode shape. The capacitance change per external rotation can be derived using equations 4.9 and 4.19:

$$\frac{\Delta c}{\Omega_z} \propto \frac{\varepsilon A}{2d^2} \sqrt{m_{eff}} \frac{Q^2}{{K_{eff}}^{1.5}} \frac{\epsilon w l V_{AC} V_{DC}}{2d^2} \tag{4.22}$$

According to equation 4.22, if the mass is kept fixed three other parameters are available to play with in order to increase the sensitivity, $\mathrm{K_{eff}}$, quality factor and gap distance. The output voltage to change of capacitance ratio, which was assumed 1 mV/aF last time, can be improved as the forth parameter. If it is assumed that the quality factor is going to remain very bad (as 200) and the gap distance is decreased to 1.35 μm, the highest sensitivity which is reported will be reached without changing other parameters but it is almost impossible to fabricate a 1.35 micron trench in a 530 wafer. According to Appendix A, two overhang lengths and at least 2 μm gap are needed and if 4 μm misalignment is assumed in the best case scenario at least 10 μm is needed for the gap so that it can be fabricated. Remaining options would be playing with the $\mathrm{K_{eff}}$ or the readout circuit. For the next try the $\mathrm{K_{eff}}$ is reduced as much as possible, by using SU8 polymer

couplers and 1 μm thick nickel cantilevers. The force is also corrected from 1 μN to the more exact value of 1.642 μN for 10 μm gap size. V_{dc} = 100 V and V_{ac} = 5 V are kept as previous values.

Polymer Coupler - 1 μm Nickel Cantilever - Q = 200

The natural frequencies of the system reduce because the effective spring constant of the system is decreased. After decreasing the compliance of the system, the sequence of the mode shapes will remain the same except parasitic mode shape 5, which moves to a frequency lower than drive and sense mode shapes and becomes number 3. Figures 4.12 to 4.17 show the first six mode shapes.

It can be seen that the drive frequency is about 3125.97 Hz and sense frequency is 3139.74 Hz, which do not match exactly with the difference of 13.77 Hz. The polymer coupler is considered to be made out of SU8 and the dimensions are the same as before. The harmonic response for no rotation and 500 deg/s external rotation are shown in Figures 4.18 and 4.19. It can be seen that the vibration pattern rotates in the presence of external rotation. The resultant vibrational pattern is constructive addition of two vibrational modes in the drive and sense mode, which are 45 degrees misaligned. As the external rotation increases the amplitude of sense vibration increases and will shift the resultant vibrational pattern from the drive direction towards the sense direction. However, the pattern rotation cannot exceed 45 degrees no matter how much the external rotation is increased. Table 4.2 shows the simulation results for the second try.

It can be seen that tangential displacement of the sense resonator is almost half of the maximum displacement and is about 2.21 μm. This will cause unwanted zero rate

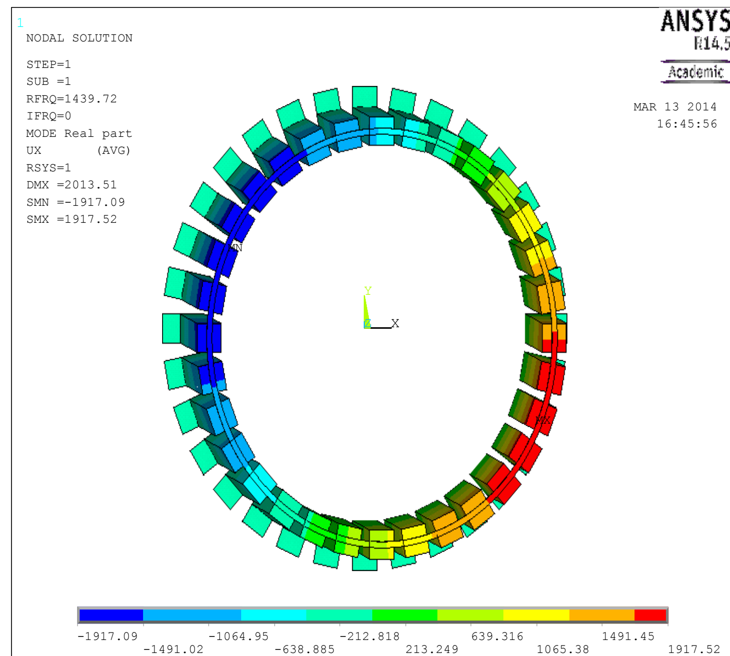

Fig 4.12: First parasitic mode shape, 1439.72 Hz.

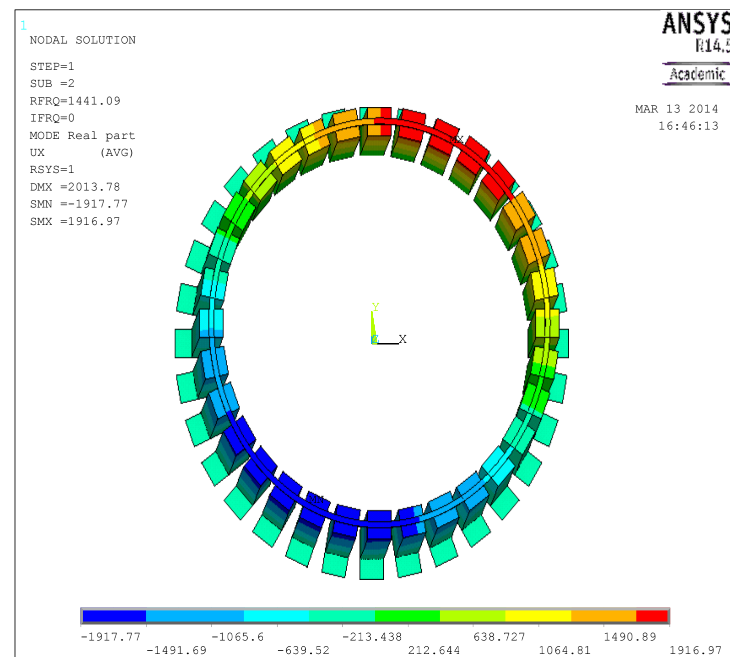

Fig 4.13: Second parasitic mode shape, 1441.09 Hz.

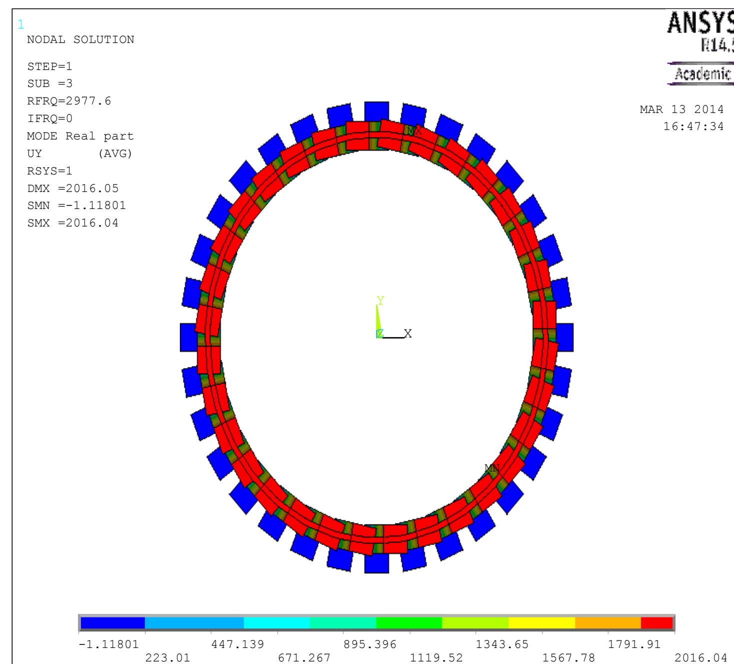

Fig 4.14: Third parasitic mode shape, 2977.6 Hz.

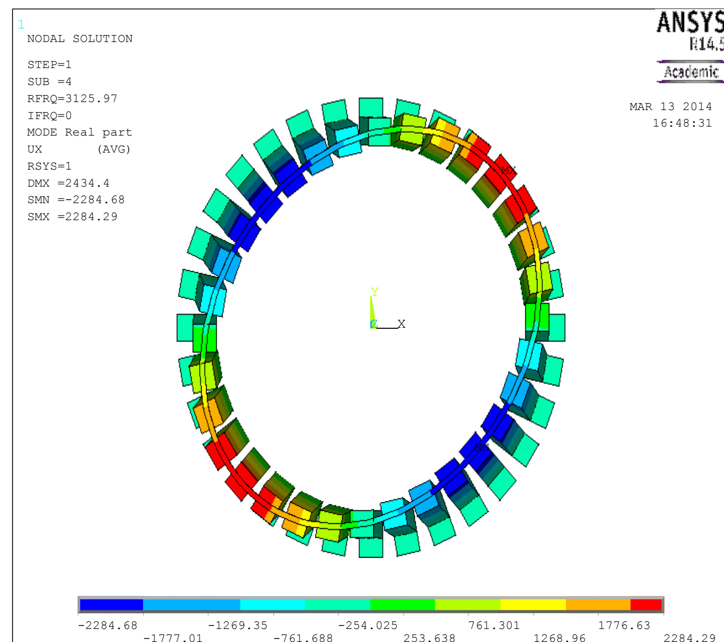

Fig 4.15: Drive mode shape, 3125.97 Hz.

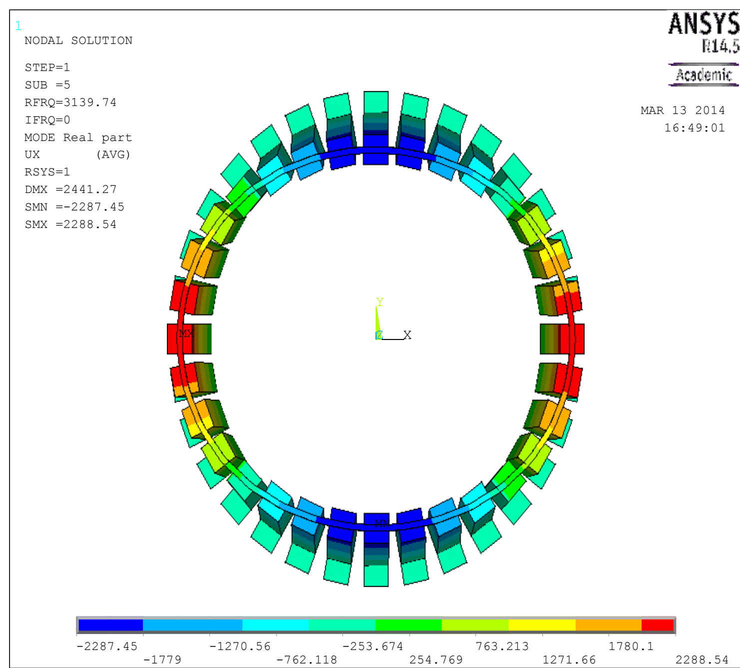

Fig 4.16: Sense mode shape, 3139.74 Hz.

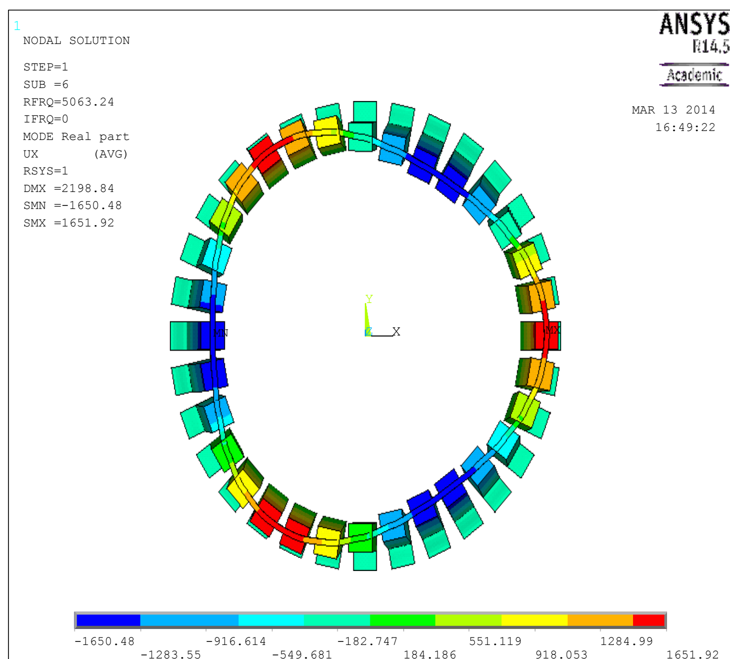

Fig 4.17: Sixth mode shape, 6063.24 Hz.

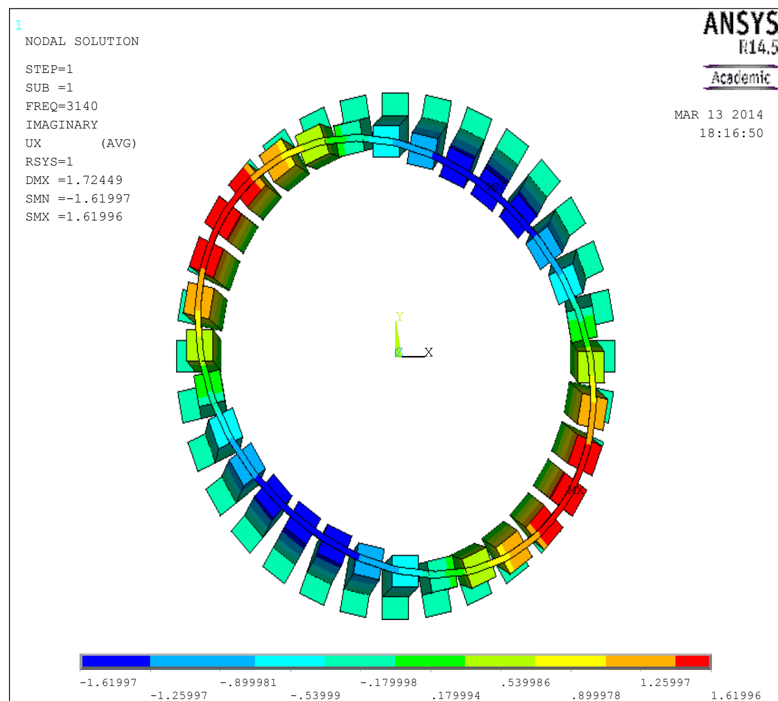

Fig 4.18: External rotation harmonic response for 500 deg/s.

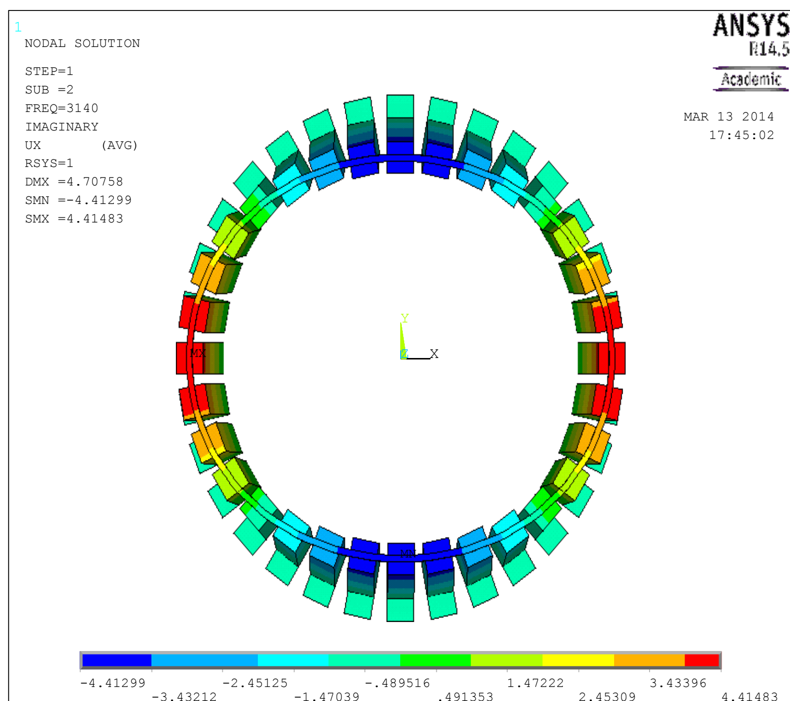

Fig 4.19: No external rotation harmonic response.

Table 4.2: Simulation results for different rotation speeds for try number 2.

Rotational velocity (deg/s)	Pattern rotation (deg)	45 degree node radial displacement (µm)	45 degree node tangential displacement (µm)	Maximum displacement (µm)
0	0	0.056	2.21	4.71
500	37.95	1.486	0.32	2.71

output and in order to cancel it, it is needed to fabricate the fixed electrodes in front of the sense resonators, slightly bigger from the sides.

$$\text{Pattern rotation sensitivity} = \frac{37.95\ \text{deg}}{500\ \text{deg/s}} = 75.9 \times 10^{-3}\,\frac{\text{deg}}{\text{deg/s}} \tag{4.23}$$

So, 100 deg/s will cause 7.59 deg pattern rotation.

$$\text{Radial displacement sensitivity} = \frac{(1.486 - 0.056)\,\mu\text{m}}{500\ \text{deg/s}} = 2.86\,\frac{\text{nm}}{\text{deg/s}} \tag{4.24}$$

So, 100 deg/s will cause 286 nm change in amplitude for a vibration with 56 nm amplitude without any rotation in the sensing electrode.

$$\Delta c = \frac{\varepsilon A}{2d^2}.\text{Sensing resonator radial displacement}$$

$$= \frac{8.85 \times 10^{-12} \times 530 \times 140 \times (1.486\ - 0.056) \times 10^{-6}}{2 \times 10^{2}}$$

$$= 4695.2\ af \qquad (4.25)$$

$$\frac{\Delta c}{w} = \frac{4695.2\ \mathrm{af}}{500\ \mathrm{deg/s}} = 9.39\ \frac{\mathrm{af}}{\mathrm{deg/s}} \qquad (4.26)$$

The minimum detectable signal = 0.1065 deg/s (4.27)

Total sensitivity will also be $9.39\frac{\mathrm{mV}}{\mathrm{deg/s}}$ if it is assumed 1 aF capacitance change corresponds to 1 mV output signal. It can be seen that 132 $\frac{\mathrm{mV}}{\mathrm{deg/s}}$ is still not reached and the sensitivity should still be increased 14 times. By using polymer couplers and 1 µm cantilevers the sensitivity is increased 131.12 times. Half a µm nickel cantilevers can be used to increase sensitivity, or 1 µm thick silicon cantilevers can be used which have lower elastic modulus than nickel and maybe a higher quality factor. In this way, SOI wafers can be used which also increases the quality factor because of material mismatch. A silicon coupler with a 1 µm thickness can be used instead of a polymer coupler with 5 µm thickness. In this way, the quality factor and spring constant will increase but it is not known if it would have a positive effect on sensitivity or not because they have opposite effects. In the readout circuit section in this chapter it will be shown that if a Wheatstone bridge is used the gap distance only affects the driving voltages and not the sensitivity.

The device which is being compared to our device has a ring oscillator diameter of 2.7 mm. Our device has a 2 mm diameter coupler. If the diameter of the coupler is

increased to 3 mm diameters it will increase the sensitivity since larger masses can be used and the effective spring constant will be reduced. This reduces the frequency and increases the sensitivity. Another option is using multiple adjacent resonators as drive electrodes to decrease voltage levels. For example, three resonators next to each other can be used for driving the gyroscope. The circuit can be improved to increase voltage to capacitance change ratio from 1 mV/aF to higher levels which will affect the sensitivity directly. The thicker the wafer is, the higher sensitivity the device will have, so using a wafer which is thicker than 530 μm can increase the sensitivity. For the next try, the quality factor is increased 100 times to see how it affects the sensitivity.

Polymer Coupler - 1 μm Nickel Cantilever - Q = 20000

The formula 4.22 is useful until the maximum displacement does not go too high; for example, not more than half of the electrode gap, because if it goes higher than that then there is a chance that the resonators stick to the other electrode. In other words, equation 4.22 is a fixed voltage equation that shows how parameters will affect the sensitivity when excitation voltages are fixed. However, it is always necessary to check the drive amplitude so that it is not enough to cause stiction. A better design approach is assuming the drive amplitude as fixed, for example, about half the electrode gap, and see what excitation voltage is needed in each step. In this way, the output sensitivity will not be that much more sensitive to the parameters, as in the case of the fixed voltage formula.

$$U_d = Q\frac{F_d}{K_{eff}} = \frac{d}{2} \tag{4.28}$$

If equation 4.28 is plugged into equation 4.22 then:

$$\frac{\Delta c}{\Omega_z} \propto \left(\frac{\varepsilon A}{d} \frac{Q\sqrt{m_{eff}}}{\sqrt{K_{eff}}} = \frac{\varepsilon A}{d} \frac{Q}{w_n} = C_0 \frac{Q}{w_n}\right) \tag{4.29}$$

This is the constant amplitude sensitivity formula. The driving voltages can be derived from inserting the oscillating force of equation 4.6 into 4.28:

$$U_d = Q \frac{\frac{\varepsilon w l V_{ac} V_{dc}}{2d^2}}{K_{eff}} = \frac{d}{2} \Rightarrow V_{AC} V_{DC} = \frac{d^3 K_{eff}}{Q \epsilon w l} \tag{4.30}$$

In the constant drive amplitude method excitation voltages change and should be calculated in each step that the parameters are changed. Equation 4.30 is for drive amplitude equal to half of the electrode gap. If it is necessary to decrease the drive amplitude, the coefficient in equation 4.30 will change slightly. In our previous analysis with Q=200 and F_d=1.641 µN the drive amplitude was 4.71 µm, which is about half the electrode gap (10 µm). If the voltages are kept as fixed and the quality factor is increased further in the simulation, the drive amplitude will increase so much that stiction will occur. Therefore it is necessary to use the constant amplitude formula for predicting the next simulation results, so as the quality factor is increased to keep the drive amplitude constant the excitation voltages should be decreased. For example, if the quality factor is increased from 200 to 20000, V_{dc} can be decreased from 100 to 10 volts and V_{ac} from 5 volts to 0.5 volts. In this way, the drive amplitude remains constant but the driving force will reduce 100 times to 0.01641 µN. In the fixed drive amplitude formula

proportionality to the quality factor to the power of two is replaced with a linear relationship. So by increasing quality factor 100 times it is expected the sensitivity to increase 100 times as well. Simulation results are shown in Table 4.3.

$$\text{Pattern rotation sensitivity} = \frac{9.54\ \text{deg}}{25\ \text{deg/s}} = 0.3816\ \frac{\text{deg}}{\text{deg/s}} \quad (4.31)$$

So, 100 deg/s will cause 38.16 deg pattern rotation.

$$\text{Radial displacement sensitivity} = \frac{(0.293 - 0.127)\ \mu\text{m}}{25\ \text{deg/s}} = 6.64\ \frac{\text{nm}}{\text{deg/s}} \quad (4.32)$$

So, 100 deg/s will cause 664 nm change in amplitude for a vibration with 127 nm amplitude without any rotation in the sensing electrode.

$$\Delta c = \frac{\varepsilon A}{2d^2}.\text{Sensing resonator radial displacement}$$

$$= \frac{8.85 \times 10^{-12} \times 530 \times 140 \times (0.293 - 0.127) \times 10^{-6}}{2 \times 10^2}$$

Table 4.3: Simulation results for different rotation speeds for try number 3.

Rotational velocity (deg/s)	Pattern rotation (deg)	45 degree node radial displacement (μm)	45 degree node tangential displacement (μm)	Maximum displacement (μm)
0	0	0.127	2.210	4.710
25	9.54	0.293	0.493	1.092

$$= 545.0361\, af \tag{4.33}$$

$$\frac{\Delta c}{w} = \frac{545.0361 \text{ af}}{25 \text{ deg/s}} = 21.8 \frac{\text{af}}{\text{deg/s}} \tag{4.34}$$

$$\text{The minimum detectable signal} = 0.0458716 \text{ deg/s} \tag{4.35}$$

Total sensitivity will also be 21.8 $\frac{\text{mV}}{\text{deg/s}}$ if 1 aF capacitance change corresponds to 1 mV output signal. Although V_{dc}=10 V and V_{ac}=0.5 V are being used instead of V_{dc}=100 V and V_{ac}=5 V, it was expected that the sensitivity of the device would increase about 100 times because, as can be seen in the formula 4.29, sensitivity is proportional to the Q which was increased from 200 to 20000. However, the actual increase in the sensitivity is 2.32 times instead of 100. At first it may be suspected that the resonance peak is shifting because of rotation. When the response curve around the excitation frequency is compared to no rotation state it can be seen that the resonance peak is shifted from 3139.74 Hz to 3140 Hz in 25 deg/s. After calculating the sensitivity in the new peak frequency almost the same results were reached, so frequency peak shift is not the reason for low sensitivity. The reason is the 13.77 Hz frequency difference between sense and drive modes, shown in Figures 4.15 and 4.16. The driving frequency is 3140 Hz, so in the Q=200 case the bandwidth is about $\frac{3140}{200} = 15.7$ Hz, which is slightly more than 13.77 Hz; but in the case of Q=20000, the bandwidth is 0.157Hz which is about 100 times less than the frequency shift between sense and drive. In high Qs the frequency shift between sense and drive shows up more, while in the low Q mode it is not that

important. By remeshing the model in a way that the frequency of sense and drive exactly match or are less than the new bandwidth, the sensitivity should increase. This shows us going to high quality factors will not result in a good sensitivity without a good frequency matching of the sense and drive motions.

Polymer Coupler - 1 μm Nickel Cantilever - Q = 20000

With No Frequency Shift Between Sense and Drive

Figure 4.20 shows the new mesh pattern. The new frequency for both sense and drive is 3065.43 Hz. For this new analysis V_{dc}=5 V and V_{ac}=0.5 V are assumed, which leads to a driving force of 8.2 nN. Table 4.4 shows the simulation results for try number 4. The sensitivities can be computed as follows:

$$\text{Pattern rotation sensitivity} = \frac{9.84\ \text{deg}}{25\ \text{deg/s}} = 0.3936\,\frac{\text{deg}}{\text{deg/s}} \tag{4.36}$$

$$\text{Radial displacement sensitivity} = \frac{(0.5752\ )\mu\text{m}}{25\ \text{deg/s}} = 23.008\,\frac{\text{nm}}{\text{Deg/s}} \tag{4.37}$$

So, 100 deg/s will cause 39.36 deg pattern rotation and 100 deg/s will cause 2.3 μm change in amplitude for a vibration with less than 1 nm amplitude without any rotation in the sensing electrode. This means more than 400 deg/s cannot be sensed, because the electrode gap is 10 μm.

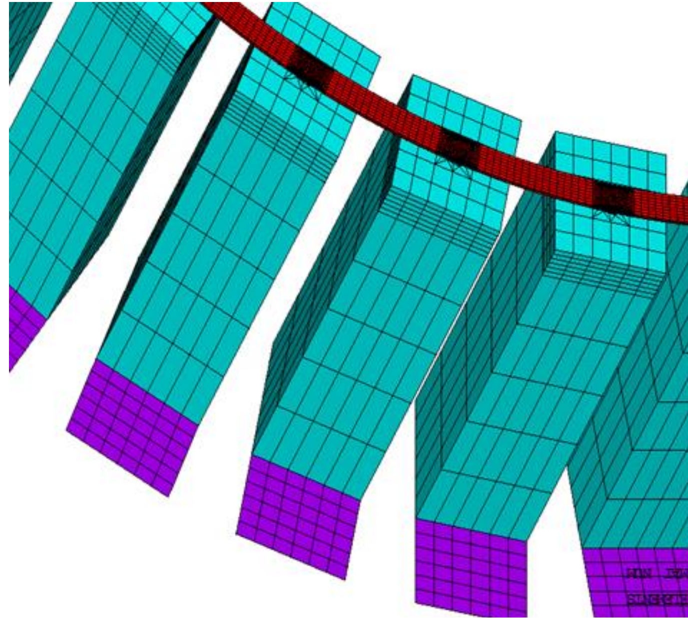

Fig 4.20: New mesh pattern with mapped meshing almost everywhere except places the coupler is attached to the resonator.

Table 4.4: Simulation results for different rotation speeds for try number 4.

Rotational velocity (deg/s)	Pattern rotation (deg)	45 degree node radial displacement (µm)	45 degree node tangential displacement (µm)	Maximum displacement (µm)
0	0	3065.432	0.000063473	1.1591
25	9.84	3063.26	0.57525	0.17

$$\Delta c = \frac{\varepsilon A}{2d^2}.Sensing\ resonator\ radial\ displacement$$

$$= \frac{8.85 \times 10^{-12} \times 530 \times 140 \times 0.5752 \times 10^{-6}}{2 \times 10^2}$$

$$= 1888.6\ af \tag{4.38}$$

$$\frac{\Delta c}{w} = \frac{1888.6\ af}{25\ deg/s} = 75.544\ \frac{af}{deg/s} \tag{4.39}$$

The minimum detectable signal = 0.013 deg/s (4.40)

Total sensitivity will also be 75.544 $\frac{\mathrm{mV}}{\mathrm{deg/s}}$, if 1 aF capacitance change corresponds to 1 mV output signal.

Readout Circuit

The most simple circuit to read the signal would be a capacitive Wheatstone bridge. Figure 4.21 produces a change in differential voltage as a function of change in capacitance. An AC voltage source must drive the bridge; its frequency needs to be stable and accurate. R1 can be a digital potentiometer (digi-pot) that is controlled to zero out the differential voltage or it can be a regular resistor. R3 provides a means to bias the instrumentation amplifier correctly and to keep the node between the capacitors from drifting over time, which needs to be much larger than C2's impedance. The divider equation can be corrected for this resistance, if necessary [26]. The advantages of this sensing configuration are an excellent common mode rejection ratio and detection of

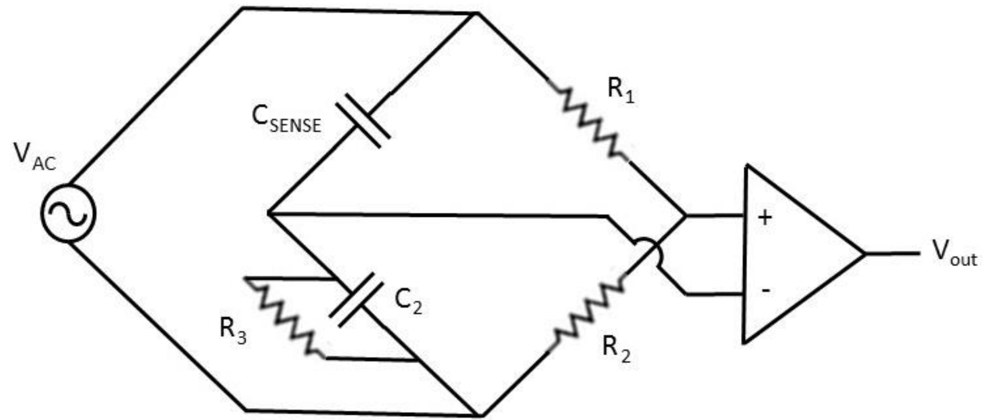

Fig 4.21: Capacitive readout circuit. Modified from [26].

open or shorted circuit. The disadvantages are power dissipation and the need for AC driving voltage. The frequency of input voltage to the readout circuit should be at least 10 times the sensor driving frequency in order to have a good understanding of the sensor mechanical vibrational behavior and also for preventing actuation of the system along the sense direction. If R_3 is neglected, from equation 4.9 for small vibration amplitude:

$$\Delta c = \frac{\varepsilon A}{d}\left(\frac{x}{2d}\right) = C_0\left(\frac{x}{2d}\right) \tag{4.41}$$

$$v_{out} = AV_{ac-readout}\left(\frac{C_0 + \Delta c}{2C_0 + \Delta c} - \frac{1}{2}\right)$$

$$= AV_{ac-readout}\left(\frac{x}{8d + 2x}\right) \sim A\left(\frac{V_{ac-readout}}{4}\right)\left(\frac{x}{2d}\right) \tag{4.42}$$

where A is the gain of the amplifier. The capacitance C_0 is 65.67 fF in our model. Now if equation 4.42 is divided by 4.41 then:

$$\frac{v_{out}}{\Delta c} = \frac{AV_{ac-readout}}{4C_0} \quad (4.43)$$

If the gain of the amplifier is considered to be 100 and $V_{ac-readout} = 10$ V for our model, the sensitivity would be 3.8 $\frac{mV}{aF}$. This shows that with an amplifier gain of 100, a sensitivity slightly more than what is assumed in our designs which was one $\frac{mV}{aF}$, is achievable. By using equation 4.39 the final sensitivity is found to be 287 $\frac{mV}{deg/sec}$, which is twice as high as our target 132 $\frac{mV}{deg/sec}$ sensitivity, reported in [5]. However, in commercial gyroscopes delta sigma circuits are mostly used for data acquisition. One main reason is their lower noise levels and the other reason is their higher sensitivities, even much better than one $\frac{mV}{deg/sec}$. For the purpose of this project a simple Wheatstone circuit will be used to show the device is working, but delta sigma circuits will be used in our device eventually. Now, if the two sides of equation 4.29 and 4.43 are multiplied, for a device with Wheatstone bridge measurement technique the total sensitivity will be:

$$\frac{v_{out}}{\Omega_z} \propto AV_{ac-readout}\frac{Q}{w_n} \quad (4.44)$$

This is the most complete sensitivity formula derived so far in this thesis for Wheatstone bridge readout gyroscope. It is very interesting to note that the total

sensitivity of the device is not a function of electrode gap or capacitance of the device; however, this may not be true in delta sigma circuits. In Wheatstone bridge readout circuits electrode gap affects the driving voltages of the gyroscope or the power consumption and has nothing to do with sensitivity of the device. For example, if it is fine to use high voltages, according to equation 4.30, V_{dc}=50 V and V_{ac}=5 V can be used to increase the gap distance from 10 µm to 46.4 µm while keeping the sensitivity at the same value of 287 $\frac{mV}{deg/sec}$. If it is necessary to round the electrode gap to 50 µm, V_{dc}=62.5 V and V_{ac}=5 V should be used. This will facilitate the fabrication process a lot and it can be a good practice to start the fabrication of the device with a large electrode gap and after mastering the fabrication steps, start reducing the electrode gap and deal with the fabrication problems of high aspect ratio trenches.

The next question that comes to mind is whether 287 $\frac{mV}{deg/Sec}$ is the maximum sensitivity possible for this device or not. In deriving this sensitivity it is assumed that quality factor is 20000, but large offset proofmasses have lower quality factors in practice. On the other hand, only a simple Wheatstone bridge is used which is less sensitive to delta sigma. So in practice it should first be seen how much the quality factor will be and then it can be estimated how much the sensitivity can be enhanced. In reference [5], the natural frequency of the device is 30KHz and the quality factor is 10000. So, from equation 4.29 it can be said that if the same readout circuit is used the sensitivity can be increased 10 times by reducing the natural frequency to 3KHz. The natural frequency can be further decreased to a sub-kilohertz regime by using a 3 mm diameter coupler instead of 2 mm and using larger proofmasses. The only concern here is the quality factor. Low quality factors may be achieved at first, but in consideration of

having access to the anchor parts, different techniques discussed in previous chapters can be used to increase it. Even in the presence of a slight decrease in quality factor, the frequency can be decreased so much that the sensitivity increases in total compared to previous works. Incorporating the bulk of the wafer in a ring gyroscope in such a way that reduces the natural frequency and finding solutions for misalignment cancelation between several fabrication steps was the main goal of this thesis. In future work on fabrication, practical quality factor enhancement methods and modematching will be discussed. The only problem in this design is that due to big proofmasses and compliant cantilevers, lots of parasitic acceleration noise is expected. In the next section a solution to this problem is offered.

Another problem that should be solved is the decrease of the peak of resonance for about 2.1 Hz for 25 deg/s rotation, which is 14 times the bandwidth. For high Q gyroscopes this is a very bad phenomenon because if the driving frequency is kept at the same frequency all the time the response will drop substantially in the presence of external rotation or temperature fluctuations. It is a common practice to incorporate a circuit to detect the peak of resonance at all times and change the driving frequency accordingly, which is called automatic gain control (AGC).

Acceleration Canceling Technique

The working frequency is 3126 Hz, which is shown in Figure 4.22. The z-parasitic mode shape frequency is 5641 Hz and is shown in Figure 4.23. The X and Y parasitic mode shape frequencies are 1440 Hz and are shown in Figures 4.24 and 4.25, respectively.

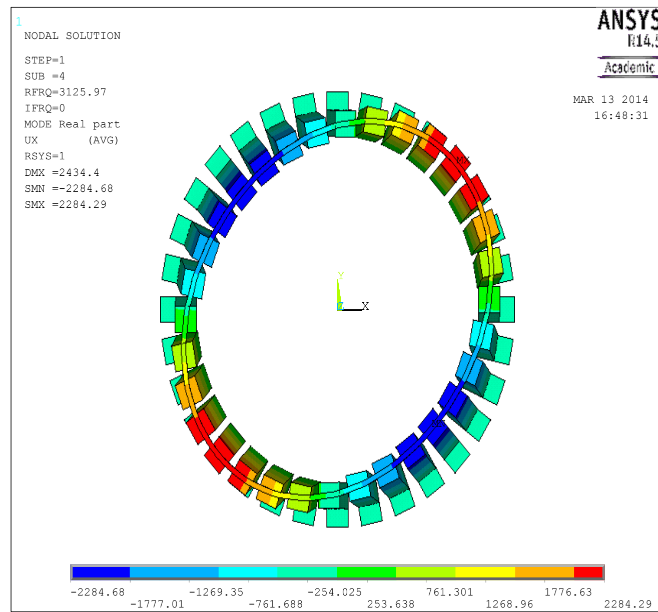

Fig 4.22: Working frequency of 3126 Hz.

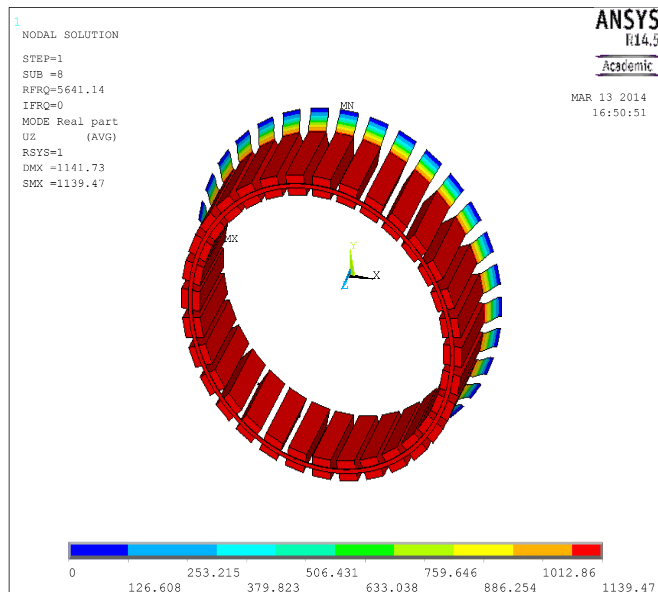

Fig 4.23: Z parasitic mode of 5641 Hz.

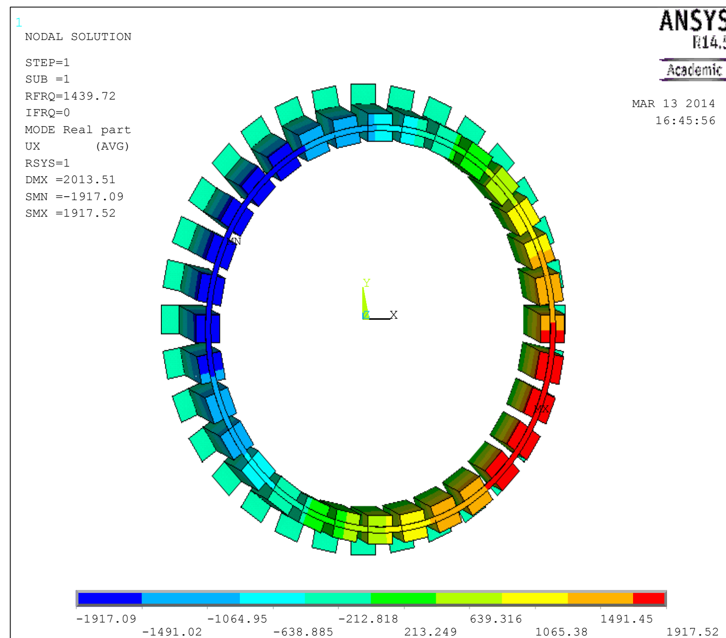

Fig 4.24: X parasitic mode of 1440 Hz.

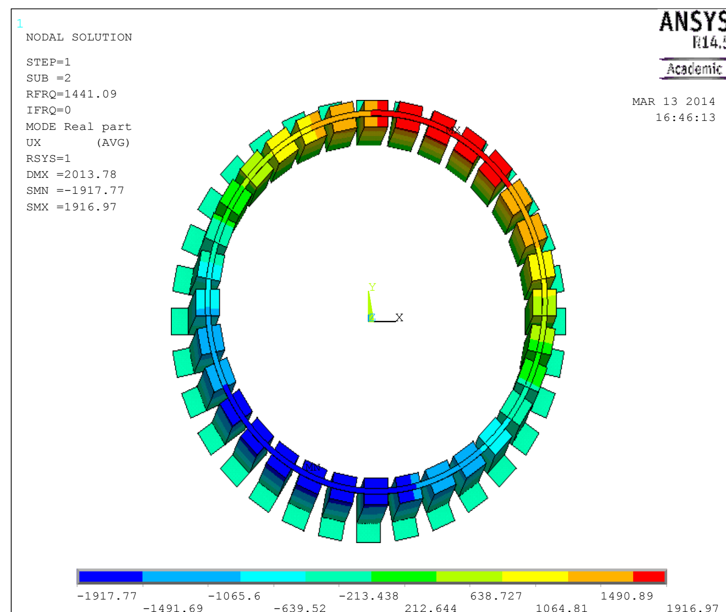

Fig 4.25: Y parasitic mode of 1440 Hz.

So there are three parasitic mode shapes. Two of them are about half the sensing frequency in the X and Y direction and one is almost 1.5 times the sensing frequency in the Z direction. If the gyroscope is working and the structure is subjected to a mechanical pulse in the Z direction, then the whole structure starts oscillating in the Z direction with a frequency about 1.5 times the sensing frequency until it is damped out based on the mode shape in Figure 4.23. If the structure undergoes a pulse in the X or Y direction, the structure starts to oscillate based on a combination of mode shapes (Figures 4.24 and 4.25) along the excitation direction with a frequency which is about half the sensing frequency until it is damped out. Since there are two parasitic modes, one below and one above the sensing frequency, if it is decided to use some kind of a filter to cancel acceleration a passband filter should be used. However, considering that the frequencies are very close it may not be a practical choice to use a filter. The simple and more effective solution is using multiple sensing capacitors along with signal subtraction and addition techniques.

By going to lower frequencies the sensitivity can be increased; however, as the spring constant decreases, the acceleration parasitic noise will also increase so a strategy is needed to get rid of them. With a very simple and effective way to cancel acceleration effects in three directions lower frequencies can be used to increase the sensitivity tremendously. More compliant cantilevers need less actuation voltages, which leads to less power consumption. Lower frequencies like 500 Hz can be achieved by reducing the thickness of the cantilevers or increasing the diameter of the coupler. This will reduce the anchor loss and increases the Q. Since the natural frequency of the system decreases six times, the sensitivity will rise six times. According to the noise formula for gyros

(equation 2.5) it can be noticed that the spring constant and quality factor are both in the denominator under the square root. Thus, it is not evident that going to lower frequencies will increase the noise because the quality factor may increase so much that it cancels the spring constant reduction effect. Another good thing about going to a sub-kilo hertz regime is reduction of the spring constant of the system so that the role of spring softening DC bias on the capacitors will be highlighted more. There are 32 resonators that DC bias: 12 of them will affect the drive direction more, 12 of them will affect the sense motion more, and 8 of them have equal effect on drive and sense frequency and cannot be used for tuning. After placing 40 volts on 4 resonators that affect the drive direction the most, the mode shape frequency of the drive was decreased about 13 Hz in simulations for our current dimensions with 10 μm gap. If the effective spring constant of the system decreases, the same voltage will change the frequency more. Thus, it can be claimed that this design almost cancels misalignment in the fabrication stage and because of the low spring constant of the system the remaining unwanted frequency mismatch between sense and drive can be tuned by DC biasing. If the drive mode has higher frequency than the sense frequency, 12 resonators along the drive direction can be used and if the sense frequency is higher the other 12 resonators should be used. The sensing and tuning capacitors are shown in Figure 4.26. The only drawback for lower frequencies is slightly slower time response. In order to cancel the acceleration effects, equation 4.45 should hold:

$$Output \propto (\Delta C_1 + \Delta C_2) - (\Delta C_3 + \Delta C_4) \tag{4.45}$$

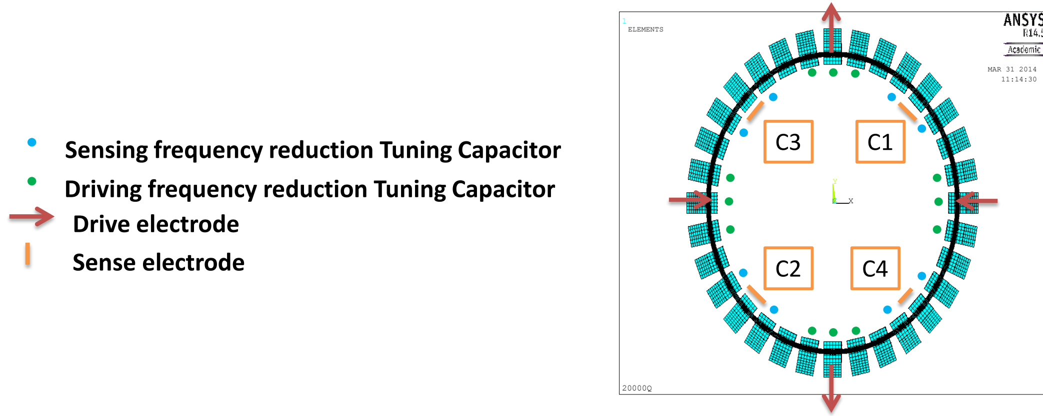

Fig 4.26: Multiple sensing electrodes.

An external impulse along the Z direction will change all four ΔC equally so the output does not change. In the case of an impulse in the X and Y direction, the response will be in-plane as a combination of mode shapes (Figures 4.24 and 4.25) along the impulse direction. In this condition the two values $\Delta C_1 + \Delta C_2$ and $\Delta C_3 + \Delta C_4$ will remain constant and the output is not affected. In this way, it can be concluded that if equation 4.45 holds, then acceleration effects will be suppressed. For Figure 4.27 the output voltage can be calculated as:

$$v_{out} = AV_{ac-readout}\left(\frac{2C_0 + \Delta C_1 + \Delta C_2}{4C_0 + \Delta C_1 + \Delta C_2 + \Delta C_3 + \Delta C_4} - \frac{1}{2}\right)$$

$$= AV_{ac-readout}\frac{(\Delta C_1 + \Delta C_2) - (\Delta C_3 + \Delta C_4)}{8C_0 + 2(\Delta C_1 + \Delta C_2 + \Delta C_3 + \Delta C_4)} \quad (4.46)$$

$$\Delta C = \Delta C_1 = \Delta C_2 = -\Delta C_3 = -\Delta C_4 \quad (4.47)$$

$$\frac{v_{out}}{\Delta c} = \frac{AV_{ac-readout}}{2C_0} \quad (4.48)$$

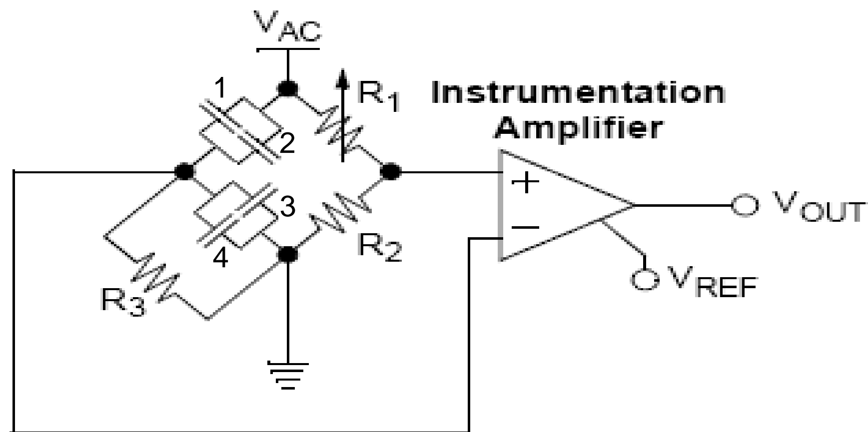

Fig 4.27: Multiple sensing electrode Wheatstone bridge configuration.

It can be noted that sensitivity of equation 4.48 is twice that of equation 4.42. In this way, by using the configuration in Figure 4.27, not only the acceleration effects can be canceled but also the sensitivity can be increased twice. The final sensitivity of the device using this configuration would be $574 \frac{mV}{deg/Sec}$. The problem with Figure 4.27 is that the left point between the four capacitors, which is connected to the instrumentation amplifier, is the central hub, which is grounded or has a DC bias in the drive circuit. This configuration should change in a way that the voltage of the central hub is fixed at all times. Figure 4.28 is a new configuration with four fixed capacitors numbered from 5 to 8. These fixed capacitors have the same dimensions with gyroscope resonating capacitors shown in Figure 2.8, with the difference that they do not have a trench on the glass which they are bonded to so that their capacitance values are fixed. These four capacitors should be fabricated next to each gyroscope to make sure their value differs as little as possible with respect to the gyroscope capacitors.

If the sensitivity formulation is written for this new configuration in Figure 4.28:

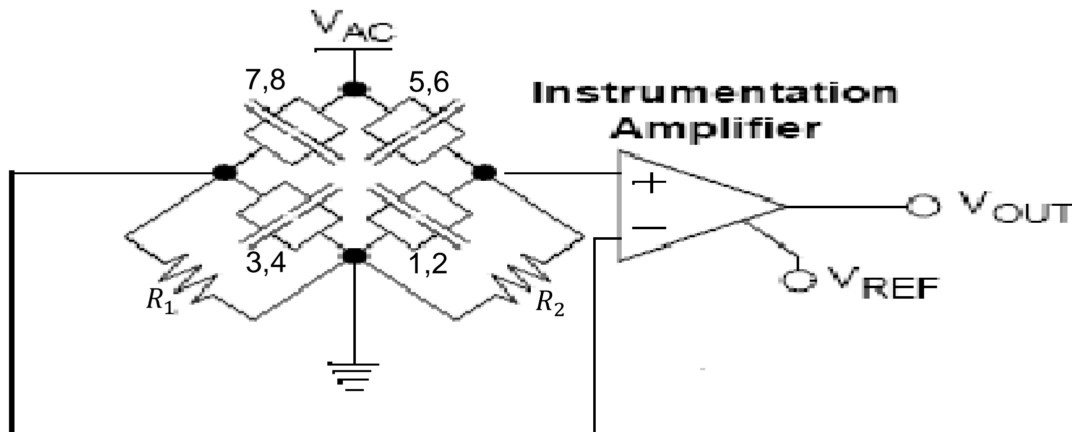

Fig 4.28: Multiple sensing electrode Wheatstone bridge configuration with fixed voltage central hub.

$$v_{out} = AV_{ac-readout} \frac{2C_0[(\Delta C_1 + \Delta C_2) - (\Delta C_3 + \Delta C_4)]}{(4C_0 + \Delta C_1 + \Delta C_2)(4C_0 + \Delta C_3 + \Delta C_4)} \tag{4.49}$$

After applying equation 4.47 to equation 4.49 the final sensitivity will be:

$$\frac{v_{out}}{\Delta c} = \frac{AV_{ac-readout}}{2C_0} \tag{4.50}$$

It can be noted that the sensitivity formula for Figure 4.28 is similar to the configuration shown in Figure 4.27. This is the final device that is going to be fabricated. It can be noted that in Table 4.4 the drive amplitude is only 1.15 µm, but since the voltages are modified after increasing the gap from 10 µm to 50 µm, the final vibrational amplitude would be 5.65 µm. This is about 10% of the electrode gap and can be considered in the linear range. It is strongly suggested to fabricate four fixed capacitors, near the gyroscope for the sensing circuit to have maximum sensitivity and minimum

offset bias in the Wheatstone bridge. Using fixed capacitors are considered the final design of this thesis. However, if off the shelf components should be used instead of fabricated fixed capacitors on the side of the gyroscope, capacitors 5 to 8 can be replaced with two trimmer capacitors, shown in Appendix B. The capacitance of each resonator with 50 μm gap is 13.13 fF, while the capacitance of trimmer capacitors varies between 0.5 to 1 pF. If it is assumed the sum of the capacitors 5 and 6 are 630 fF, their value can be considered as 48C, while C is 13.13 fF. The sum of the capacitors 7 and 8 is considered to be 48C+$\Delta c'$ because it may not be possible to tune both capacitors to be exactly the same. The output voltage in this case would be:

$$v_{out} = AV_{ac-readout}\left[\frac{48C}{50C_0 + \Delta C_3 + \Delta C_4} - \frac{48C + \Delta c'}{50C_0 + \Delta C_1 + \Delta C_2}\right] \tag{4.51}$$

After using equation 4.47 the output voltage will be like this:

$$v_{out} = AV_{ac-readout}\left[\frac{192C_0\Delta C + (50C_0 - 2\Delta C)\Delta c'}{2500{C_0}^2 + 4\Delta C^2}\right] \tag{4.52}$$

If $\Delta c'$ is considered to be zero the output voltage will be simplified to:

$$v_{out} = AV_{ac-readout}\left[\frac{\Delta C}{(13.021)C_0}\right] \tag{4.53}$$

If equation 4.53 is compared to equation 4.50, it can be noted that the sensitivity is 6.5 times less in this method since fF capacitors are not commercially available. If $\Delta c'$

is considered as C, then the zero rate output voltage will be:

$$v_{out} = AV_{ac-readout}\left[\frac{\Delta c'}{50C_0}\right] = \frac{AV_{ac-readout}}{50} \tag{4.54}$$

According to equation 4.53 this output voltage would be equivalent to the signal for $\Delta C = (0.26)C_0$ or x = (0.52)d. It can be concluded that capacitors should be tuned very carefully to minimize the zero rate output of the sensing circuit.

Stress Analysis

In order to find the maximum stress, the stress in the cantilevers when the tip of the resonator is touching the opposite electrode can be calculated.

$$\theta_{max} = \frac{d}{H} \tag{4.55}$$

Using equation 3.2, the maximum moment in the cantilever can be written as:

$$M_{max} = K_\theta \theta_{max} = \frac{EId}{LH} \tag{4.56}$$

By using equation 4.56, the maximum stress would be:

$$\sigma_{max} = \frac{M_{max}}{I}\left(\frac{h}{2}\right) = \frac{Edh}{2LH} = \frac{(219\ GPa) \times 50 \times 1}{2 \times 100 \times 530} = 103\ MPa \tag{4.57}$$

It should be noted that the vibration amplitude is about one-tenth of the electrode gap, and the stress concentration factor, which depends on the geometry of trench near the corners, can be considered as 10. In order to reduce the stress further according to equation 4.57, the thickness of the cantilevers can be reduced, which also increases the quality factor of the system, decreases the spring constant and increases the sensitivity.

The final dimensions of the device are shown in Table 4.5.

Table 4.5: Final dimensions and characteristic of the device.

Proofmass	530 µm high – 140 µm wide Silicon
Coupler	5 µm thick – 30 µm wide – 2 mm diameter SU8 polymer
Cantilevers	140 µm wide – 100 µm long – 1 µm thick Nickel
Number of proofmasses	32
Electrode gap	50 µm
Drive amplitude	5.65 µm
Driving DC voltage	62.5 V
Driving AC voltage	5 V
Sensing AC voltage	10 V
Sensing amplifier gain	100
Assumed quality factor	20000
Natural frequency	3126 Hz
Final sensitivity	574 $\frac{mV}{deg/sec}$
Minimum detectable signal	0.00174 deg/sec

CONCLUSION

The sensitivity of the gyroscope is inversely proportional to the natural frequency; however, if surface micromachining techniques are used it may not be possible to decrease the natural frequency of a ring gyroscope a lot. This thesis is focused on proposing a way to use bulk of the silicon wafer in the gyroscope to decrease the natural frequency to very low levels, such as a sub-kilohertz regime that cannot be achieved by single mask surface micromachining processes. It then proposes a solution for solving the misalignment problem caused by using multiple fabrication steps and masks instead of using only one mask in surface micromachined gyroscopes.

In this design discrete proofmasses are linked together around a circle by compliant structures to ensure the highest effective mass and lowest effective spring constant. By using a proposed double sided fabrication technology the effect of misalignments on frequency mismatch can be reduced. ANSYS simulations show that 20 μm misalignment between the masks causes a frequency shift equal to 0.3% of the natural frequency, that can be compensated for by using electrostatic frequency tuning. Acceleration parasitic effects can also be a major problem in a low natural frequency gyroscope. In this design a multiple sensing electrode configuration is used that cancels the acceleration effects completely. The sensitivity of the gyroscope with 3126 Hz natural frequency is simulated to be 574 $\frac{mV}{deg/sec}$, or about four times higher than 132 $\frac{mV}{deg/sec}$, which was used as a benchmark for a sensitive gyroscope.

APPENDIX A

MISALIGNMENT COMPENSATION TECHNIQUE

In conventional MEMS gyroscopes, usually attempts to use only one mask are tried because if several masks are used, because of the unavoidable misalignment of the masks, the final structure becomes useless, e.g., gap distances may differ in different parts of the system. Sometimes, in order to use several masks, the gap distances are defined by a sacrificial layer conformal chemical vapor deposition (CVD) method on the side walls and etching. The main goal of this research is using the bulk part of silicon wafer in the gyroscope structure to increase the sensitivity of the device. When the bulk part of the silicon is used at least two masks are needed based on the design of the gyroscope. In this design, since there is a ring on top of the structure three main masks are needed to define the structure. The question is how the misalignment effect can be canceled out. A simplified version of this gyroscope without the coupler on top of it was fabricated in order to see the fabrication feasibility of this design. A common method to fabricate the device was used, in which the cantilever side of the structure was patterned from the bottom by doing DRIE for about 50 μm and from the other side of the wafer the structure was formed using another DRIE process to reach the cantilever side. As can be seen in Figure A.1, there are lots of issues with the conventional fabrication method due to the misalignment of the masks. There would be a discontinuity in the proofmass

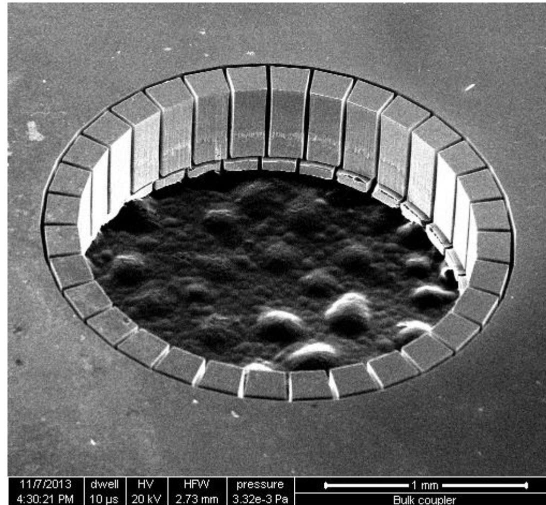

Fig A.1: Fabricated prototype of the structure using the conventional fabrication method. There is a 55 micron misalignment between the masks on the two sides of the wafer.

sidewalls and the center of gravity of the proof mass changes with respect to the cantilever around the circle. The cantilever's dimensions change because sometimes some part of it is covered by proofmass or a substrate part and at some places cantilevers are completely covered. At some places two resonators are connected together. If a ring coupler is added to this system, it would be impossible to match sense and drive frequency, even by removing materials. Misalignment between the front-side and the back-side mask is about 55 microns, which can be reduced below 10 μm by several tries, but let us assume the misalignment is going to remain this bad. Even if better tools are used 3 or 4 μm of misalignment is always there and cannot be avoided; that 3 or 4 μm will make the sense and drive frequencies not match. From this observation it is concluded that the conventional fabrication method is not useful in designing a system with more than one mask. In a conventional method DRIE is performed from both sides, but the summation of etching time from the two sides equals the time needed to etch

entirely through the silicon wafer. In other words, the DRIE is stopped when the etch front from the second side reaches the etch front from the first side.

To solve the misalignment problem a simple method is proposed. If four lines are intersected to form a parallelogram in the center and two of the parallel lines are shifted together with respect to the other two lines in a random direction, then the dimensions of the internal parallelogram and its area does not change. This is valid only on parallelograms and not on trapezoids or a shape formed by intersection of four curved lines (Figure A.2).

In order to show the practical usage of this concept, consider a rectangular feature is on the top mask over another rotated rectangular feature on the bottom mask. DRIE can be done from the top side to form a wall shaped structure as shown in Figure A.3. Now, if another DRIE process is done from the bottom, the final structure would be a column between the two masks and its dimensions are not related to the direction and amount of misalignment between the top and bottom masks. Now, it is only necessary to make room for the column in order to be able to move the parallel lines of the top and bottom features, at least for 55 µm, which is our expected misalignment.

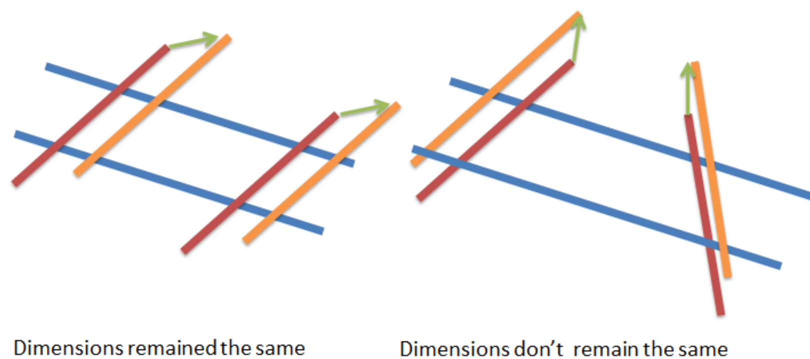

Fig A.2: Insensitivity of the dimensions of parallelogram to shifting of two facing edges.

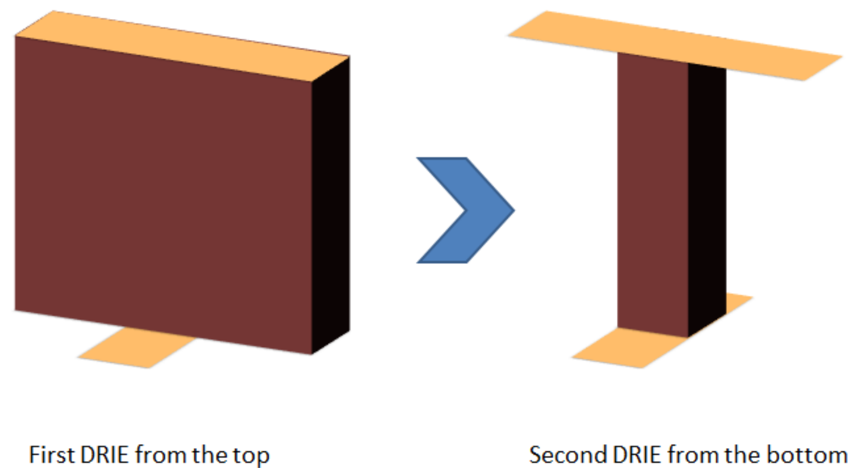

Fig A.3: Uniformity and insensitivity of the dimensions of the column to misalignment of the top and bottom masks.

This fabrication method has none of the problems of the conventional fabrication method, like the step in the middle of the structure or changes of the dimensions of the final structure; however, the total etching time is twice the conventional etching option. A resonator with a sensing or driving capacitor would have more moving edges in the two masks. In Figure A.4, the blue lines are for the bottom mask and the red lines are for the top mask. Lots of these proofmasses are arranged around a circle to form the final gyroscope structure. One of the features that should be considered in this design and in this type of fabrication is a room for floating of the structure both in X and Y directions, because misalignment can be towards any direction. So, some overhangs should be considered in the gap area of the bottom mask to compensate for probable misalignment. If the two masks have misalignment along the resonator axis, in the final structure the overhangs separation in the middle of the gap will move slightly in one direction. Still, since the thickness of the metallic layer is much less than the thickness of the proofmass

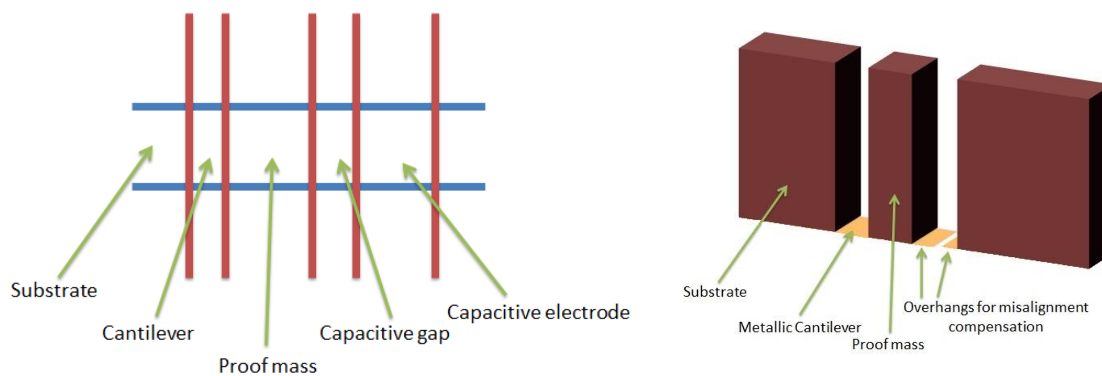

Fig A.4: Floating lines on the top and bottom masks and different features that are finally generated.

the percentage change of mass of the resonator would be almost negligible. It is also known that overhangs move rigidly with the proofmass and will not affect the spring constant. Overall, it can be concluded that the natural frequency of each resonator is not affected by the misalignment in this fabrication method.

To fabricate the whole gyroscope structure, at first polygonal trenches are etched from the top side and then the fabricated polygonal wall is etched into columns or proofmasses with another mask from the bottom. In this fabrication method, the width of the cantilever should be the same as the width of the proofmass, but its thickness and length can be changed to tune cantilever stiffness. If fixed electrodes slightly wider than the resonator are needed, then the width of the two overhangs should not be equal anymore. In Figure A.5, a sample top and bottom mask to fabricate a set of resonators without the capacitive sensing electrode are shown to demonstrate the concept of resonator fabrication. The final device will additionally have capacitive sensing electrodes. These are not shown in Figure A.5 for a better understanding of the misalignment cancelation technique. The effect of misalignment of the mask on the

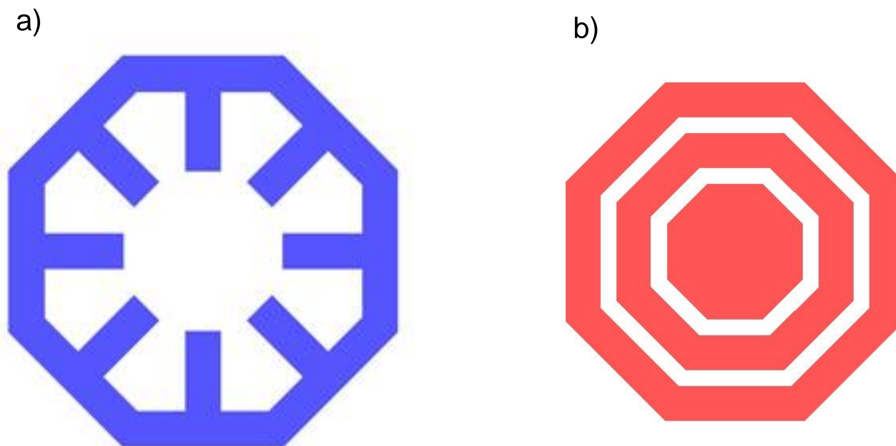

Fig A.5: Two needed masks to fabricate eight resonators.
a) Bottom mask, b) top mask.

movement of proofmasses with respect to the initial position is also depicted in Figure A.6. It can be seen that because of the misalignment, dimensions of the cantilevers and the proofmasses and position of each cantilever-proofmass pair with respect to each other will not change and there would be no step in the proofmasses in SEM images. In other words, the misalignment completely cancels out for each cantilever-proofmass set, but the relative position of each set to the others will slightly change. When the position of proofmasses in the case without misalignment and the case with it are compared, it can be noticed that, some of the proofmasses move and some of them stay still. When the mass does not move due to the misalignment, the size of overhangs for misalignment compensation change and when the overhangs for misalignment compensation does not change size, the proofmass has its maximum displacement. In Figure A.6, the distance between the upper half adjacent resonators increases while the distance between the lower half adjacent resonators decreases. If a type of coupler that connects the edges together is used, then the coupling between resonators will

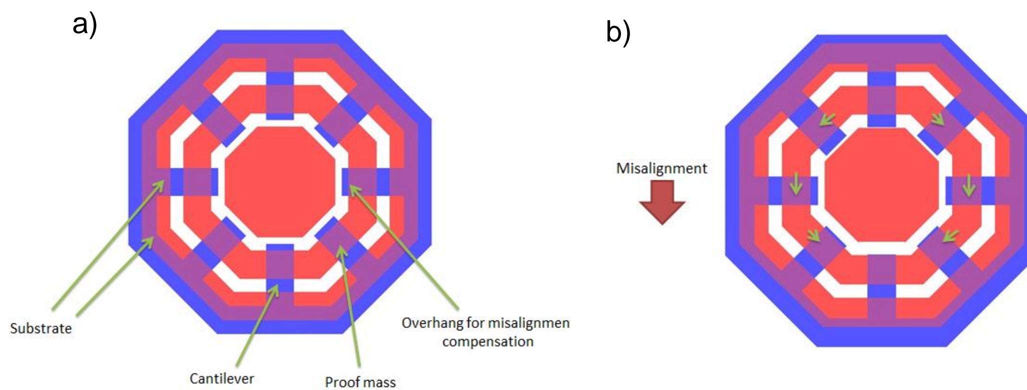

Fig A.6: The effect of misalignment of the bottom mask on the movement of proofmasses with respect to the initial position. a) Center position, b) Slight misalignment of the bottom mask towards downward direction.

change a lot and cause a large frequency change between sense and drive mode; however, if a coupler that joins a point on top of the proofmass to a point on top of the adjacent proofmass is used, since cantilevers and proofmasses are wide, the drive and sense frequency will not differ that much. To make sure, FEM simulation software can be used to see how much the misalignment affects the frequency mismatch, as is done in the last section of Chapter 3. Fixed electrodes can be added to this design if the wafer is bonded to a glass substrate. Using this fabrication technique, it can be guaranteed that the capacitor area and gap is not affected by misalignment. The capacitor gap should be more than twice the expected misalignment, since two overhangs are needed with at least the length of the misalignment which should not be connected to each other.

In order to have high sensitivity the frequency of operation should be kept around 1 KHz, which requires a cantilever thickness of around 1 μm. A high quality factor which is proportional to $\left(\frac{l}{t}\right)^3$ is also preferable for the case of a cantilever beam resonator

without proofmass. Piezoelectric MEMS energy harvesters have the same frequency range of below 1 KHz and should be studied to understand the behavior of low frequency oscillators similar to the ones that are used in this design. The difference is that in energy harvesters low quality factors are needed so that the harvester can absorb energy from a wide range of frequencies. To decrease the natural frequency in energy harvesters a large proof mass and long cantilevers for holding them are used, usually. As an example, in one of the previous works [27], the thickness of the cantilever is 36 µm, its length is 3200 µm but the resulting quality factor is only 233, which means in a resonator with a big proofmass lots of energy is going to escape away from the supports if nothing is done about it. The best way to have a very thin cantilever is by using SOI wafer or a metallic cantilever. However, because of fabrication issues it is very hard to make a thin cantilever by timing the DRIE etch out of silicon from the other side of the wafer. In addition, SOI wafers and metallic cantilevers decrease the anchor loss because of material mismatch. A 1 µm thickness metallic cantilever with 100 µm length should be a good start to see what the quality factor will be. If it is decided to use a metallic cantilever, the fabrication parameters should be optimized for stress free conditions. Electroplating of a metallic layer can be a good choice because it is a low temperature and low residual stress process.

APPENDIX B

TRIMMER CAPACITOR DATASHEET

Table B.1: Trimmer capacitor TZY2Z010A001R00.

Manufacturer	Murata Electronics North America
Manufacturer part number	TZY2Z010A001R00
Description	CAP TRIMMER 0.5-1PF 25V SMD
Lead Free ftatus / RoHS status	Lead free / RoHS compliant
Category	Capacitors
Family	Trimmers, Variable capacitors
Series	TZY2
Packaging	Tape & Reel (TR)
Capacitance range	0.5 ~ 1pF

Table B.1 continued

Adjustment type	Top adjustment
Voltage	25V
Size	Rectangular - (3.20mm x 2.50mm)
Height - Seated (Max)	0.049" (1.25mm)
Mounting Type	Surface Mount
Features	General Purpose
Dynamic catalog	TZY2 Series
Other names	490-2009-2

Fig B.1: Trimmer capacitor TZY2Z010A001R00.

REFERENCES

[1] Cenk Acar and Andrei Shkel, *MEMS vibratory gyroscopes structural approaches to improve robustness*, Springer, 2009.

[2] Navid Yazdi et al, "Micromachined inertial sensors," in *Proceedings of the IEEE*, 1998, pp. 1640-1659.

[3] Kai Liu et al., "The development of micro-gyroscope technology," *Journal of Micromechanics and Microengineering,* 19, 2009.

[4] P. B. Ruffin, "Progress in the development of gyroscopes for use in tactical weapon systems," in *Proceedings of SPIE, Smart Structures and Materials*, 3990, 2000, pp. 2-12.

[5] Guohong He and Khalil Najafi, "A single-crystal silicon vibrating ring gyroscope," in *Fifteenth IEEE International Conference on Micro Electro Mechanical Systems,* Las Vegas, NV, USA, 2002.

[6] Minoru Kurosawaa et al., "A surface-acoustic-wave gyro sensor," in *Sensors and Actuators A (Physical),* 66 (1-3), 1998, pp. 33-39.

[7] V. K. Varadan et al., "Design and development of a MEMS-IDT gyroscope," in *Smart Materials and Structures*, 9(6), 2000, pp. 898-905.

[8] Takao Murakoshi et al., "Electrostatically levitated ring-shaped rotational-gyro/accelerometer," in *Japanese Journal of Applied Physics*, 42, 2003, pp. 2468–2472.

[9] Watanabe Y. et al., "SOI micromachined 5-axis motion sensor using resonant electrostatic drive and non-resonant capacitive detection mode," in *Sensors and Actuators A (Physical)*, 130-131, 2006, pp. 116-123.

[10] Alper S. E. et al., "A low-cost rate-grade nickel micro-gyroscope," in *Sensors and Actuators A (Physical)*, 132(1), 2006, pp. 171–181.

[11] Lutz M.et al., "A precision yaw rate sensor in silicon micromachining," in *Solid State Sensors and Actuators Transducer'97*, 1996.

[12] Thakur Praveen Singh et al., "Frequency response of in-plane coupled resonators for investigating the acceleration sensitivity of MEMS tuning fork gyroscopes," in *Microsystem Technology*, 2012, pp. 797–803.

[13] Houri Johari and Farrokh Ayazi, "Capacitive bulk acoustic wave silicon disk gyroscopes," in *International Electron Devices Meeting*, San Francisco, CA, 2006.

[14] J. Cho et al., "Single-crystal-silicon vibratory cylinderical rate integrating gyroscope (CING)," in *16th International Conference Transducers Solid-State Sensors, Actuators and Microsystems*, Beijing, 2011.

[15] W.T. Thomson, *Theory of vibration with applications*, Prentice Hall, Englewood cliffs, NJ, 1993.

[16] Zhili Hao et al., “An analytical model for support loss in micromachined beam resonators with in-plane flexural vibrations,” in *Sensors and Actuators A*, 109, 2003, pp. 156–164.

[17] Hiroshi Hosaka et al., “Damping characteristics of beam shaped micro-oscillators,” in *Sensors and Actuators,* A 49, 1995, pp. 87-95.

[18] J.C. Hsu et al., “Reducing anchor loss in MEMS resonators using mesa isolation,” in *Journal of Microelectromechanical Systems*, 18(44), 2009.

[19] Jing Wang et al., “1.51-GHz nanocrystalline diamond micromechanical disk resonator with material-mismathched isolating support,” in *17th IEEE International Conference on MEMS*, 2004.

[20] J.C. Hsu et al., “Reducing anchor loss in micromechanical resonators using phononic crystal strips,” in *IEEE International Ultrasonics Symposium Proceedings*, 2011.

[21] Jae-Kap Kim, “Semiconductor device having a SOI structure with substrate bias formed through the insulator and in contact with one of the active diffusion layers,” Hyundai Electronics Ind. Co., Kyoungki-do, Rep. of Korea, 1999.

[22] Matthew J. Rutten and Steven H. Voldman, “Electrical contact to buried SOI structure,” U. S. Patent 5 889 293 A, Apr 4, 1997.

[23] Cenk Acar and Andrei M. Shkel, “An approach for increasing drive-mode bandwidth of MEMS vibratory gyroscopes,” in *Journal of Micro Electromechanical Systems*, 14(3) , 2005.

[24] Jongpal Kim et al., “Why is (111) silicon a better mechanical material for MEMS?” in *IEEE Procedings Transducers*, 2001.

[25] M.A. Lemkin et al., ”A 3-axis surface micromachined Sigma Delta accelerometer,” in *IEEE International Solid-State Circuits Conference*, 1997.

[26] Shayeste Kiaei, 2008, *Wheatstone bridge sensing methods*, available at: http://saba.kntu.ac.ir/eecd/ecourses/inst%2086/Projects/Instrumentational%20/Shayeste%20Kiaei/conditioning%20circuit-sent/capacitive_wheatstone_bridge.htm.

[27] Shen, “The design, fabrication and evaluation of a MEMS PZT cantilever with an integrated Si proofmass for vibration energy harvesting,” in *Journal of Micromechanics and Microengineering*, 2008.